ADVANCED CONTROL FOR POWER DENSITY MAXIMIZATION OF THE BRUSHLESS DC GENERATOR

A Dissertation

by

HYUNG-WOO LEE

Submitted to the Office of Graduate Studies of
Texas A&M University
in partial fulfillment of the requirements for the degree of

DOCTOR OF PHILOSOPHY

December 2003

Major Subject: Electrical Engineering

ADVANCED CONTROL FOR POWER DENSITY MAXIMIZATION OF THE BRUSHLESS DC GENERATOR

A Dissertation

by

HYUNG-WOO LEE

Submitted to Texas A&M University
in partial fulfillment of the requirements
for the degree of

DOCTOR OF PHILOSOPHY

Approved as to style and content by:

Mehrdad Ehsani (Chair of Committee)	
Andrew K. Chan (Member)	Karen L. Butler-Purry (Member)
Reza Langari (Member)	Chanan Singh (Head of Department)

December 2003

Major Subject: Electrical Engineering

ABSTRACT

Advanced Control for Power Density Maximization of the Brushless DC Generator.

(December 2003)

Hyung-Woo Lee, B.S.; M.S., Hanyang University, Seoul, Korea

Chair of Advisory Committee: Dr. M. Ehsani

This dissertation proposes a novel control technique for power density maximization of the brushless DC (BLDC) generator which is a nonsinusoidal power supply system. In a generator of given rating, the weight and size of the system affect the fuel consumption directly, therefore power density is one of the most important issues in a stand-alone generator. Conventional rectification methods cannot achieve the maximum power possible because of a distorted or unsuitable current waveform. The optimal current waveform for maximizing power density and minimizing machine size and weight in a nonsinusoidal power supply system has been proposed theoretically and verified by simulation and experimental work. Also, various attributes of practical interest are analyzed and simulated to investigate the impact on real systems.

To my parents, my wife Kirang

and

my beloved son, Alex Donghan

ACKNOWLEDGEMENTS

I would like to express my special appreciation to Dr. M. Ehsani for his inspiring guidance and constant encouragement throughout the progress of this work. I also deeply appreciate the members of my committee, Dr. A. K. Chan, Dr. K. L. Butler-Purry, and Dr. G. Langari, for their valuable comments and interest in this project. My thanks are extended to the past and present lab members at Texas A&M University and Hanyang University, Korea. I also need to express my sincere gratitude to Dr. J. Lee and Dr. J. P. Hong for their continuous support.

Without my family's sacrifice and support, this study would not have been possible. I would like to affirm my indebtedness to my parents, sisters, brothers, parents-in-law, and wife for their unconditional love and encouragement.

TABLE OF CONTENTS

TABLE OF CONTENTS (Continued)

LIST OF TABLES

LIST OF FIGURES

LIST OF FIGURES (Continued)

LIST OF FIGURES (Continued)

LIST OF FIGURES (Continued)

LIST OF FIGURES (Continued)

LIST OF FIGURES (Continued)

FIGURE Page

CHAPTER I

INTRODUCTION

Recently, the demands for electricity have increased very rapidly. Even though state and federal governments build new power plants, the supply is still insufficient and such plants take a long time to design and build. Thus, nowadays, stand-alone generators are essential, not only in remote areas but also in urban areas, and especially for the transportation system. The major issue regarding the stand-alone generator is, undoubtedly, power density maximization for a given power rating. In other words, minimal sizing and lighter weight in the same rated machine are the most important factors.

Among several kinds of generators, the brushless DC (BLDC) generator is the best candidate for improving power density. As compared with other generators, the BLDC generator has lots of benefits; it is lightweight, it has a compact design, and low maintenance because it has a magnetic source inside itself. With the inherent advantages of the BLDC generator, additional increases in power density can be expected by the advanced control techniques, resulting in considerable reduction of weight and volume. This technique is highly desirable for many applications, such as small power plants, remote area off-grid power supply systems, and especially transportation system such as

---

This dissertation follows the style and format of *IEEE Transactions on Industry Applications*.

conventional cars, EVs (Electric Vehicle), or HEVs (Hybrid Electric Vehicle) that need to be downsized and lightweight.

In the conventional drive system, generated electrical power is transferred to the DC-side battery through the uncontrolled diode rectifier and loses a great deal of energy as a reactive power. Therefore, many researches have been done to reduce this reactive power in the power generation system. However, no research for a non-sinusoidal power supply system such as a BLDC generator has been done.

This dissertation presents a novel control technique to maximize the power density and minimize the size and weight of the BLDC generator that has the trapezoidal induced EMF for a given machine by controlling the current spectrum using active switches. This control technique can be adopted into both linear and rotary type BLDC generators, into both single and three-phase.

The proposed method does not rely on the measured back-EMF; hence the need for external hardware circuitry for sensing terminal voltages has been removed. Moreover, the proposed algorithm is very suitable for implementation in low-cost, fixed-point Digital Signal Processors (DSPs).

A simulation model for the BLDC generator drive has been developed to validate the proposed methods, and experimental results prove the proposed methods. Also, various attributes of practical interest are analyzed and simulated to investigate the impact on real systems.

A. Research Objectives

The main objective of this research is to develop a control method for maximizing power density and efficiency of the BLDC generator in the given rating of a machine so that accomplish minimal sizing and lighter weight. That is, for a generator of given design, we can maximize the power throughput by control means as shown in Fig. 1. In order to achieve this, the unique optimal current waveform is developed and evaluated.

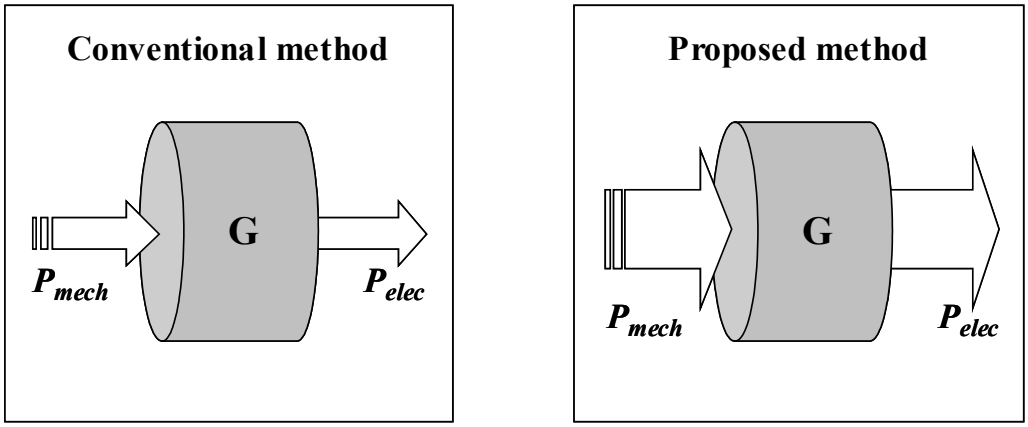

Fig. 1. Maximum power throughput for a generator of given design.

The first objective of this research is to develop new theories for power density maximization in the single-phase and three-phase nonsinusoidal power supply system.

The second objective of this research is to develop simulation models to verify the validity and evaluate the performance of the proposed control method. The proposed

method should be suitable for implementation in low-cost fixed-point digital signal processors.

The third objective of this research is to implement the proposed control method on the experimental test-bed that has been built in the lab to verify the theories and simulation results.

The final objective is to do further detailed studies on the various attributes of the proposed control techniques, such as neutral point connection, sinusoidal current waveform, load variation, multi-phase system and unbalanced-EMF system in order to investigate the impact on real systems.

B. Dissertation Outline

This dissertation starts with an introduction in Chapter I to the BLDC generator and the need for power density maximization. The research objective to develop a new control method is explained.

The fundamental characteristics of a BLDC generator are presented in Chapter II. Mechanical structure and the electromagnetic behavior of the BLDC generator, trapezoidal induced EMF, and the advantages and disadvantages of BLDC generators are presented.

The conventional rectification methods of the BLDC generator are reviewed in Chapter III. The drawbacks of the existing method are investigated so as to develop a new method that can solve those problems.

The theory of the advanced control method for power density maximization of the single-phase and three-phase BLDC generator is presented in Chapter IV. Derivation of an optimal current waveform by using line-to-line voltage equation is included. Also, the details of simulation work performed to validate the theory are presented.

The experimental results obtained on the test-bed developed in the laboratory are presented to verify the theory and simulation results, in Chapter V.

The analyses of various attributes of the proposed control method have been performed and the results are presented in Chapter VI. The influences from several situations (neutral connection, sinusoidal current waveform, load variation, one-phase failure, unbalanced induced EMF, and multi-phase) on the performance of the proposed control technique are investigated through simulation and experiments, and the results are detailed. And also, effects of the various error sources are investigated as well.

Chapter VII concludes this dissertation and describes contribution of this research, as well as the future research work.

CHAPTER II

CHARACTERISTICS OF THE BLDC GENERATOR DRIVE

Advances in the development of the permanent magnet (PM) have made the PM machine popular in many applications. It is compact, lightweight and low maintenance. In addition, development of fast semiconductor switches and cost-effective DSP processors have revolutionized the motor/generator drives. These new opportunities have contributed to the field of motor/generator drives by introducing novel configurations for electric machines and improving performance in which the burden is shifted from complicated hardware structures onto software and control algorithms. This, in turn, has resulted in considerable improvement in cost while upgrading the performance of the overall drive system.

The BLDC motor/generator drive system is the most illustrative example of this trend. With the inherent mechanical advantages of the BLDC generator, additional increase in power density can be expected with the advanced control technique, and this technique results in considerable reduction of weight and volume.

In this chapter, characteristics of the BLDC generator are described. The detailed structure of the BLDC generator; permanent magnets used in a BLDC generator; induced EMF; advantages and disadvantages of the generator; and simplified model of the BLDC generator drive are included.

A. Mechanical Structure of the BLDC Generator [1]-[7]

The brushless DC (BLDC) generator is a kind of permanent magnet generator that has permanent magnets inside of the machine. Because of the permanent magnet, as shown in Fig. 2, the brush and the commutator used for supplying the magnetic flux are not necessary compared with the DC machine; therefore, the maintenance for those components is not required. As the field winding is substituted with a permanent magnet, Joule heat from copper loss of the field winding is absent. The stator has laminated steel to reduce the eddy current loss and the structure is the same as the BLDC motor.

The permanent magnet BLDC generator can be categorized according to the way the permanent magnets are mounted on the rotor and the shape of the induced EMF (Electromotive Force). The permanent magnets can either be surface mounted or interior mounted in the rotor, and the induced EMF shape in the stator can either be sinusoidal or trapezoidal.

1) Surface-Mounted Permanent Magnet Type (SMPM)

Fig. 2(a) shows the rotor of a surface-mounted permanent magnet type. Each permanent magnet (PM) is mounted on the round surface of the rotor. It is easy to build but there is a possibility for the attached PM to fly apart during high-speed operation. Typically, for this type of generator, the inductance variation by rotor position is negligibly small.

2) Interior-Mounted Permanent Magnet Type (IPM)

Fig. 2(b) shows the rotor of the interior-mounted PM type. Each permanent magnet is mounted inside of the rotor. The use of the interior-mounted PM is not as common as of the surface-mounted type, but the interior-mounted PM is a good candidate for high-speed operation. It is noted that there is an inductance variation for this type of machine because the effective air-gap varies by rotor position.

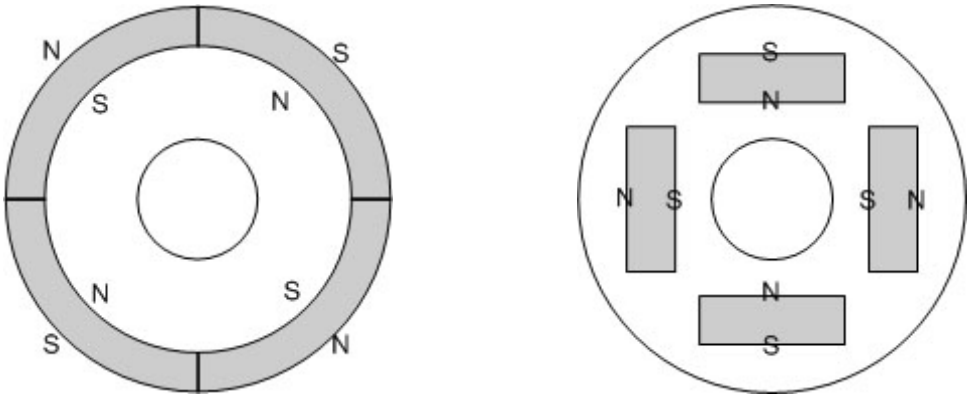

(a) Surface-mounted PM rotor (b) Interior-mounted PM rotor

Fig. 2. Cross sectional view of the permanent magnet rotors.

3) Trapezoidal Shape Induced EMF Type

Fig. 3(a) shows the winding structure of the trapezoidal induced EMF type. The trapezoidal induced EMF is a salient feature of the BLDC generator. From the design point of view, we can have approximately 15% higher power density compared with a permanent magnet synchronous generator [8]. The detailed explanation about waveform

of the induced EMF of the BLDC generator will be presented section C. It has the following characteristics:

- Rectangular distribution of magnetic flux in the air gap
- Concentric stator windings

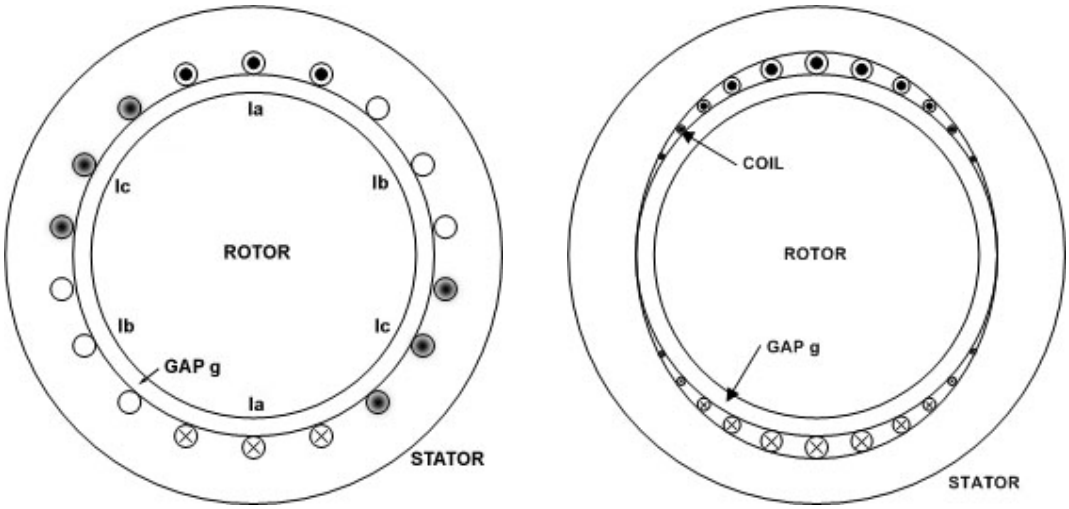

(a) Trapezoidal induced EMF type (b) Sinusoidal induced EMF type

Fig. 3. Winding structure of the BLDC generator.

4) Sinusoidal Shape Induced EMF Type

Fig. 3(b) shows the winding structure of the sinusoidal induced EMF type. It has the following characteristics:

- Sinusoidal distribution of magnetic flux in the airgap
- Sinusoidal distribution of stator conductors

The most fundamental aspect of the sinusoidal induced EMF type of generator is that the EMF generated in each phase winding by the rotation of the magnet should be a

sinusoidal wave function of the rotor angle. The basic operation of a sinusoidal EMF type of BLDC generator is very similar to the AC synchronous generator. Typically, the sinusoidal induced EMF type of generator is not considered as a BLDC, but rather a PMSM (permanent magnet synchronous machine). In this dissertation, the advanced control for power density maximization of a BLDC generator that has trapezoidal induced EMF and SMPM type is presented.

B. Permanent Magnets of the BLDC Generator [9]

Permanent magnets are essential ingredients to the BLDC generator. In last two decades permanent magnet technology has been improved substantially. The nature of the permanent magnet can be explained through a B-H curve as in Fig. 4. When a permanent magnet has been magnetized by external magnetic filed, it will remain magnetized even if the magnetic field intensity is gone. The magnetic flux density at this point is called the remanence, denoted B_r. The remanence is the maximum flux density that the magnet can produce by itself. And if magnetic field intensity is increased in the opposite polarity, the flux density will eventually become zero. The magnetic field intensity at this point is called the coercivity, denoted H_c. The absolute value of the product of the magnetic flux density, B and the magnetic field intensity, H at each point along the curve in the second quadrant region is called the energy product.

The operating point is also located at the point of intersection between the permeance line and the hysteresis curve in the second quadrant region. The permeance

line is determined by the characteristics of the machine structure: airgap length, magnetic path length, number of turns of the coil.

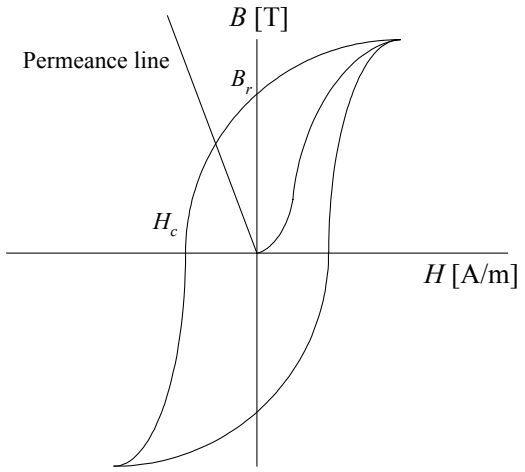

Fig. 4. Hysteresis loop of a permanent magnet.

Nowadays, many different types of permanent magnet materials are available. The types available include Alnico, Ferrite (ceramic), Rare-earth samarium-cobalt, and Neodymium-iron-boron (Nd-Fe-B). The Nd-Fe-B magnets, which have been developed recently, have the highest power product. Ferrite magnets are the most commonly used due to their cost effectiveness. Each magnet type has different properties leading to different constraints and different levels of performance. The characteristics of the permanent magnet materials are compared in Table I and Fig. 5. Ferrite magnets are widely used because the material and production costs are both low, even though they have low remanence, coercivity, and power product. Nd-Fe-B magnets have the highest remanence and coercivity but the initial price is very high.

Table I. Characteristics of the permanent magnets.

Permanent Magnet	Remanence B_r	Coercivity H_c	Cost	Features
Alnico	High	Low	Inexpensive	Excellent mechanical strength
Ferrite	Low	Medium	Relatively inexpensive	Fragile
Neodymium-Iron-Boron	High	High	Relatively expensive	Excellent performance
Rare-Earth Samarium-Cobalt	High	High	Very expensive	Small temperature coefficient

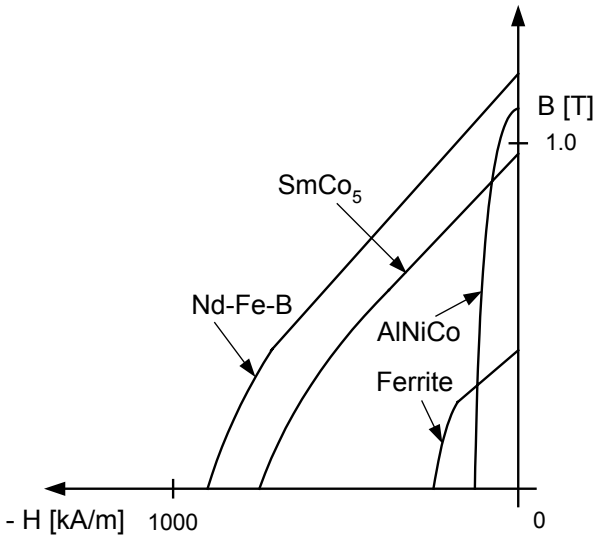

Fig. 5. Characteristics of the common magnetic materials.

C. Induced EMF of the BLDC Generator [10]

In order to control electrical output power of a BLDC generator, it is essential to understand the characteristics of the induced EMF generated in the BLDC generator.

Fig. 6 shows the flux linkage and induced EMF of a single turn coil by the position variation. The flux linkage of a single turn coil is derived as:

$$\lambda_s = (\pi r l) B_f (\theta \,/\, (\pi \,/\, 2)) \qquad (-\pi/2 \le \theta \le \pi/2) \tag{2.1}$$

Where, l, B_f, and θ are rotor length, flux density of the permanent magnet, and rotor position, respectively. According to Faraday's law, the induced EMF is the result of the flux crossing the airgap in a radial direction and cutting the coils of the stator at a rate proportional to the rotor speed:

$$e_s = \frac{d\lambda_s}{dt} = \frac{d\lambda_s}{d\theta} \cdot \frac{d\theta}{dt} = \frac{\pi r l B_f \omega_r}{\pi \,/\, 2} = 2 B_f l r \omega_r \tag{2.2}$$

The magnitude of the total induced EMF with N-turn concentric windings is derived as:

$$E = 2 N_S B_f l r \omega_r \tag{2.3}$$

Where, N_S is the number of turns in a phase winding.

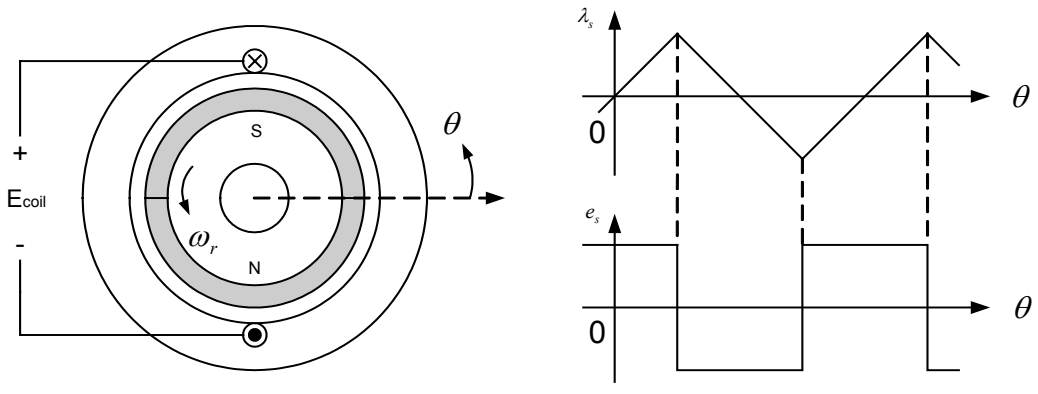

Fig. 6. Induced EMF waveform of a single turn coil.

The induced EMF waveforms of three-phase stator windings are shown in Fig. 7. The sum of EMF that is induced in a N-turn coil generates a trapezoidal waveform with a 60° electrical angle slope region created by stator winding configuration. Each phase is shifted by 120° electrical angles. The distortion of the phase EMF due to many reasons, including manufacturing imperfections (machine geometry, winding, unevenness of the surface of the permanent magnet), leakage flux, and local saturation is neglected. Therefore, the induced EMF waveform is ideally trapezoidal.

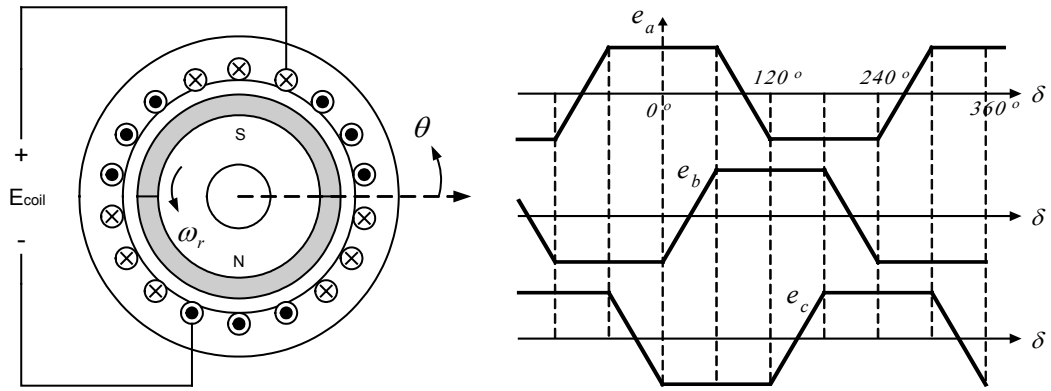

Fig. 7. Induced EMF waveforms of three-phase stator windings.

D. Advantages and Disadvantages of the BLDC Generator [11]-[14]

The BLDC generator offers many advantages such as:

- High efficiency: The BLDC machine is the most efficient of all electric machines since it has a magnetic source inside itself. Use of permanent magnets for the excitation consumes no extra electrical power. Therefore, copper loss of the

exciter does not exist and the absence of mechanical commutator and brushes or slip ring means low mechanical friction losses.

- Compactness: The recent introduction of high-energy density magnets (rare-earth magnets) has allowed achievement of very high flux densities in the BLDC generator. And winding of the rotor is not required. These in turn allow the generator to be small, light and rugged structure.
- Ease of cooling: There is no current circulation in the rotor for magnetic field. Therefore, the rotor of a BLDC generator does not heat up. The only heat production is on the stator, which is easier to cool than the rotor because it is static and on the periphery of the generator.
- Low maintenance, great longevity, and reliability: The absence of brushes, mechanical commutators and slip rings suppresses the need for associated regular maintenance and suppresses the risk of failure associated with these elements. The longevity refers only to the winding insulation, bearing, and magnet life-length.
- Low noise: There is no noise associated with the mechanical contact. The driving converter switching frequency is high enough so that the harmonics are not audible.

Also, the BLDC generator has some inherent disadvantages such as:

- Cost: Permanent magnets are expensive parts in the machine and result in an increased motor cost. The cost of higher energy density magnets prohibits their use in applications where initial cost is a major concern.
- Limited operating-speed range: The field-weakening operation for the BLDC machine is somewhat difficult due to the use of permanent magnets. Some accidental speed increase might damage the power electronic components above the rating of converter, especially for vehicle applications. In addition, the surface-mounted permanent magnet generators cannot reach high speeds because of the limited mechanical strength of the assembly between the rotor yoke and the permanent magnets. There is a possibility of permanent magnets to fly apart.
- Demagnetization of the permanent magnet: Magnets can be demagnetized by large opposing magneto-motive-force (MMF) and high temperatures. The critical demagnetization force is different for each magnet material. Extreme care must be taken to cool the generator, especially if it is compact.

E. Simplified Model of the BLDC Generator [15]-[16]

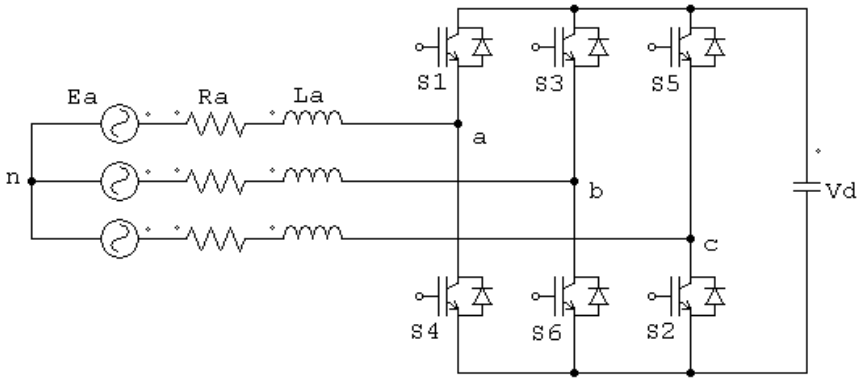

Fig. 8. Equivalent circuit of the BLDC generator.

Fig. 8 shows the equivalent circuit of the BLDC generator. The analysis is based on the following assumptions for simplification:

- The generator is operated within the rated condition, so the generator is not saturated.
- Stator resistances and inductances of all the windings are equal.
- All three phases have an identical induced EMF shape.
- Power semiconductor devices in the converter are ideal.
- Iron losses are negligible.

Phase voltage equations of the BLDC generator can be expressed as:

$$
\begin{aligned}
e_{an} &= R_a i_a + \frac{d}{dt}\left(L_{aa}(\theta, i_a)\cdot i_a + L_{ab}(\theta, i_b)\cdot i_b + L_{ac}(\theta, i_c)\cdot i_c\right) + v_{an} \\
e_{bn} &= R_b i_b + \frac{d}{dt}\left(L_{ba}(\theta, i_a)\cdot i_a + L_{bb}(\theta, i_b)\cdot i_b + L_{bc}(\theta, i_c)\cdot i_c\right) + v_{bn} \\
e_{cn} &= R_c i_c + \frac{d}{dt}\left(L_{ca}(\theta, i_a)\cdot i_a + L_{cb}(\theta, i_b)\cdot i_b + L_{cc}(\theta, i_c)\cdot i_c\right) + v_{cn}
\end{aligned}
\tag{2.4}
$$

Based on the assumptions:

$$
\begin{aligned}
&R_a = R_b = R_c = R \\
&L_{aa} = L_{bb} = L_{cc} = L_s \\
&L_{ba} = L_{ab} = L_{ca} = L_{ac} = L_{bc} = L_{cb} = L_m \\
&L_s - L_m = L \\
&i_a + i_b + i_c = 0
\end{aligned}
\tag{2.5}
$$

Equation (2.4) can be represented as:

$$
\begin{aligned}
e_{an} &= Ri_a + (L_s - L_m)\frac{di_a}{dt} + v_{an} = Ri_a + L\frac{di_a}{dt} + v_{an} \\
e_{bn} &= Ri_b + (L_s - L_m)\frac{di_b}{dt} + v_{bn} = Ri_b + L\frac{di_b}{dt} + v_{bn} \\
e_{cn} &= Ri_c + (L_s - L_m)\frac{di_c}{dt} + v_{cn} = Ri_c + L\frac{di_c}{dt} + v_{cn}
\end{aligned}
\tag{2.6}
$$

$$
e_{xn} = Ri_x + L\frac{di_x}{dt} + v_{xn} \tag{2.7}
$$

Where, e_{xn}, $v_{xn,}$ i_x, R, L, L_s and L_m represent each phase EMF, each phase-to-neutral voltage, each phase current, phase resistance, inductance, self-inductance, and mutual inductance, respectively. EMF calculation can be accomplished by sensing each phase current (i_x) and voltage (v_{xn}). And motion equation can be represented as:

$$
T_{mover} = T_{generator} + B\omega_r + J\frac{d}{dt}\omega_r \Rightarrow \frac{d\omega_r}{dt} = \frac{1}{J}(T_{mover} - T_{generator} - B\omega_r) \tag{2.8}
$$

Where, B and J represent viscous friction and inertia.

G. Conclusion

In this chapter, the basic characteristics of the BLDC generator were described. The mechanical structure of the BLDC generator, along with the induced EMF waveform, was presented. The characteristics of the permanent magnet of the BLDC generator were discussed. Also, a simplified model of the BLDC generator was described. The salient features and advantages of the BLDC generator can be summarized as follows:

- PM machine
- Trapezoidal EMF waveform
- High efficiency
- Lighter, more compact construction
- Low maintenance and greater longevity
- Ease of cooling
- Low noise

In the chapter to follow, conventional rectification methods for the BLDC generator will be presented.

CHAPTER III

CONVENTIONAL RECTIFICATION METHODS FOR THE BLDC GENERATOR

In the previous chapter, characteristics of the BLDC generator were described. From the induced EMF waveform, it is evident that the BLDC generator is a non-sinusoidal AC (Alternating Current) power supply system. PM generators such as BLDC generators are used for small rated power supply systems because of PM, and the electrical output power is charged in the battery as a DC voltage source. Therefore, using an AC-to-DC converter between the BLDC generator and charging equipment is essential. In this chapter, conventional rectification methods for AC-to-DC conversion are described.

A. Conventional Rectification of the Power Supply System

1) Full-bridge diode rectifier [17]

In most power electronics applications, a simple full-bridge diode rectifier is used for the AC-to-DC conversion. Its advantages are:

- Simple construction: A full-bridge diode rectifier has six diodes in one package. No additional hardware is required.

- No control: The diode is a passive element in the power electronics. There is no control to conduct circuits.
- Low cost

However, it has also disadvantages:

- The phase voltage and current is not in phase.
- Current waveform cannot be controlled as ideal waveform, and diode rectifiers draw highly distorted current from the AC side.
- Power per ampere is low because of the uncontrolled current.

Fig. 9 shows the equivalent circuit of the BLDC generator with a diode rectifier. As it can be seen, there is no switch to control the phase current. And rectified electrical power is charged to the battery as a DC voltage source. Fig. 10 shows each phase induced EMF and current waveform of the diode rectifier.

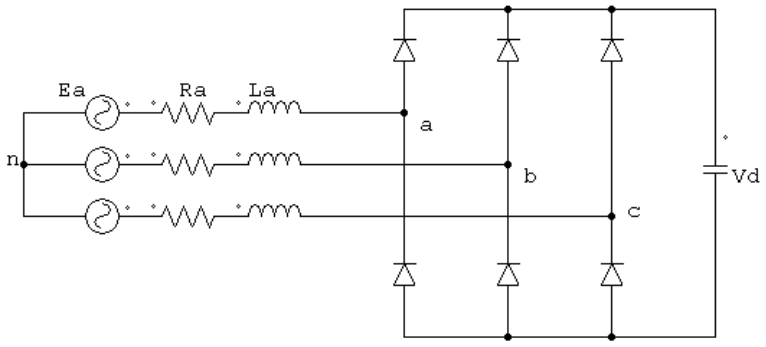

Fig. 9. Equivalent circuit of the BLDC generator with a diode rectifier.

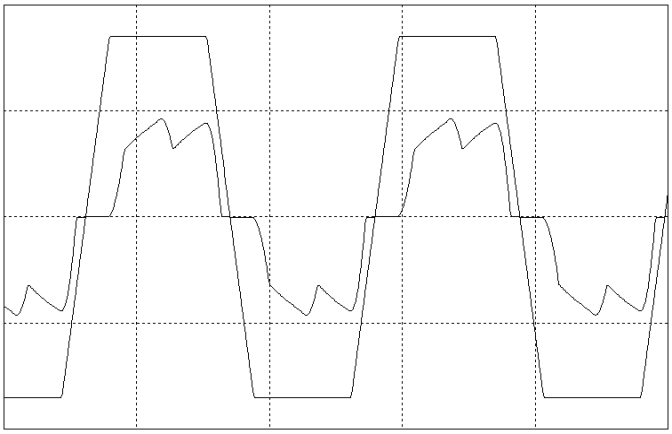

Fig. 10. Phase EMF and current waveform of the full-bridge diode rectifier.

2) PWM rectifier for sinusoidal current waveform [18]-[21]

In a sinusoidal power supply system, a PWM rectifier is used for power factor correction, generally. In the given sinusoidal current reference waveform, six active switches as shown in Fig. 11 can control the current to be in phase with the voltage of the generator. However, note that a BLDC generator is a nonsinusoidal power supply system; therefore, the optimal current waveform for power density maximization is not sinusoidal. Therefore, sinusoidal PWM rectifier cannot make the output power maximum possible.

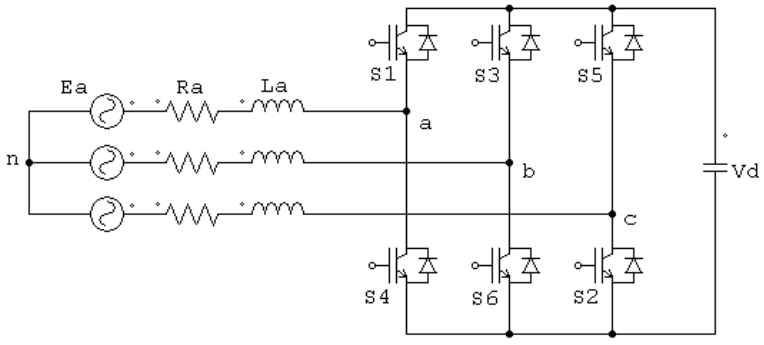

Fig. 11. Equivalent circuit of the BLDC generator with active switches.

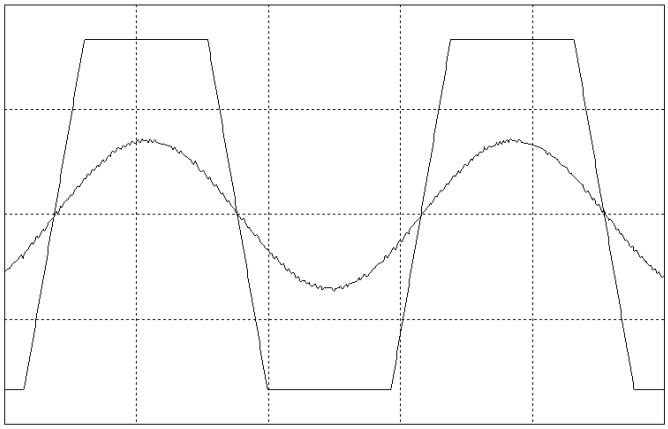

Fig. 12. Phase EMF and current of the sinusoidal PWM rectifier.

B. Conclusion

In this chapter, the conventional rectification methods of the BLDC generator are reviewed. The diode rectifier is simple and cheap, but power per ampere is so low because of the distorted current waveform that it is not suitable for power density maximization. In order to control currents for power density maximization, a PWM rectifier should be used. However, a BLDC generator is a non-sinusoidal system so that optimal current waveform for power density maximization is not sinusoidal but the other waveform. The work presented in this dissertation shows the optimal current waveform by developing a theory based on the induced EMF waveform of the BLDC generator. In the chapter to follow, the details of proposed control for BLDC generators will be presented.

CHAPTER IV

ADVANCED CONTROL FOR POWER DENSITY MAXIMIZATION OF THE BLDC GENERATOR

In the previous chapter, conventional rectification methods are reviewed. The most popular and practical method is to use a diode rectifier for a BLDC generator system. However, since the voltage and current are out-of-phase and current waveform is uncontrolled, the maximum power and efficiency available cannot be achieved. To control the current waveform, a PWM rectifier also has been used. However, a BLDC generator is a non-sinusoidal power supply system from the induced EMF waveform, as shown in Chapter II, and no research has been done for optimal current reference waveform for power density maximization of the non-sinusoidal system.

In this chapter, the derivation of the optimal current waveform of a single-phase BLDC generator and induced EMF calculation are described, first for easy understanding of a three-phase BLDC generator drive, followed by the derivation of the optimal current waveform of the three-phase BLDC generator. The detailed current and voltage controls are presented and the numerical simulation verification of the proposed method is shown.

A. Derivation of the Optimal Current Waveform of a Single-phase BLDC Generator

The induced EMF in the BLDC generator is not a sinusoidal waveform and contains harmonics because it is a trapezoidal waveform due to the machine design and structure described in Chapter II. As it is known, the product of each voltage and current harmonic produces electrical output power. So, we have to consider all the harmonics included. In the single-phase BLDC generator, the average power is presented in (4.1), and phase voltage and current is presented in (4.2):

$$P_{avg} = \frac{1}{T}\int_0^T e(t)i(t)dt \tag{4.1}$$

$$\begin{aligned} e(t) &= E_1 \sin(wt) + E_2 \sin 2(wt) + E_3 \sin 3(wt) + \dots \\ i(t) &= I_1 \sin(wt - \phi_1) + I_2 \sin 2(wt - \phi_2) + I_3 \sin 3(wt - \phi_3) + \dots \end{aligned} \tag{4.2}$$

Where, the capital letters E and I represent the peak magnitude of each harmonic of the voltage and current. ϕ_n represents the phase difference between each voltage and current harmonic. For power density maximization, each voltage and current harmonic should be in phase. Otherwise, the output power has a negative value during every cycle, and the average power cannot be the maximum possible. Therefore, ϕ_n should be zero and the average power is given simply in (4.3):

$$
\begin{aligned}
P_{avg} &= \frac{1}{T}\int_0^T e(t)i(t)dt \\
&= \frac{1}{T}\int_0^T \left[\begin{matrix} \{E_1 \sin(wt) + E_2 \sin 2(wt) + E_3 \sin 3(wt) + \ldots\} \cdot \\ \{I_1 \sin(wt) + I_2 \sin 2(wt) + I_4 \sin 4(wt) + \ldots\} \end{matrix} \right] dt \\
&= \frac{1}{2}(E_1 I_1 + E_2 I_2 + E_3 I_3 + \ldots)
\end{aligned}
\tag{4.3}
$$

Another constraint for power density maximization is the RMS value of the voltage and current. Since the object of this research is to maximize the power density in the generator of the given rating, the RMS value of current and voltage should be maintained at the rated value as in (4.4):

$$
\begin{aligned}
i_{rms} &= \sqrt{\frac{1}{T}\int_0^T i^2(t)dt} = \frac{1}{\sqrt{2}}\sqrt{I_1^2 + I_2^2 + I_3^2 + \ldots} \\
&= \sqrt{i_{1,rms}^2 + i_{2,rms}^2 + i_{3,rms}^2 + \ldots} = \textit{rated value} \\
I_1 &= \sqrt{2i_{rms}^2 - I_2^2 - I_3^2 - \ldots} \\
E_1 &= \sqrt{2e_{rms}^2 - E_2^2 - E_3^2 - \ldots}
\end{aligned}
\tag{4.4}
$$

From equation (4.3) and (4.4), the average power can be given as in (4.5):

$$
P_{avg} = \frac{1}{2}\left[\left(E_1 \cdot \sqrt{2i_{rms}^2 - I_2^2 - I_3^2 - \ldots}\right) + E_2 I_2 + E_3 I_3 + \ldots\right] \tag{4.5}
$$

For maximum power density, the differentiation of average power by the peak value of the each harmonic current should be zero as in (4.6) and the results are shown in (4.7):

$$\frac{\partial P_{avg}}{\partial I_n} = 0 \qquad \mathrm{I}_n : I_1,\ I_2,\ I_3,\ I_4,\ldots$$
$$\frac{\partial P_{avg}}{\partial I_1} = 0\,,\quad \frac{\partial P_{avg}}{\partial I_2} = 0\,,\quad \frac{\partial P_{avg}}{\partial I_3} = 0\,,\quad \frac{\partial P_{avg}}{\partial I_4} = 0\,,\ldots \tag{4.6}$$

$$\Rightarrow I_2 = \frac{I_1}{E_1}E_2\,,\quad I_3 = \frac{I_1}{E_1}E_3\,,\quad I_4 = \frac{I_1}{E_1}E_4\,,\ldots \tag{4.7}$$

By inserting (4.7) into (4.4),

$$\begin{aligned} I_1 &= \sqrt{2i_{rms}^2 - I_2^2 - I_3^2 - \ldots} \\ &= \sqrt{2i_{rms}^2 - \left(\frac{I_1}{E_1}E_2\right)^2 - \left(\frac{I_1}{E_1}E_3\right)^2 - \ldots} \\ &= \sqrt{2i_{rms}^2 - \left(\frac{I_1}{E_1}\right)^2 \cdot (E_2^2 + E_3^2 + \ldots)} \\ &= \sqrt{2i_{rms}^2 - \left(\frac{I_1}{E_1}\right)^2 \cdot (2e_{rms}^2 - E_1^2)} \end{aligned} \tag{4.8}$$

Each harmonic magnitude of the current is:

$$\therefore\ \frac{I_1}{E_1} = \frac{i_{rms}}{e_{rms}} \quad \Rightarrow \quad I_1 = \frac{i_{rms}}{e_{rms}}E_1\,,\quad I_2 = \frac{i_{rms}}{e_{rms}}E_2\,,\quad I_3 = \frac{i_{rms}}{e_{rms}}E_3\,,\ldots \tag{4.9}$$

Therefore, the optimal current waveform for maximum power density in the single-phase BLDC generator of the given rating is:

$$\therefore\quad I_n = \frac{i_{rms}}{e_{rms}}E_n \Rightarrow i(t) = g \cdot e(t) \tag{4.10}$$

Where, g is the gain for the current reference.

B. Induced EMF Calculation of the Single-phase BLDC Generator

In order to implement to the Digital Signal Processor (DSP), a digitized form of the voltage equation for induced EMF calculation is presented in (4.11):

$$\mathrm{E[k]} = R \cdot \left(\frac{i[k] + i[k-1]}{2} \right) + L \cdot \left(\frac{i[k] - i[k-1]}{t[k] - t[k-1]} \right) + V_{dclink} \cdot \left(S_1[k-1] - S_2[k-1] \right) \quad (4.11)$$

Here, phase current is measured by a Hall-effect current sensor, and R, L are known parameters. DC-link voltage is also measured by a Hall-effect voltage sensor and ($S_1[k-1]$-$S_2[k-1]$) is a switching function which is known by current control algorithm. The $S_1[k-1]$ and $S_2[k-1]$ are actually PWM duty ratios that are in between zero and one.

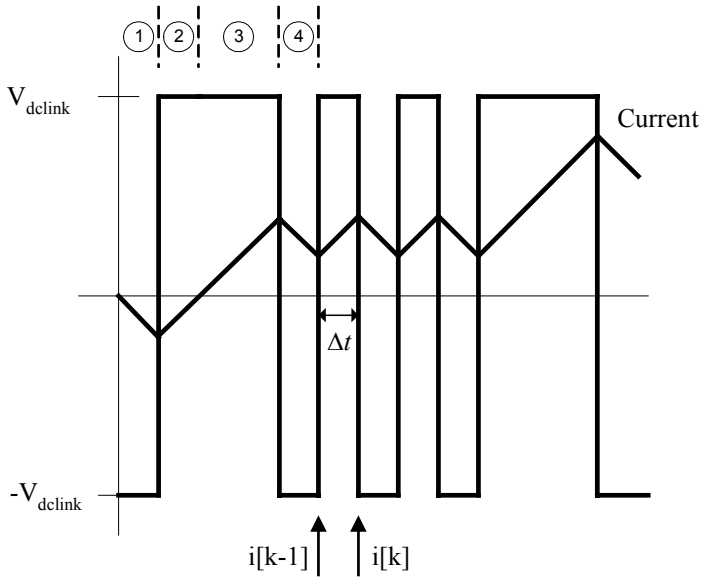

Fig. 13. Multiplication of DC-link voltage and switching function, and instant current waveform.

Fig. 13 shows the multiplication of the sensed DC-link voltage and switching function, and the instant current waveform in each interval. For current control, we are using hysteresis control which will be discussed in section F. Therefore, switching function is known by the switching operation. There are four cases of switching operation as below.

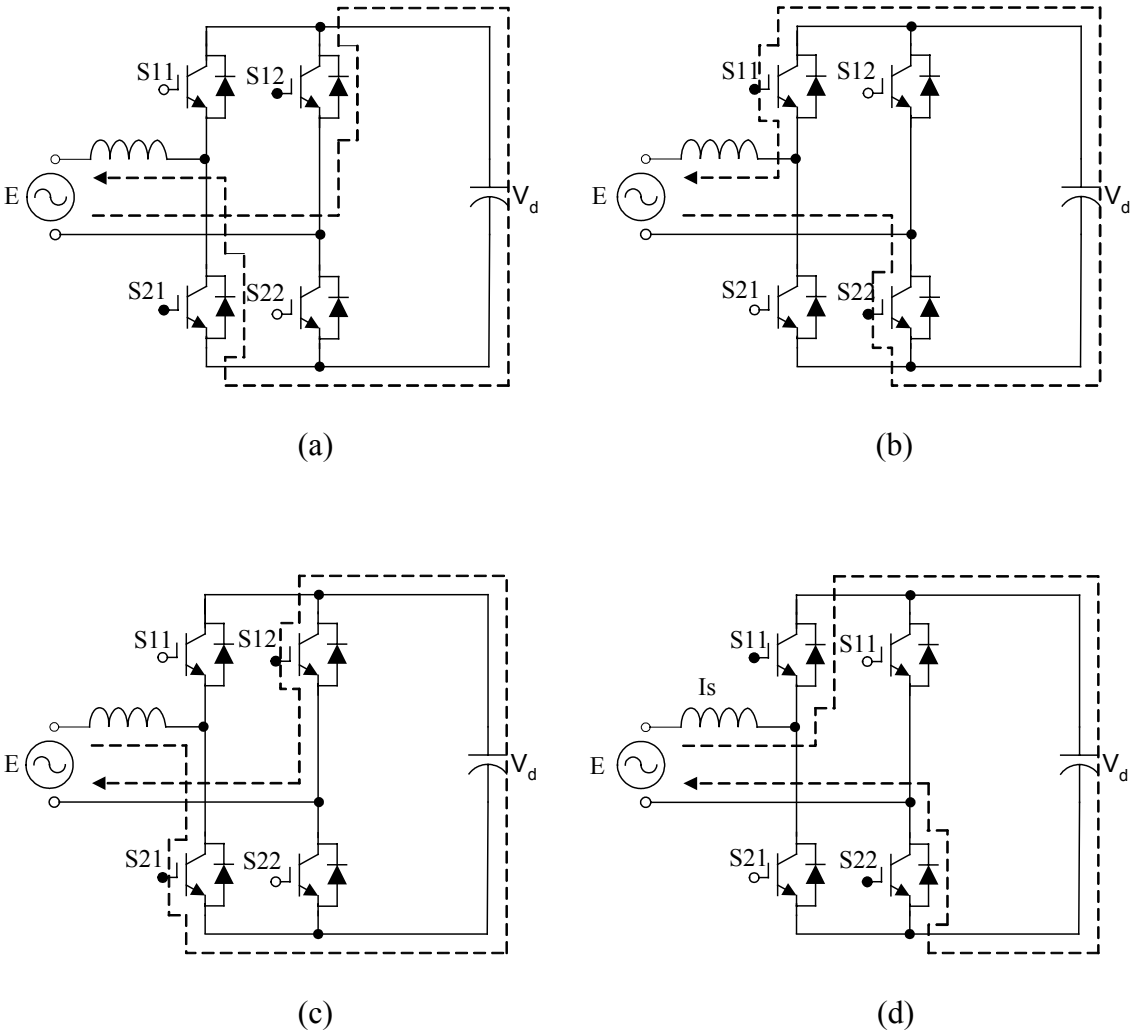

Fig. 14. Single-phase converter circuits and direction of current flow.

In the interval of (1), EMF is negative. If switch 12 and switch 21 are turned on as shown in Fig. 14(a), the current is flowing in negative direction and DC-link voltage is bigger than EMF. Therefore, the current decreases according to (4.12).

$$\begin{aligned} \mathrm{E} &= V_d + L \cdot \frac{di}{dt} \\ \mathrm{E} - V_d &= L \cdot \frac{di}{dt} \quad < \quad 0 \end{aligned} \tag{4.12}$$

In the interval of (2), EMF is still negative. If switch 11 and switch 22 are turned on, as shown in Fig. 14(b), the current is flowing in negative direction and increasing according to (4.13).

$$\begin{aligned} \mathrm{E} &= -V_d + L \cdot \frac{di}{dt} \\ \mathrm{E} + V_d &= L \cdot \frac{di}{dt} \quad > \quad 0 \end{aligned} \tag{4.13}$$

Here, V_d should be always bigger than E for current control.

In the interval of (3), EMF is positive. If switch 12 and switch 21 are turned on, as shown in Fig. 14(c), the current is flowing in positive direction and increasing according to (4.14).

$$\begin{aligned} \mathrm{E} &= -V_d + L \cdot \frac{di}{dt} \\ \mathrm{E} + V_d &= L \cdot \frac{di}{dt} \quad > \quad 0 \end{aligned} \tag{4.14}$$

In the interval of (4), EMF is positive. If switch 11 and switch 22 are turned on, as shown in Fig. 14(d), the current is flowing in positive direction and decreasing according to (4.15).

$$\begin{aligned} \mathrm{E} &= V_d + L \cdot \frac{di}{dt} \\ \mathrm{E} - V_d &= L \cdot \frac{di}{dt} \quad < \quad 0 \end{aligned} \tag{4.15}$$

Therefore, we can control the phase current based on the current reference and the EMF is calculated. Fig. 15 shows the calculated EMF by the voltage equation above. This calculated EMF in the present step is used for the phase current reference of the next step in the single-phase BLDC generator, as in (4.16).

$$i^*[k+1] \quad \Leftarrow \quad E[k] \tag{4.16}$$

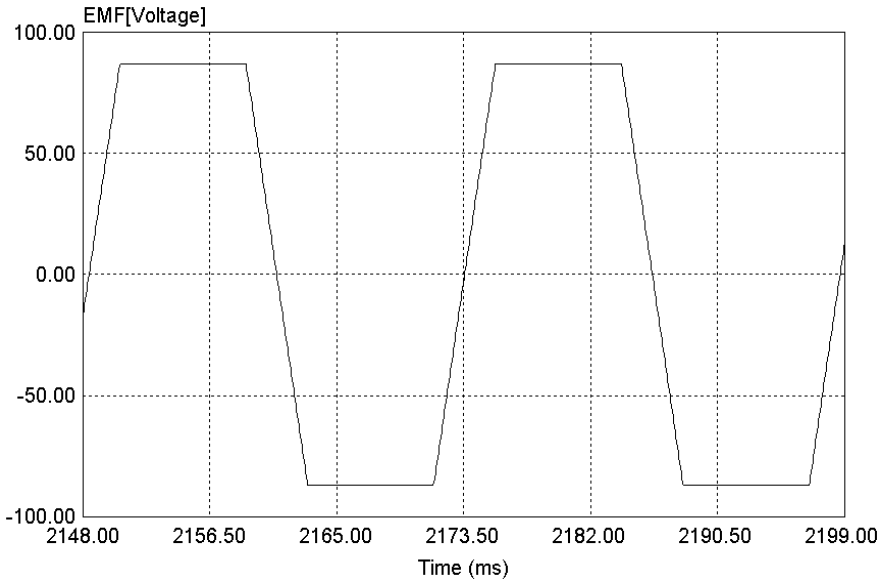

Fig. 15. Calculated EMF waveform using voltage equation.

C. Derivation of the Optimal Current Waveform of a Three-phase BLDC Generator

In the three-phase BLDC generator, we have to consider all harmonics included in the three-phase together. The average power is presented in (4.17), and each phase voltage and current is presented in (4.18):

$$\begin{aligned} P_{avg} &= \frac{1}{T}\int_0^T e(t)i(t)dt \\ &= \frac{1}{T}\int_0^T \{e_a(t)i_a(t) + e_b(t)i_b(t) + e_c(t)i_c(t)\}dt \\ &= \frac{1}{T}\int_0^T e_a(t)i_a(t)dt + \frac{1}{T}\int_0^T e_b(t)i_b(t)dt + \frac{1}{T}\int_0^T e_c(t)i_c(t)dt \\ &= \frac{3}{T}\int_0^T e_a(t)i_a(t)dt \end{aligned} \tag{4.17}$$

$$\begin{aligned} e_a(t) &= E_{a1}\sin(wt) + E_{a2}\sin 2(wt) + E_{a3}\sin 3(wt) + E_{a4}\sin 4(wt) + \dots \\ e_b(t) &= E_{b1}\sin(wt - \frac{2\pi}{3}) + E_{b2}\sin 2(wt - \frac{2\pi}{3}) + E_{b3}\sin 3(wt - \frac{2\pi}{3}) + E_{a4}\sin 4(wt - \frac{2\pi}{3}) + \dots \\ e_c(t) &= E_{c1}\sin(wt - \frac{4\pi}{3}) + E_{c2}\sin 2(wt - \frac{4\pi}{3}) + E_{c3}\sin 3(wt - \frac{4\pi}{3}) + E_{a4}\sin 4(wt - \frac{4\pi}{3}) + \dots \end{aligned} \tag{4.18}$$

$$\begin{aligned} i_a(t) &= I_{a1}\sin(wt - \phi_1) + I_{a2}\sin 2(wt - \phi_2) + I_{a4}\sin 4(wt - \phi_4) + \dots \\ i_b(t) &= I_{b1}\sin(wt - \phi_1 - \frac{2\pi}{3}) + I_{b2}\sin 2(wt - \phi_2 - \frac{2\pi}{3}) + I_{b4}\sin 4(wt - \phi_4 - \frac{2\pi}{3}) + \dots \\ i_c(t) &= I_{c1}\sin(wt - \phi_1 - \frac{4\pi}{3}) + I_{c2}\sin 2(wt - \phi_2 - \frac{4\pi}{3}) + I_{c4}\sin 4(wt - \phi_4 - \frac{4\pi}{3}) + \dots \end{aligned}$$

Where, E and I represent the peak magnitude of each harmonic of the voltage and current, and ϕ_n represents the phase difference between each voltage and current harmonic.

As shown in (4.18), phase current does not contain the multiple of the third harmonic because the current does not have zero-sequence; this zero-sequence is a resultant value when each phase current is summed in the three-phase system. In other words, the sum of the three phase currents should be zero in the Wye connection.

For power density maximization, each voltage and current harmonic should be in phase, the same as a single-phase case. Otherwise, the output power has a negative value during every cycle and the average power cannot be the maximum possible. Therefore, ϕ_n should be zero and the average power is given simply as in (4.19):

$$\begin{aligned} P_{avg} &= \frac{3}{T}\int_0^T e_a(t) i_a(t) dt \\ &= \frac{3}{T}\int_0^T \left[\begin{matrix} \{E_{a1}\sin(wt) + E_{a2}\sin 2(wt) + E_{a3}\sin 3(wt) + \ldots\} \cdot \\ \{I_{a1}\sin(wt) + I_{a2}\sin 2(wt) + I_{a4}\sin 4(wt) + \ldots\} \end{matrix} \right] dt \\ &= \frac{3}{2}(E_{a1}I_{a1} + E_{a2}I_{a2} + E_{a4}I_{a4} + \ldots) \end{aligned} \tag{4.19}$$

Another constraint for power density maximization is the RMS value of the voltage and current. Since the object of this research is to maximize the power density in the generator of a given rating, the RMS value of current and voltage should be maintained at the rated value as in (4.20):

$$\begin{aligned} i_{a,rms} &= \sqrt{\frac{1}{T}\int_0^T i_a^2(t) dt} = \frac{1}{\sqrt{2}}\sqrt{I_{a1}^2 + I_{a2}^2 + I_{a4}^2 + \ldots} \\ &= \sqrt{i_{a1,rms}^2 + i_{a2,rms}^2 + i_{a4,rms}^2 + \ldots} = \textit{rated value} \\ I_{a1} &= \sqrt{2i_{a,rms}^2 - I_{a2}^2 - I_{a4}^2 - \ldots} \\ E_{a1} &= \sqrt{2e_{a,rms}^2 - E_{a2}^2 - E_{a3}^2 - E_{a4}^2 - \ldots} \end{aligned} \tag{4.20}$$

From (4.19) and (4.20), the average power can be given as in (4.21):

$$P_{avg} = \frac{3}{2}[\left(E_{a1} \cdot \sqrt{2i_{a,rms}^2 - I_{a2}^2 - I_{a4}^2 - \ldots}\right) + E_{a2}I_{a2} + E_{a4}I_{a4} + \ldots] \tag{4.21}$$

For maximum power density, the differentiation of average power by the peak value of the each harmonic current should be zero, as in (4.22), and the results are shown in (4.23):

$$\begin{aligned} &\frac{\partial P_{avg}}{\partial I_{an}} = 0 \qquad\qquad \mathrm{I}_{an} : I_{a1},\ I_{a2},\ I_{a4},\ I_{a5}, \ldots \\ &\frac{\partial P_{avg}}{\partial I_{a1}} = 0\,, \quad \frac{\partial P_{avg}}{\partial I_{a2}} = 0\,, \quad \frac{\partial P_{avg}}{\partial I_{a4}} = 0\,, \quad \frac{\partial P_{avg}}{\partial I_{a5}} = 0\,, \ldots \end{aligned} \tag{4.22}$$

$$\Rightarrow I_{a2} = \frac{I_{a1}}{E_{a1}}E_{a2}\,,\ \ I_{a4} = \frac{I_{a1}}{E_{a1}}E_{a4}\,,\ \ I_{a5} = \frac{I_{a1}}{E_{a1}}E_{a5}\,, \ldots \tag{4.23}$$

By inserting (4.23) into (4.20), the result is (4.24):

$$\begin{aligned} I_{a1} &= \sqrt{2i_{a,rms}^2 - I_{a2}^2 - I_{a4}^2 - \ldots} \\ &= \sqrt{2i_{a,rms}^2 - \left(\frac{I_{a1}}{E_{a1}}\right)^2 \cdot (E_{a2}^2 + E_{a4}^2 + \ldots)} \\ &= \sqrt{2i_{a,rms}^2 - \left(\frac{I_{a1}}{E_{a1}}\right)^2 \cdot (2e_{a,rms}^2 - E_{a1}^2 - E_{a3}^2 - E_{a6}^2 - \ldots)} \end{aligned}$$

$$2i_{a,rms}^2 = \left(\frac{I_{a1}}{E_{a1}}\right)^2 (2e_{a,rms}^2 - E_{a3}^2 - E_{a6}^2 - \ldots) \tag{4.24}$$

Here, we define the function $e_{am}(t)$ as the following (4.25),

$$\begin{aligned} e_{am}(t) &= e_a(t) - \textit{multiple of triple harmonic} \\ &= E_{a1}\sin(wt) + E_{a2}\sin(2wt) + E_{a4}\sin(4wt) + \ldots \end{aligned} \tag{4.25}$$

From (4.20) and (4.25), we can derive (4.26).

$$2e_{a,rms}^2 = \underbrace{E_{a1}^2 + E_{a2}^2 + E_{a4}^2 + \ldots}_{2e_{am,rms}^2} + \underbrace{E_{a3}^2 + E_{a6}^2 + \ldots}$$

$$2e_{am,rms}^2 = 2e_{a,rms}^2 - E_{a3}^2 - E_{a6}^2 - \ldots \tag{4.26}$$

By inserting (4.26) into (4.24), each harmonic magnitude of the phase current should be (4.27):

$$\begin{aligned} &\therefore \ \frac{I_{a1}}{E_{a1}} = \frac{i_{a,rms}}{e_{am,rms}} \\ &\Rightarrow I_{a1} = \frac{i_{a,rms}}{e_{am,rms}} E_{a1}, \ \ I_{a2} = \frac{i_{a,rms}}{e_{am,rms}} E_{a2}, \ \ I_{a4} = \frac{i_{a,rms}}{e_{am,rms}} E_{a4}, \ldots \\ &\Rightarrow I_{an} = \frac{i_{a,rms}}{e_{am,rms}} E_{an} \end{aligned} \tag{4.27}$$

Therefore, the optimal current waveform for maximum power density in the same rated three-phase BLDC generator is:

$$\therefore \ \ i_{abc}(t) = g \cdot e_{abcm}(t) \tag{4.28}$$

Where, g is the gain for the current reference.

In the above equation, the optimal current waveform for power density maximization of the BLDC generator has been derived. The average power we mentioned in this research is the airgap average power because it is from the product of each phase airgap voltage (EMF) and current, as in (4.17).

$$\begin{aligned} P_{avg} &= \frac{1}{T}\int_0^T e(t)i(t)dt \\ &= \frac{1}{T}\int_0^T \{e_a(t)i_a(t) + e_b(t)i_b(t) + e_c(t)i_c(t)\}dt \\ &= \frac{1}{T}\int_0^T e_a(t)i_a(t)dt + \frac{1}{T}\int_0^T e_b(t)i_b(t)dt + \frac{1}{T}\int_0^T e_c(t)i_c(t)dt \\ &= \frac{3}{T}\int_0^T e_a(t)i_a(t)dt \end{aligned} \tag{4.17}$$

However, power used practically is not the airgap power but the terminal output power as shown in Fig. 16. Therefore, the investigation into whether or not the airgap power density maximization is the terminal output power density maximization should be done.

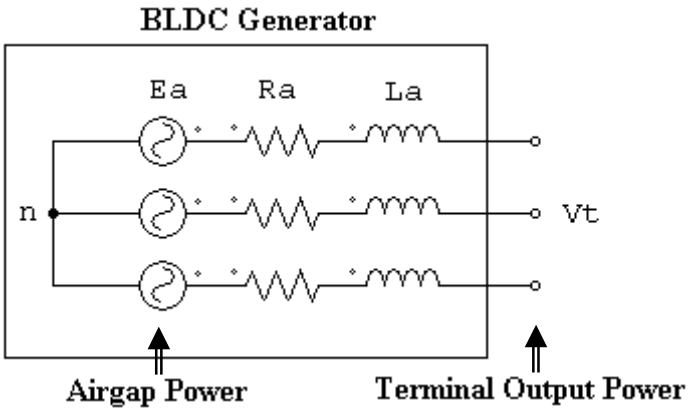

Fig. 16. Airgap power and terminal output power of the BLDC generator.

Voltage equation of the BLDC generator is:

$$v_t(t) = e(t) - R \cdot i(t) - L\frac{di(t)}{dt} \tag{4.29}$$

Terminal output power is presented as:

$$\begin{aligned} P_{\text{terminal}} &= \frac{1}{T}\int_0^T v_t(t) i(t) dt \\ &= \frac{1}{T}\int_0^T \left\{ e(t) - R \cdot i(t) - L\frac{di(t)}{dt} \right\} \cdot i(t) dt \end{aligned} \tag{4.30}$$

And this terminal output power is categorized by airgap power, resistive loss or copper loss, and inductive component:

$$P_{\text{terminal}} = \frac{1}{T}\int_0^T e(t) \cdot i(t) dt - \frac{1}{T}\int_0^T R \cdot i^2(t) dt - \frac{1}{T}\int_0^T L\frac{di(t)}{dt} \cdot i(t) dt \tag{4.31}$$

Because resistive loss is a constant value in the rated RMS current and the average power of the inductive component is null, the terminal output power can be written simply as:

$$\begin{aligned} P_{\text{terminal}} &= \underbrace{\frac{1}{T}\int_0^T e(t) \cdot i(t) dt}_{\text{airgap power}} - \underbrace{R \cdot i_{rms}^2}_{\substack{\text{constant} \\ \text{value}}} - \underbrace{\frac{L}{T}\int_0^T i'(t) \cdot i(t) dt}_{0} \\ &= \frac{1}{2}(E_1 I_1 + E_2 I_2 + E_3 I_3 + \ldots) - R \cdot i_{rms}^2 \end{aligned} \tag{4.32}$$

In a certain equation, if one component is maximized and the other is a constant value, the output of the equation is maximized.

$$Maximum = Maximum - Constant\ value$$

Therefore, it is clear that the airgap power density maximization is the terminal output power density maximization.

Maximum power density in the non-sinusoidal system is accomplished by matching all the harmonics of the current with those of the induced EMF except the zero-sequence component. Here, knowing each harmonic of the EMF except zero-sequence component is very difficult without an FFT (Fast Fourier Transform), which is time-consuming and complicated. Another way to accomplish this task without an FFT is to use the linear tracking method; That is, to make the current waveform track the calculated zero-sequence free EMF waveform. In section E, simple algebraic method to eliminate the zero-sequence component in the three-phase BLDC generator will be presented.

D. Induced EMF Calculation of the Three-phase BLDC Generator

In order to implement the proposed algorithm to the Digital Signal Processor (DSP), a digitized form of the voltage equation for induced EMF calculation in the three-phase BLDC generator is presented as:

$$\begin{aligned} \mathrm{E_{ab}[k]} &= R \cdot \left(i_a[k] + i_b[k]\right) \\ &+ L \cdot \left(\frac{\left(i_a[k] - i_a[k-1]\right) - \left(i_b[k] - i_b[k-1]\right)}{t[k] - t[k-1]} \right) + V_{dclink} \cdot \left(S_a[k-1] - S_b[k-1]\right) \end{aligned} \tag{4.33}$$

Where, the phase current is measured by a Hall-effect current sensor and R, L are known parameters. DC-link voltage is also measured by a Hall-effect voltage sensor and (S_a*[k-1]*-S_b*[k-1]*) is a switching function which is known by current control algorithm.

The di/dt terms in (4.11) and (4.33) are very sensitive parts from the measurement error of the current, and need a special algorithm to reduce the possible error. In this research, an Infinite Impulse Response (IIR) filter and the sparse calculation method are used to reduce the EMF estimation errors due to measured currents. The noise of the sampled phase currents can lead to a large estimation error. Therefore, it is required to filter out the signal noise. Since the noise is usually caused by the switching of the converter, an IIR low-pass filter is a good candidate to reduce it. This low-pass filter is in the following form:

$$I_{f[k]} = \alpha \cdot I_{f[k-1]} + \beta \cdot I_{s[k]} \tag{4.34}$$

Where, I_f and I_s represent the filtered and sampled currents. The transfer function of the filter in z domain is:

$$H\left(z^{-1}\right) = \frac{\beta}{1 - \alpha \cdot z^{-1}} \tag{4.35}$$

Based on the desired cut-off frequency in s-domain, the filter is designed and the coefficients, α and β are calculated.

The designed filter is transformed to z-domain using the well-known bilinear transformation:

$$s = \frac{2}{T} \cdot \frac{1 - z^{-1}}{1 + z^{-1}} \tag{4.36}$$

Where, T is the sampling time. As mentioned earlier, the di/dt terms in (4.11) and (4.33) amplify the measured current error. Even if the measured current is filtered out using the low-pass filter, the small time interval, dt, can cause significant EMF estimation error.

To further decrease the error of di/dt term, the sparse calculation method is developed. If the sampling frequency is selected as 20 kHz, one sampling period is 50 μ seconds. The very small time difference, such as 50 μ seconds, seriously amplifies the di/dt term error. Therefore, to increase the time difference in the di/dt term, the calculation frequency of the EMF is selected as much lower than that of the sampling frequency of the current.

Fig. 17 shows the calculated line-to-line EMF by using the voltage equation described above. This calculated line-to-line EMF in the present step is used for each phase current reference of the next step, as in (4.37).

$$i^*_{phase}[k+1] \quad \Leftarrow \quad E_{l-l}[k] \tag{4.37}$$

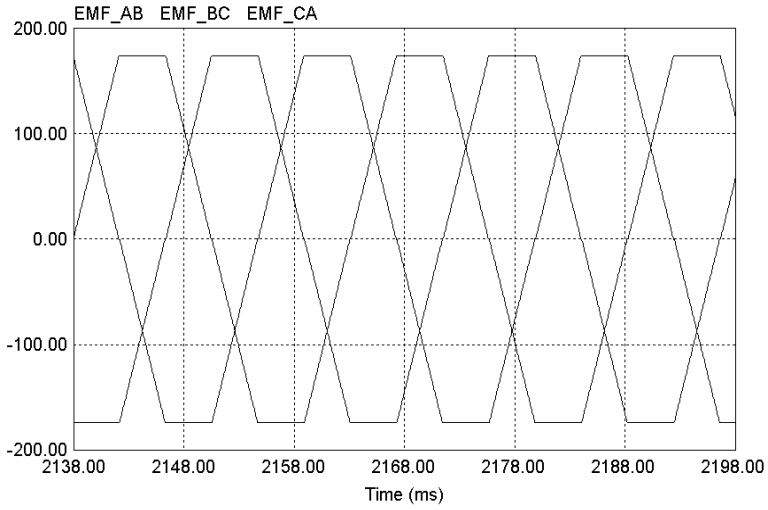

Fig. 17. Calculated line-to-line EMF waveform using voltage equation.

E. Zero-squence Elimination of the Three-phase BLDC Generator

To create optimal current waveform for power density maximization in the three-phase BLDC generator, the zero-sequence component should be eliminated from the phase EMF waveform as we derived in the previous section. This zero-sequence component does not contribute to the total power because the electrical output power is produced by the product of each voltage and current harmonic, and zero-sequence of the current is null according to Kirchhoff's law as mentioned before.

In order to eliminate the specific harmonic, zero-sequence, we propose simple algebraic method as in (4.41). Each phase EMF has harmonics as 1^{st}, 3^{rd}, 5^{th},… and the sum of three phase EMFs can be categorized by zero and zero-sequence component as in (4.38). This zero sequence is a multiple of the third harmonic so that it is identical as in

(4.39). By inserting (4.39) into (4.38), the component that does not have zero-sequence can be derived in (4.40). The line-to-line EMFs are used in (4.41) because some manufacturers do not provide a neutral point.

$$\begin{aligned} e_a &= e_{a1} + e_{a3} + e_{a5} + \ldots = e_{am} + e_{az} \\ e_b &= e_{b1} + e_{b3} + e_{b5} + \ldots = e_{bm} + e_{bz} \qquad \mathrm{m} = 1, 5, 7, 11, \ldots \\ e_c &= e_{c1} + e_{c3} + e_{c5} + \ldots = e_{cm} + e_{cz} \qquad \mathrm{z} = 3, 9, 15, 21, \ldots \\ e_a + e_b + e_c &= \underbrace{e_{am} + e_{bm} + e_{cm}}_{0} + \underbrace{e_{az} + e_{bz} + e_{cz}}_{\text{zero sequence}} \end{aligned} \tag{4.38}$$

$$\begin{aligned} & e_{az} = e_{bz} = e_{cz} = e_z \\ & \Rightarrow e_z = \frac{1}{3}(e_a + e_b + e_c) \end{aligned} \tag{4.39}$$

$$\begin{aligned} e_{am} &= e_a - e_z = e_a - \frac{1}{3}(e_a + e_b + e_c) \\ e_{bm} &= e_b - e_z = e_b - \frac{1}{3}(e_a + e_b + e_c) \\ e_{cm} &= e_c - e_z = e_c - \frac{1}{3}(e_a + e_b + e_c) \end{aligned} \tag{4.40}$$

Therefore, each phase optimal current reference for power density maximization of the three-phase BLDC generator is:

$$\begin{bmatrix} i_a^* \\ i_b^* \\ i_c^* \end{bmatrix} = g \cdot \begin{bmatrix} e_{am} \\ e_{bm} \\ e_{cm} \end{bmatrix} = g \cdot \frac{1}{3} \begin{bmatrix} e_a - e_b + e_a - e_c \\ e_b - e_a + e_b - e_c \\ e_c - e_a + e_c - e_b \end{bmatrix} = \frac{g}{3} \begin{bmatrix} 1 & 0 & -1 \\ -1 & 1 & 0 \\ 0 & -1 & 1 \end{bmatrix} \begin{bmatrix} e_{ab} \\ e_{bc} \\ e_{ca} \end{bmatrix} \tag{4.41}$$

Here, g is a proportional gain from the voltage controller. This simple algebraic method removes the burden of the FFT and provides the optimal current waveform from the calculated line-to-line EMF directly.

F. Current and Voltage Control of the BLDC Generator Drive [22]-[23]

To control currents, a conventional controller such as a PID controller or a hysteresis controller can be used for the proposed method. In general motion-control systems, the P controllers in the position loop and the PI controllers in the speed and current control loop are often adequate [13]. Therefore, the differential (D) controllers are not considered. The other consideration is a hysteresis controller. The advantages of the hysteresis controller are fast transient response and simple implementation. However, the current ripple in transient state is a disadvantage of the controller. Compared to the hysteresis controller, the advantage of the PI controller is the zero steady-state error. On the other hand, the transient response is slower than that of the hysteresis controller. In general, since generators operate at high speed and current reference for power density maximization is not a constant value but a function, a PI controller is not suitable for current control of the generator. However, a PI controller is adequate to control battery voltage which does not need a fast transient response. In this research, to control the current, the hysteresis controller is used, and to control the voltage, the PI controller is used.

Fig. 18(a) shows the DC-link voltage and resultant current which follows the current reference based on the upper and lower limit of the hysteresis band. Also, Fig. 18(b) shows a controlled phase current of the BLDC generator by using the hysteresis controller. The current waveform in Fig. 18(b) is the proposed optimal current waveform which will be shown in the next section G.

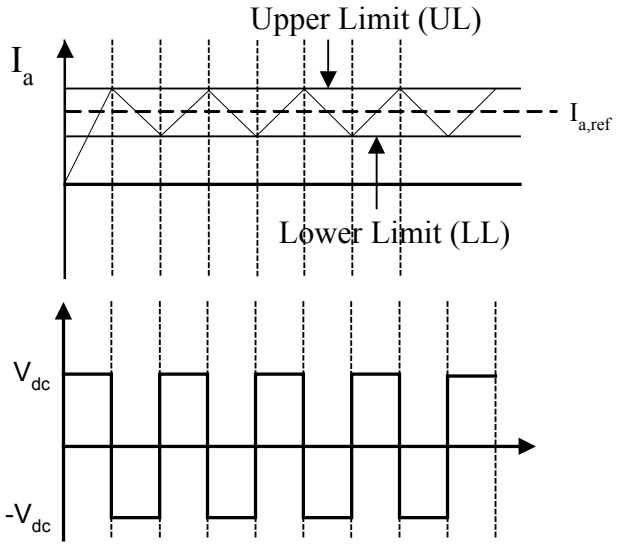

(a) Principle of the hysteresis controller

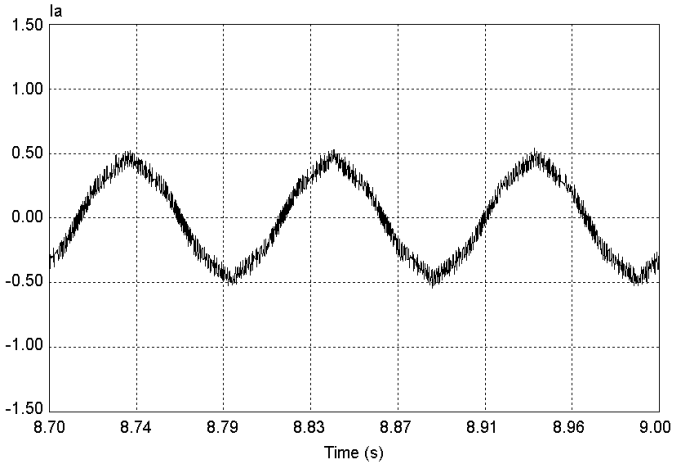

(b) Current response

Fig. 18. Hysteresis current controller and current response.

For the voltage regulation, a PI controller is used. (4.42) shows the transfer function of the PI controller.

$$G_c(s) = k_p + \frac{k_I}{s} \tag{4.42}$$

The digitized form of the transfer function using the bilinear transformation is shown in (4.43):

$$Y[K+1] = Y[K] + k_P \cdot [u[K+1] - u[K]] + \frac{k_I \cdot T_s}{2} \cdot [u[K+1] + u[K]] \qquad (4.43)$$

Where u, Y, and T_s stand for the input, output, and sampling time of the PI controller, respectively. Fig. 19 shows a DC-link voltage response with the PI controller.

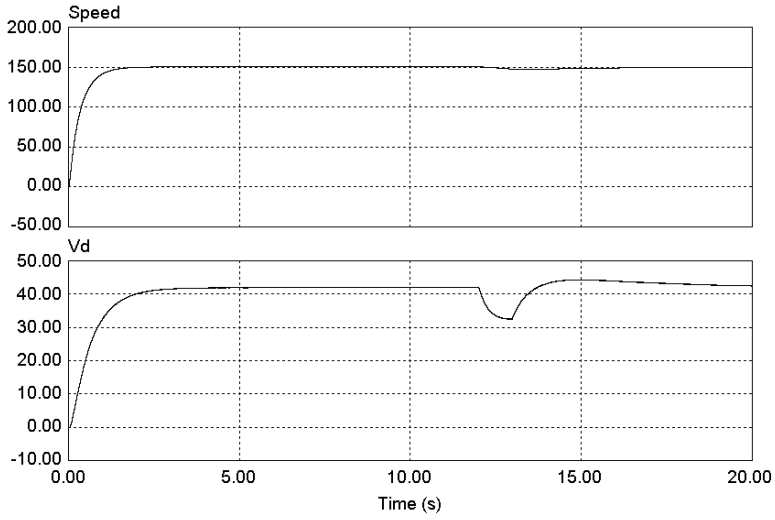

Fig. 19. Voltage response of the PI controller.

G. Simulation Verification of the Proposed Control

After the power density maximization control algorithm is formulated, the next step is to perform numerical simulations in order to observe the operation of the control algorithm and to validate the theory proposed. To develop a simulation model of the BLDC generator system, the dynamic equations of the system are formulated in section

E, Chapter II. Each phase of the BLDC generator is represented by a voltage equation that includes EMFs, resistive and inductive drops, and the DC-link voltage. The voltage equations of three phases are:

$$\begin{aligned} e_{an} &= R_a i_a + \frac{d}{dt}\left(L_{aa}(\theta, i_a)\cdot i_a + L_{ab}(\theta, i_b)\cdot i_b + L_{ac}(\theta, i_c)\cdot i_c\right) + v_{an} \\ e_{bn} &= R_b i_b + \frac{d}{dt}\left(L_{ba}(\theta, i_a)\cdot i_a + L_{bb}(\theta, i_b)\cdot i_b + L_{bc}(\theta, i_c)\cdot i_c\right) + v_{bn} \\ e_{cn} &= R_c i_c + \frac{d}{dt}\left(L_{ca}(\theta, i_a)\cdot i_a + L_{cb}(\theta, i_b)\cdot i_b + L_{cc}(\theta, i_c)\cdot i_c\right) + v_{cn} \end{aligned} \tag{2.4}$$

The EMFs can be represented using the Fourier expression as:

$$\begin{aligned} e_a &= 2\cdot B_g \cdot r \cdot l \cdot \omega_r \cdot N_a \cdot \sum_{n=1}^{\infty} A_n \cdot \cos[n(\theta)] \\ e_b &= 2\cdot B_g \cdot r \cdot l \cdot \omega_r \cdot N_b \cdot \sum_{n=1}^{\infty} A_n \cdot \cos\left[n\left(\theta - \frac{2\pi}{3}\right)\right] \\ e_c &= 2\cdot B_g \cdot r \cdot l \cdot \omega_r \cdot N_c \cdot \sum_{n=1}^{\infty} A_n \cdot \cos\left[n\left(\theta + \frac{2\pi}{3}\right)\right] \end{aligned} \tag{4.44}$$

Where, B_g, r, l, ω_r, N_a, A_n, and θ are air-gap flux density, rotor radius, stack length, speed, number of turns for phase A, n_{th} harmonic coefficient, and rotor position, respectively. And motion equation of the system can be represented as:

$$T_{mover} = T_{generator} + B\omega_r + J\frac{d}{dt}\omega_r \Rightarrow \frac{d\omega_r}{dt} = \frac{1}{J}(T_{mover} - T_{generator} - B\omega_r) \tag{2.8}$$

$$\omega_r = \frac{d\theta}{dt} \tag{4.45}$$

Where, B and J represent viscous friction and inertia.

These complete the dynamic equations of the simulation model. In this research, the PSIM (simulation package for power electronics and motor control) is used to simulate the BLDC generator system. To perform simulation, a fixed time step of 50 μ second is used in order to have a fixed sampling of 20 kHz. Every 50 μ seconds, the current and DC-link voltage are sampled and stored to use for the EMF calculation algorithm. For this simulation, the test-bed BLDC generator model is used which has the following specifications. Table II shows the specification of the BLDC generator.

Table II. Specification of the BLDC generator.

Pole	4	Resistance	4.3[Ω]
Phase	3	Inductance	43[mH]
Power	0.75[kW]	K_e	1.29[V/rps]
DC–link Battery	7200[μF]	Rated Current	5.0[A]

Fig. 20 shows the system configuration with a diode rectifier. The prime mover is a separately excited DC motor.

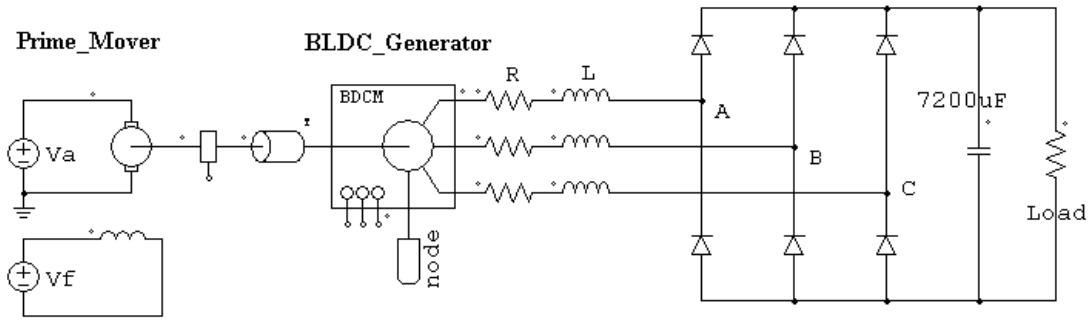

Fig. 20. System configuration with a diode rectifier.

Fig. 21 and Fig. 22 show the simulation results with the diode rectifier for an operating point at 300 RPM. The induced EMF is assumed as an ideal trapezoidal waveform, as shown in Fig. 21. The current waveform is not controlled and has a ripple. Since it is not an optimal current waveform and the current is out of phase with EMF, the average power cannot be the maximum possible.

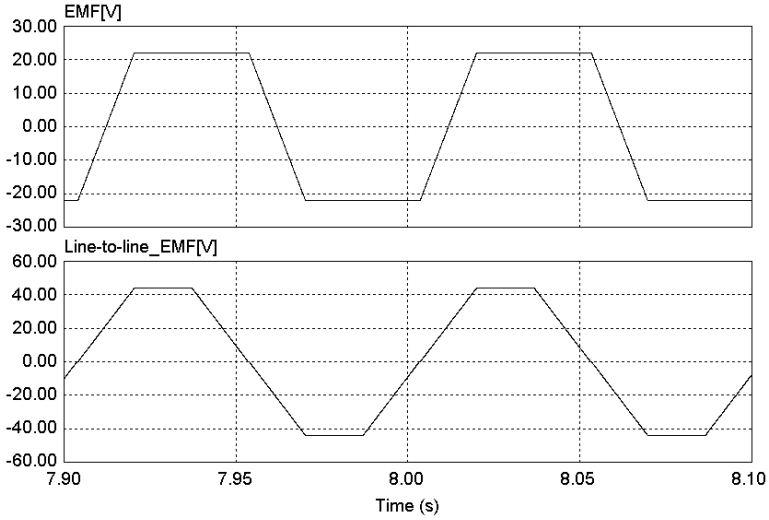

Fig. 21. Simulated phase EMF and line-to-line EMF at 300 RPM.

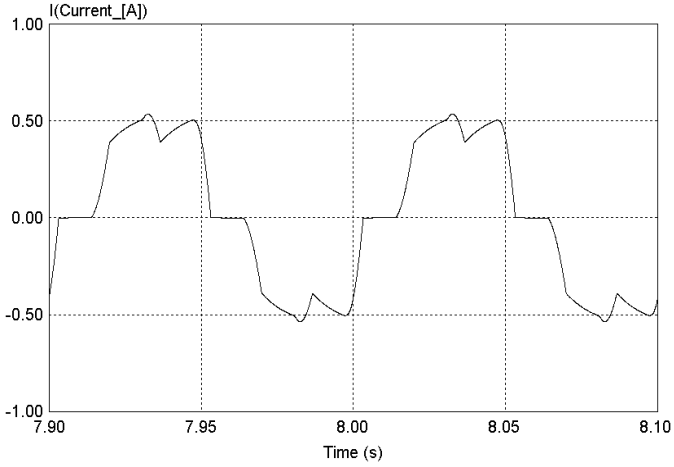

Fig. 22. Simulated phase current at 300 RPM.

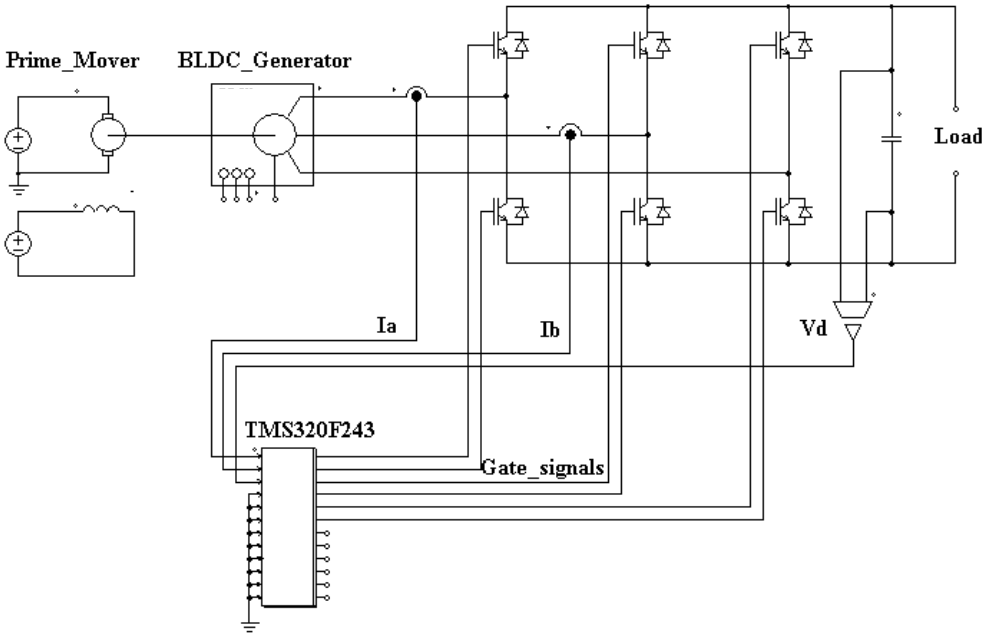

Fig. 23. System configuration with a controlled converter.

Fig. 23 shows the system configuration with an active converter. Each-phase current and battery voltage are measured by the Hall-effect sensors for EMF calculation and current control. Outputs of the controller provide six gate signals for each switch. Figs. 24 through 28 show the simulation results for an operating point at 300 RPM. As was mentioned before, the optimal current reference waveform for maximizing power density does not have multiple of the third harmonic, a zero-sequence component. Fig. 24 shows the phase EMF waveform and zero-sequence eliminated EMF waveform by using the proposed simple algebraic method in (4.41). And Fig. 25 shows the result of frequency analysis of the EMF and zero-sequence eliminated EMF to confirm that the multiple of the third harmonic is removed. The fundamental frequency is 10Hz. The

circles show the third and ninth harmonic components. It is clear that using simple algebraic method without requiring a FFT has eliminated the zero-sequence component from the trapezoidal EMF.

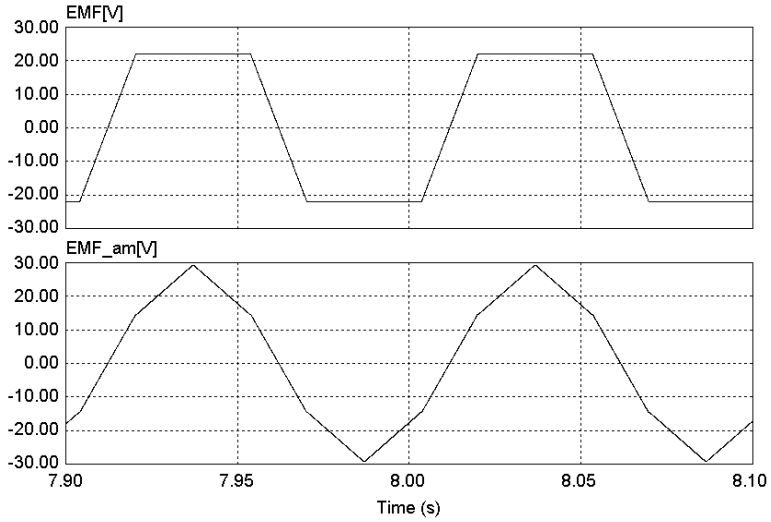

Fig. 24. Simulated phase EMF and zero-sequence eliminated-phase EMF.

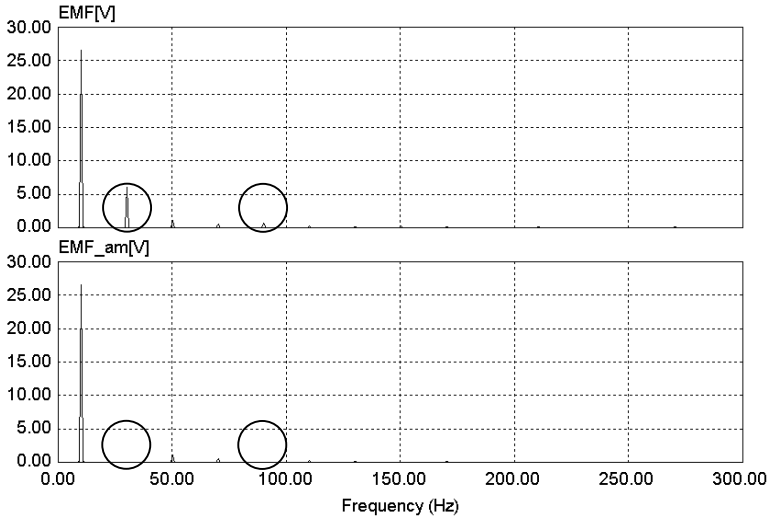

Fig. 25. Frequency analysis of phase EMF and zero-sequence eliminated-phase EMF.

Fig. 26 shows the three-phase zero-sequence eliminated EMFs. They are similar as sinusoidal waveforms. However, they have all harmonics except multiple of the third harmonic. Optimal current reference waveform and controlled phase current are shown in Fig. 27. A hysteresis controller is used for current control and the band of the controller (upper limit or lower limit from the reference in Fig. 18(a)) is 0.05A.

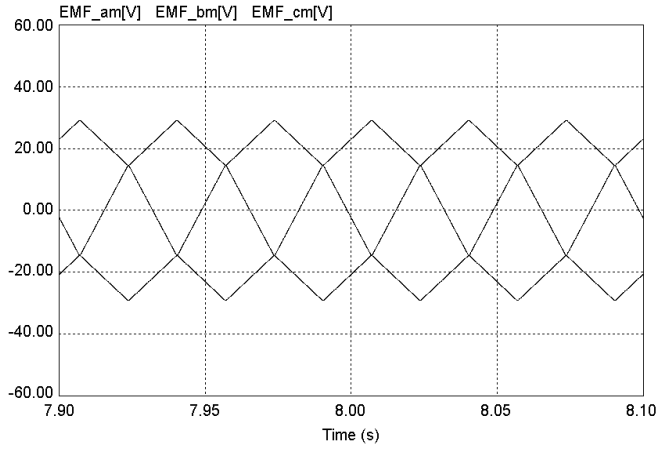

Fig. 26. Zero-sequence eliminated three-phase EMFs.

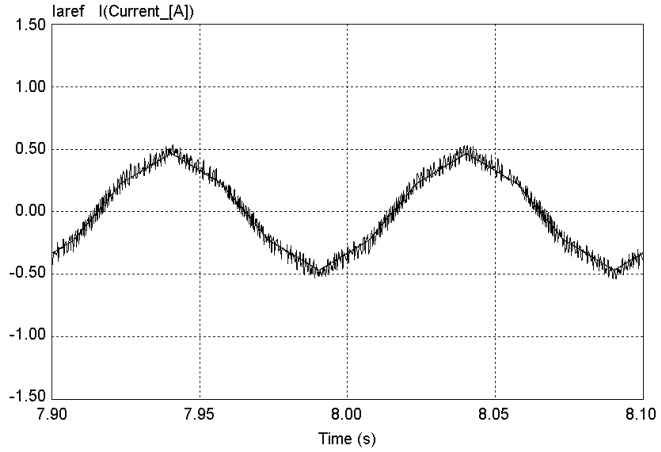

Fig. 27. Optimal current reference waveform and controlled current for power density maximization at 300 RPM.

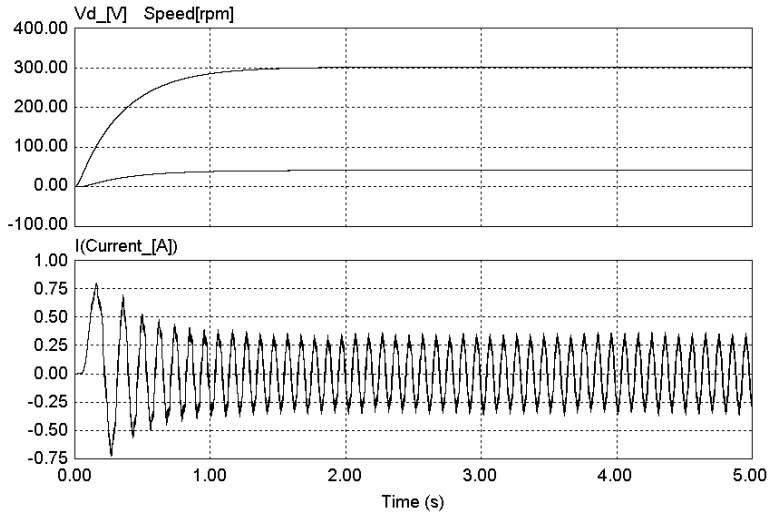

Fig. 28. Transient response with the PI voltage controller and hysteresis current controller.

The performance of the drive during transient period is also simulated. Fig. 28 shows the phase current and voltage response with the PI voltage controller and hysteresis current controller. The output of the PI controller is the magnitude of the current reference and the waveform of the current reference comes from (4.41).

Since the objective of this research is to maximize the power density in the generator of given rating, performance analysis in the rated current, 5A should be simulated. Fig. 29 and 30 show the simulation results with a diode rectifier for an operating point at 1350 RPM and rated current 5A.

As shown in Fig. 30, the phase current is almost sinusoidal waveform, and it is out of phase with phase EMF compared with Fig. 22, because of the high-speed operation.

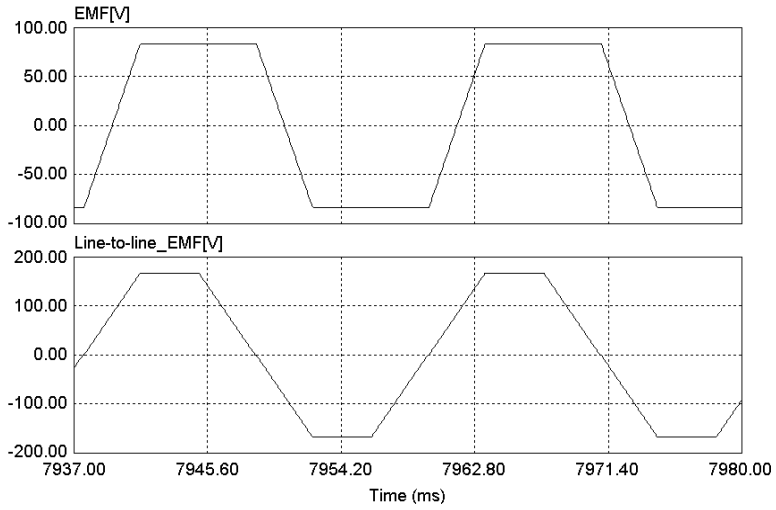

Fig. 29. Simulated phase EMF and line-to-line EMF.

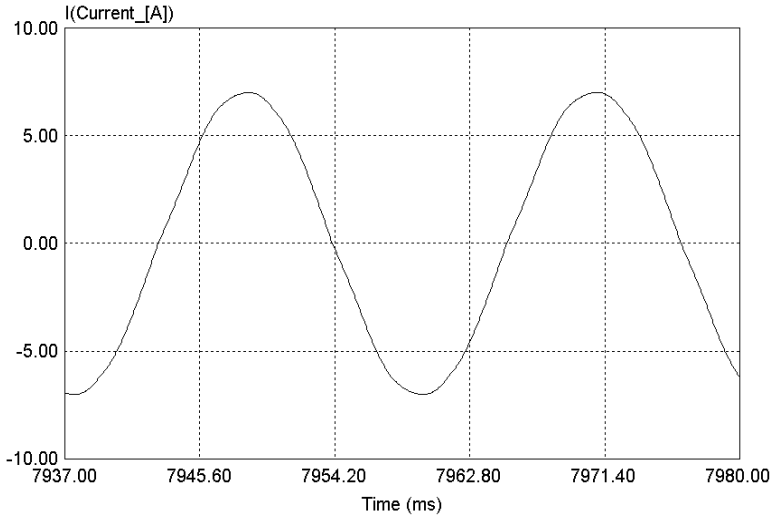

Fig. 30. Simulated phase current at 1350 RPM.

As the inductance of the generator and the speed of the rotor increase, the out-of-phase phenomenon between induced voltage and current is prominent in (4.46) and Fig. 31. Therefore, the average power is getting worse than in the low-speed case. The results of the power comparison will be shown in Table III at the end of this section. In the

conventional rectifier, the rate of increase of the average power goes down as the speed of the rotor increases because of the out-of-phase phenomenon. However, in the proposed control method, this out-of-phase phenomenon does not occur because of the in-phase current control by using the active switching. Therefore, the relevant power increase to conventional rectifier in the high-speed mode is much bigger than in low-speed mode.

$$\phi = \tan^{-1}\left(\frac{wL}{R}\right) \tag{4.46}$$

Where, ϕ is phase difference angle between EMF and current; w, L and R are angular speed, inductance and resistance of the system, respectively.

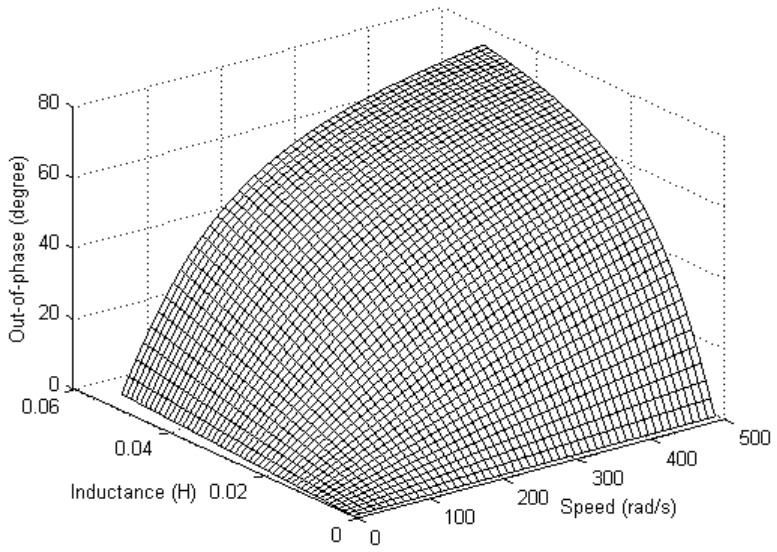

Fig. 31. Phase delay according to inductance and speed.

Figs. 32 through 36 show the simulation results with a active converter for an operating point at 1350 RPM and rated current 5A. The switching frequency is 20kHz.

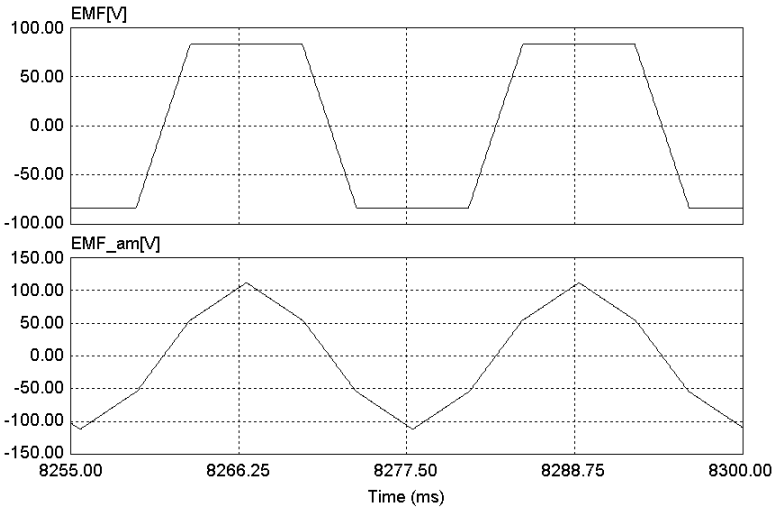

Fig. 32. Simulated phase EMF and zero-sequence eliminated-phase EMF.

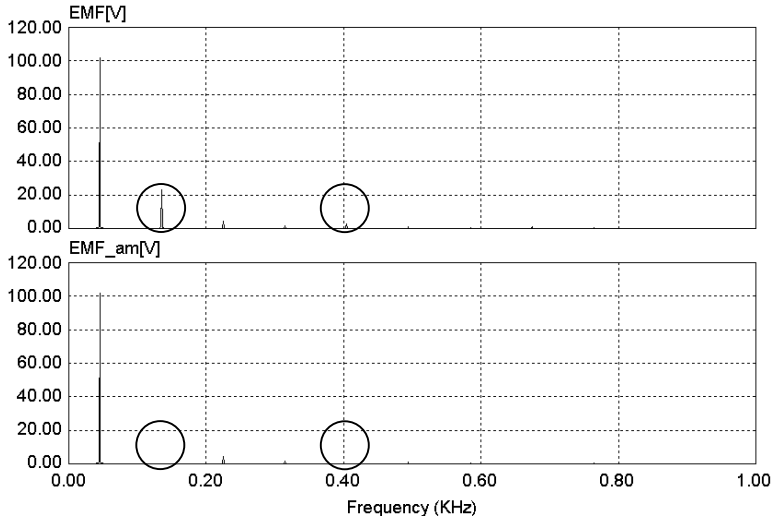

Fig. 33. Frequency analysis of phase EMF and zero-sequence eliminated-phase EMF.

Fig. 32 shows simulated phase EMF and zero-sequence eliminated-phase EMF. Since the EMF is proportional to the rotational speed, the magnitude of the calculated EMF and zero-sequence eliminated-phase EMF is increased compared with the 300 RPM case. But the shapes of those are identical. Fig. 33 shows the result of frequency analysis of the EMF and zero-sequence eliminated EMF to confirm the proposed algebraic method. The fundamental frequency is 45Hz. The circles show the third and ninth harmonic components. It is clear that using the proposed simple algebraic method without requiring a FFT has eliminated the zero-sequence component from the trapezoidal EMF regardless of the speed of the rotor.

Fig. 34 shows the three-phase zero-sequence eliminated EMFs at 1350 RPM. It is similar as a sinusoidal waveform but it has all harmonics except multiple of the third harmonic.

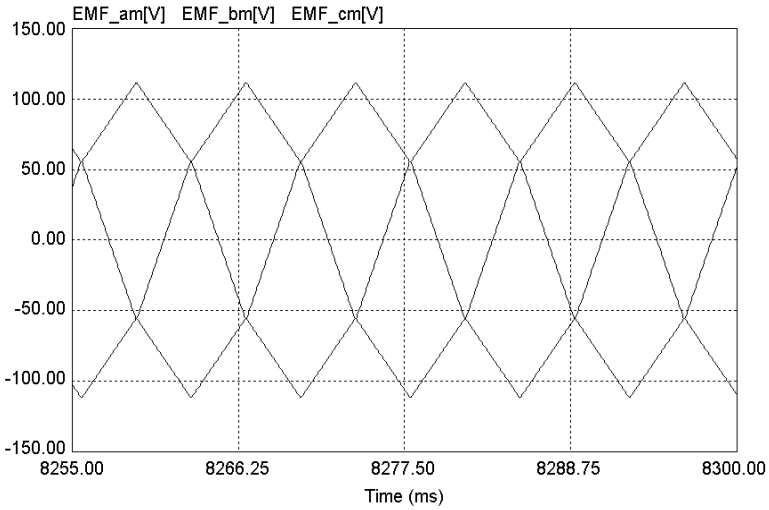

Fig. 34. Zero-sequence eliminated three-phase EMFs at 1350 RPM.

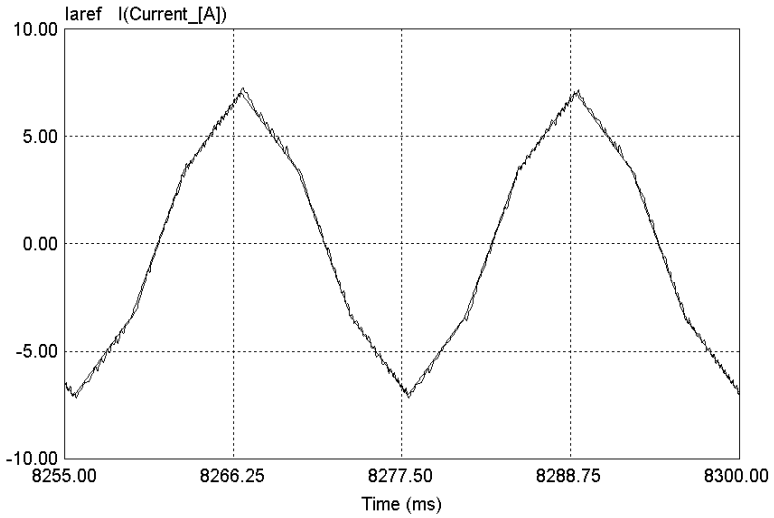

Fig. 35. Optimal current reference waveform and controlled current for power density maximization at 1350 RPM and rated current 5A.

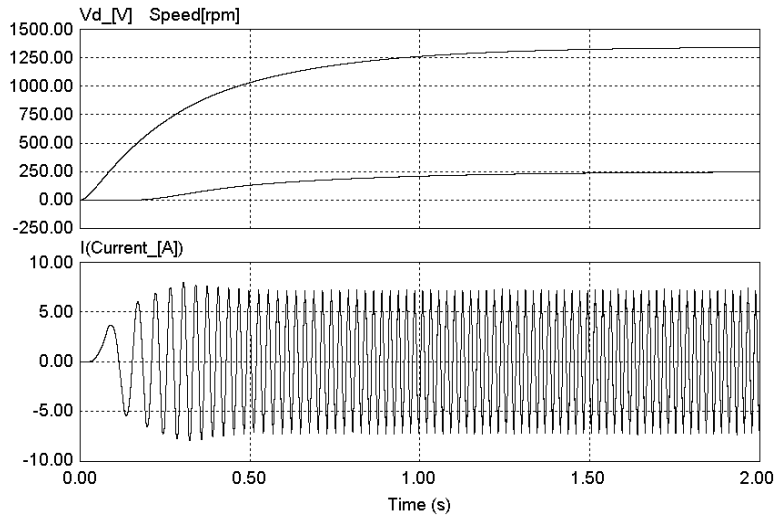

Fig. 36. Transient response with the PI voltage controller.

The optimal current reference waveform and controlled phase current are shown in Fig. 35. A hysteresis controller is used for current control and the band of the

controller is 0.05A, the same as the 300 RPM case. Since the magnitude of phase current for an operating point at 1350 RPM is almost 13 times larger than the 300 RPM case, the same control band as 300 RPM case, 0.05A is so small that the controlled current is almost the same as reference. The performance of the drive during transient period is also simulated. Fig. 36 shows the phase current and voltage response with the PI voltage controller. The output of the voltage controller is the magnitude of the current reference and the waveform of the current reference comes from (4.41).

Table III. Comparison of the electrical output power of the BLDC generator.

	Conventional Method	Proposed Method	Conventional Method	Proposed Method
Speed[RPM]	300	300	1350	1350
RMS Current[A]	0.386	0.386	5.0	5.0
Output Power[W]	18.32	19.80	251.1	464.5
Increase[%]	-	8.1	-	85

Table III shows the electrical output power comparison between a conventional method and the proposed method. Here, the most important thing for comparing the electrical output power is to keep the RMS (Root-Mean-Square) current values the same in both cases. In other words, the rating of the machine should be the same in both cases. In the same low speed (300 RPM) and same small RMS current (0.386A), the proposed method increases electrical output power by 8.1%. Also, in the same high speed (1350 RPM) and same rated RMS current (5.0A), the proposed method increases electrical output power by 85%. Since the conventional diode rectifier has a significant out-of-

phase phenomenon in the condition of high inductance and high speed, the increase of power in the high-speed case is much larger than low-speed case, even though the proposed control method is applied perfectly to both cases.

From the other point of view, the weight and volume of the generator can be reduced by 8.1% and 85%, respectively because the volume of the machine is proportional to the electrical output power. Hence, it is possible to make the whole power generation system compact and much more light by using the proposed control method.

H. Conclusion

In this chapter, first the theory of the proposed control method for power density maximization of the BLDC generator was presented. EMF calclulation based on the voltage equation and the optimal current waveform of both single-phase and three-phase non-sinusoidal power supply systems are investigated. And also, a simple algebraic method for zero-sequence elimination from EMFs was presented. The details of the simulation model developed to understand the performance of the BLDC generator system were described. Also, a comprehensive set of simulation results was presented and discussed. In the next chapter, the details of the experimental results carried out to validate the proposed control method will be presented.

CHAPTER V

EXPERIMENTAL VERIFICATION OF THE PROPOSED CONTROL METHOD FOR POWER DENSITY MAXIMIZATION

In Chapter IV, the theory of the proposed current control scheme for power density maximization and the simulation results of the method were presented. The next step is to experimentally validate the theory of the proposed method and the simulation results.

In this chapter, the details of the experimental setup designed and developed in the laboratory are described. Also, the procedure involved in developing the software for the control scheme is discussed. Finally, the experimental results obtained in the laboratory are presented.

A. Experimental Setup

The experimental test bed has been designed and developed in the Power Electronics and Motor Drive Laboratory, Electrical Engineering Department. The experimental setup consists of a 0.75kW, 5.0A, three-phase, four-pole BLDC generator drive connected with a permanent magnet DC motor as a prime mover, active converter and load. The load can be changed by varying the value of the resistor that is connected

to the DC-link capacitor. The IGBTs (Insulated Gate Bipolar Transistors) are used as converter switches, and freewheeling diodes integrated inside of the IGBTs can be used as a full bridge diode rectifier as well. Fig. 37 shows the block schematic of the developed experimental BLDC generator system.

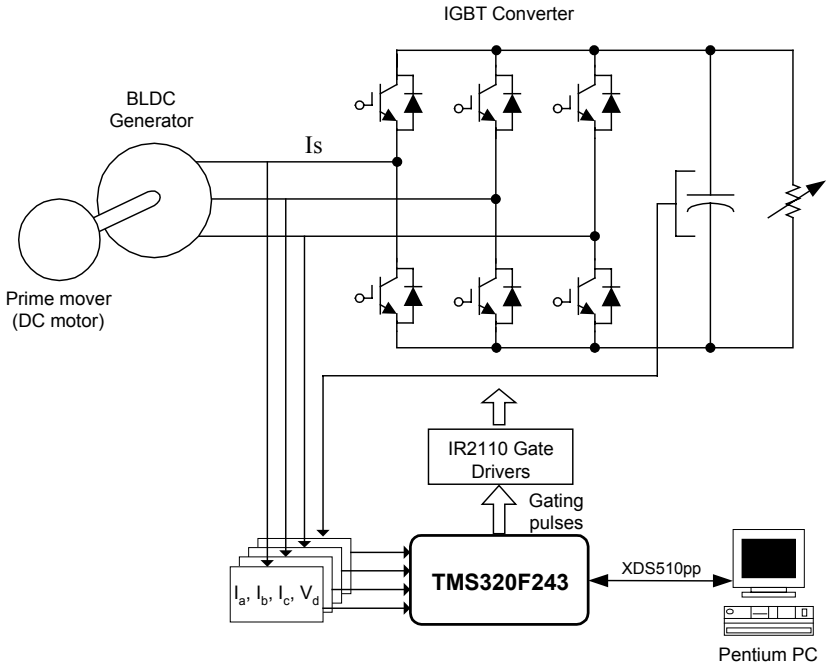

Fig. 37. Block schematic of the experimental system.

For current sensing, Hall-effect current sensors, which are manufactured by the LEM company (LA55-P) are used. Fig. 38 shows the current sensing circuit. For voltage sensing, a Hall-effect voltage sensor, which is also manufactured by the LEM (LV25-P) is used.

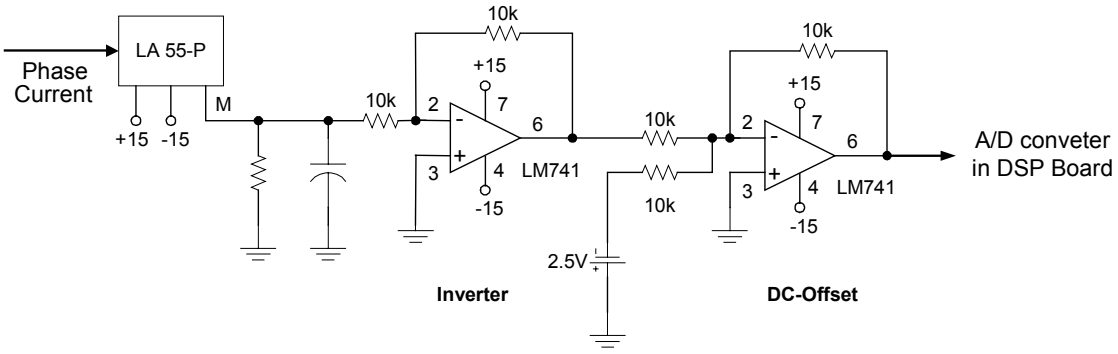

Fig. 38. Current sensing circuit.

The entire drive system is controlled by using the TMS320F243 Digital Signal Processor (DSP). The DSP has a high-speed 10-bit Analog-to-Digital (A/D) converter which has four independent channels. The specification of the DSP, TMS320F243 is described in Table IV.

Table IV. Specification of the TMS320F243 DSP.

MIPS	20MIPS (50ns)
Data Bus	16 bit
Internal Register	544 word
Internal ROM/EEPROM	8K word
Memory Size	224K word
Timer/Counter	2 up/down counter/timer
A/D Converter	8 channel, 10 bit (conversion time: 900ns)
PWM Channel	8 channel (synchronous/asynchronous)
Interrupt Source	34 interrupt sources
External Interrupt Pin	3 external interrupt pins

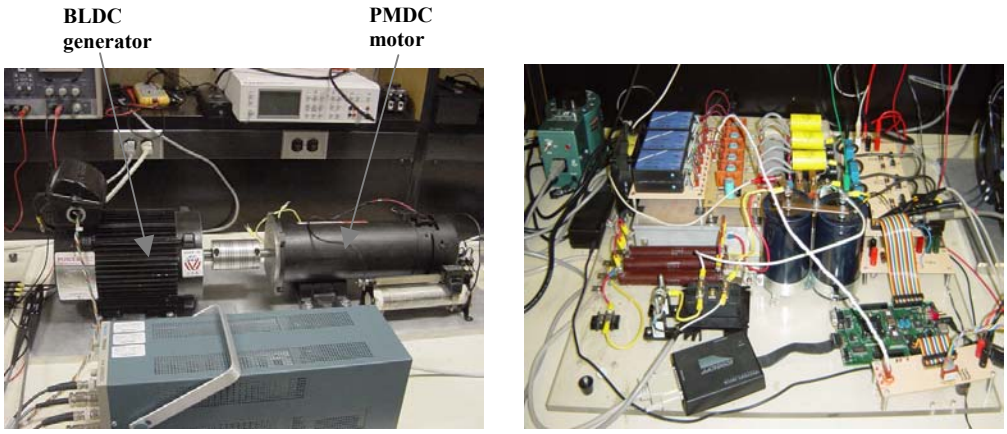

(a) BLDC generator and prime mover (b) Drive system

Fig. 39. Experimental test-bed.

Fig. 39 shows the overall experimental test-bed for the BLDC generator drive system built in the Power Electronics and Motor Drives Laboratory, Texas A&M University. A DC motor is used for the prime mover of the generating system, as shown in the right side of the Fig. 39(a). The converter and the controller are shown in Fig. 39(b). Specifications of the BLDC generator used to examine the performance of the developed technique are presented in Table V.

Table V. Specification of the BLDC generator.

Pole	4	Resistance	4.3[Ω]
Phase	3	Inductance	43[mH]
Power	0.75[kW]	K_e	1.29[V/rps]
DC–link Battery	7200[μF]	Rated Current	5.0[A]

B. Software Structure

The first step for development of the control algorithm is to initialize all the peripherals on the DSP board, which includes initialization of the PWM ports, timer interrupt, Analog-to-Digital (A/D) converters, and Digital-to-Analog (D/A) converters. The next step is to develop an EMF calculation algorithm. The controller should sense the active phase currents and DC-link voltage from the Hall-effect sensors, and then compute the line-to-line EMF, basically solving (4.33) in real-time. The programming of the DSP is done using the assembly language.

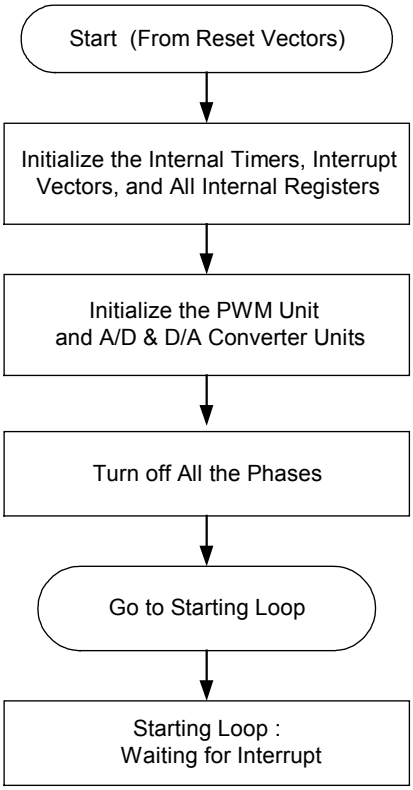

Fig. 40. Flowchart of the main program.

The flowchart of the main program is shown in Fig. 40. For the periodic sampling and computation, a timer interrupt function is utilized. In the timer interrupt service routine (ISR), an algorithm for control of optimal current waveform is programmed. Fig. 41 shows the flowchart of the control algorithm.

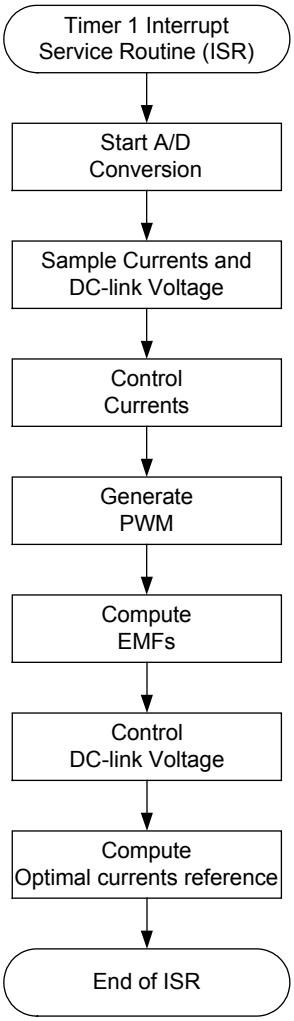

Fig. 41. Flowchart of the control algorithm.

Once the timer interrupt service routine starts, the controller measures the phase currents and DC-link voltage at periodic intervals. The timer 1 interrupt source in the DSP is used to generate periodic sampling every 50 μ seconds. During each interrupt, the active phase currents and DC-link voltage are sampled using the A/D converters. Once the instantaneous magnitude of the phase currents and DC-link voltage are stored, the EMFs and optimal current reference waveforms for power density maximization can be computed based on voltage equation and simple algebraic method described in Chapter IV. Output of the PI controller for DC-link voltage control will decide the magnitude of the phase current reference.

C. Experimental Results

In this experiment, the PI controller is used for DC-link voltage control and hysteresis controller is used for each phase current control. The EMFs are calculated based on the sensed DC-link voltage, sensed phase currents, and the switching status of the converter. Fig. 42 shows the three-phase induced EMF waveforms of the test-bed BLDC generator by direct measurement. Each phase is shifted by a 120^{o} electrical angle and the waveform is not exactly trapezoidal as in simulation because of the machine geometry, the winding of the stator, and the unevenness of the surface of the permanent magnet in the rotor. Fig. 43 shows the experimental waveforms of each phase current waveform with a diode rectifier at 300 RPM. The RMS value of the current is 0.386A.

Since the speed of rotor is low and magnitude of the current is small, current waveform shows the typical diode rectifier current waveform.

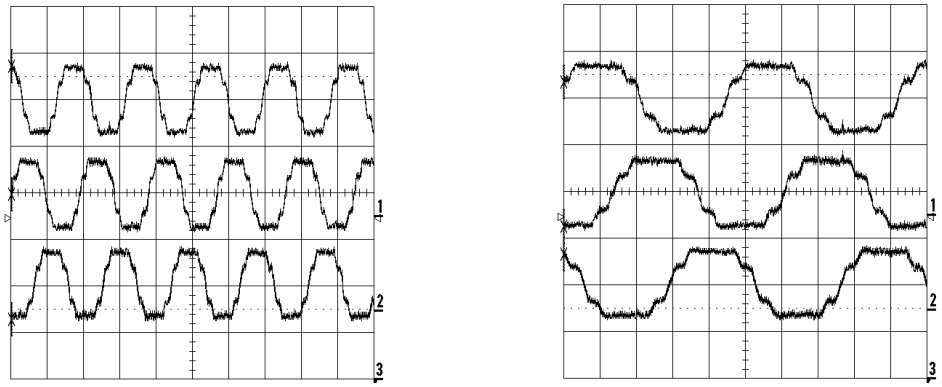

(a) 50 ms/div. (b) 20 ms/div.

Fig. 42. Phase EMF waveforms of the test-bed from the direct measurement [25 V/div.].

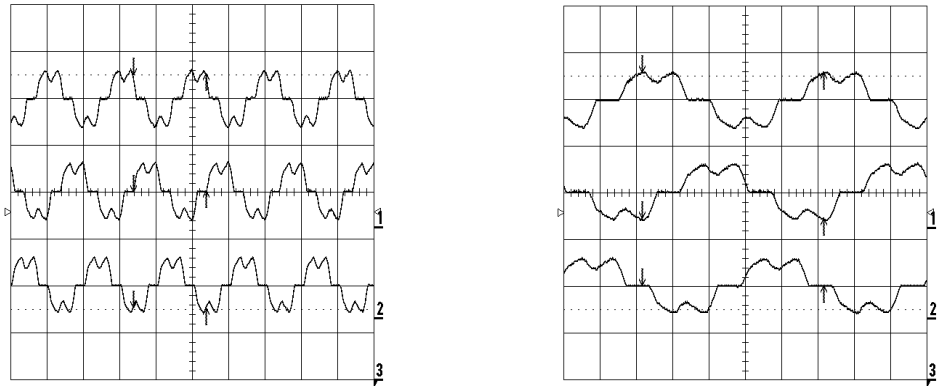

(a) 50 ms/div. (b) 20 ms/div.

Fig. 43. Each phase current waveform with a diode rectifier at 300 RPM [1 A/div.].

Fig. 44 shows the calculated line-to-line EMF waveforms at 300 RPM. The line-to-line EMF is computed in the DSP by solving the voltage equation, (4.33) and is sent

to a D/A converter to observe through an oscilloscope. Based on the calculated line-to-line EMFs, the zero-sequence component of the EMFs are eliminated by using (4.41); the results are shown in Fig. 45. These zero-sequence eliminated EMFs form the ground of the optimal current reference waveform for power density maximization. And these are similar to sinusoidal waveforms.

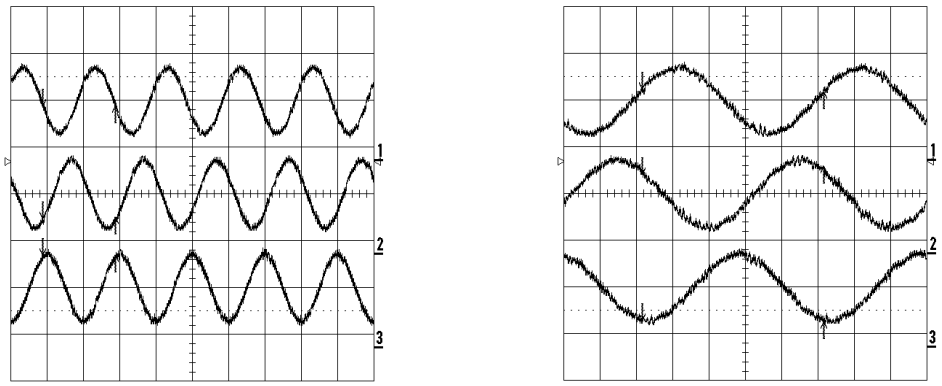

(a) 50 ms/div. (b) 20 ms/div.

Fig. 44. Calculated line-to-line EMF waveforms at 300 RPM [50 V/div.].

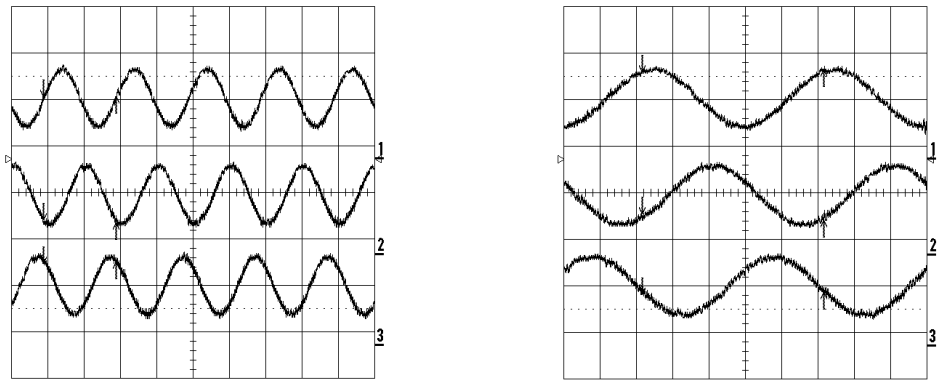

(a) 50 ms/div. (b) 20 ms/div.

Fig. 45. Zero-sequence eliminated phase EMF waveforms at 300 RPM [50 V/div.].

Fig. 46 shows the line-to-line EMF of phase BC, the zero-sequence eliminated EMF of phase A, and the controlled current of phase A at 300 RPM. As it is shown, zero-crossing point of the line-to-line EMF is the peak point of the phase current. In other words, calculated-phase EMF and current are in-phase.

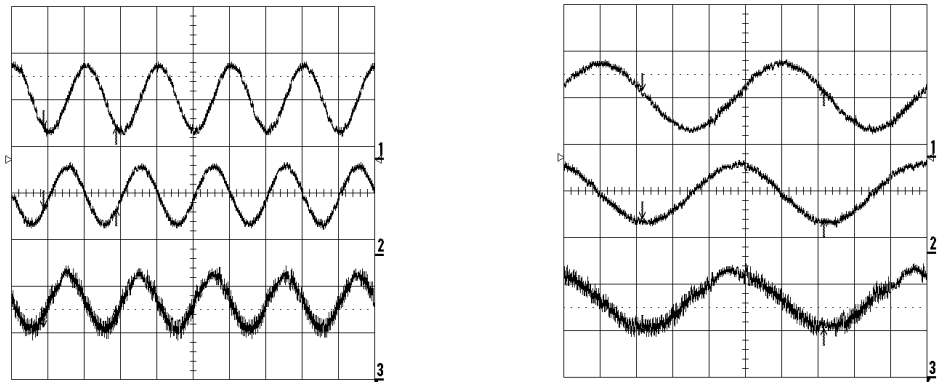

(a) 50 ms/div. (b) 20 ms/div.

Fig. 46. Line-to-line EMF_{bc}, zero-sequence eliminated phase EMF_a, and controlled phase current I_a waveforms at 300 RPM [50 V/div., 50 V/div., 1 A/div.].

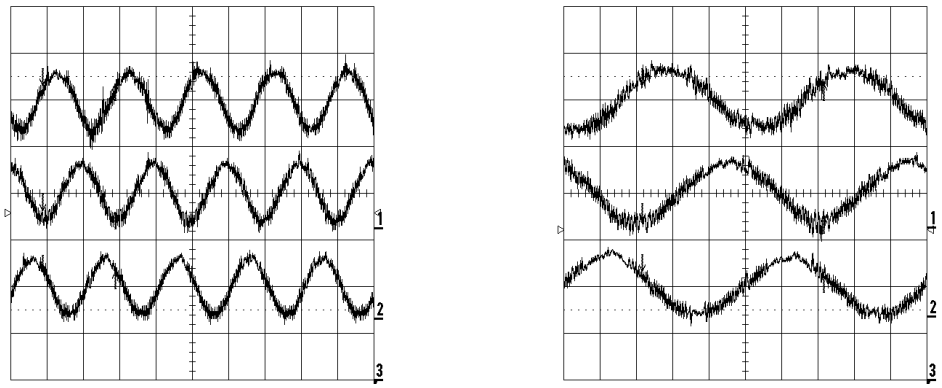

(a) 50 ms/div. (b) 20 ms/div.

Fig. 47. Each phase current waveforms at 300 RPM [1 A/div.].

In Fig. 47, three-phase controlled current waveforms are presented and the hysteresis controller for the current shaping is working well. Fig. 48 shows the phase EMF from the direct measurement and optimal current reference waveforms of the test-bed BLDC generator based on the proposed control method.

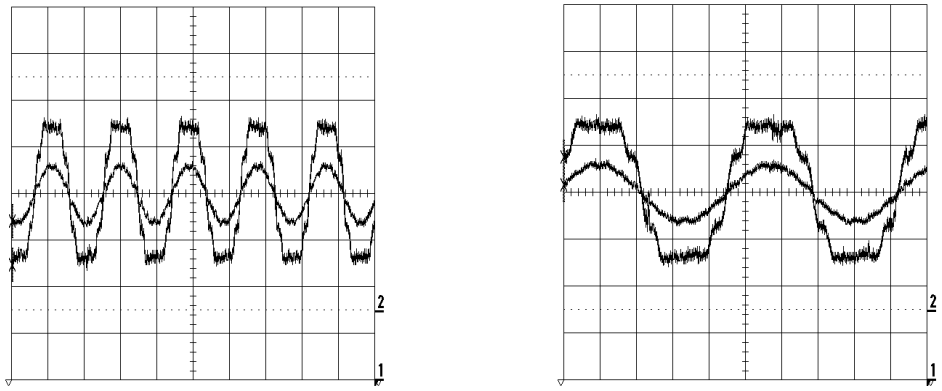

(a) 50 ms/div. (b) 20 ms/div.

Fig. 48. Phase EMF and optimal current reference waveforms of the test-bed BLDC generator from direct measurement [15 V/div., 1A/div.].

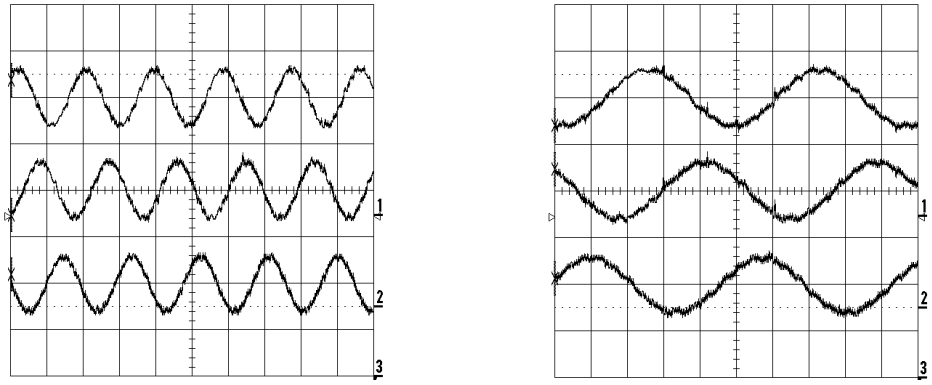

(a) 50 ms/div. (b) 20 ms/div.

Fig. 49. Each phase optimal current reference waveform of the test-bed BLDC generator from the EMFs measured directly [1A/div.].

Current reference is not as smooth as its simulation results because the EMF of the test-bed generator is not the same as the ideal trapezoidal waveform. However, this is the optimal current reference waveform for the power density maximization in the test-bed BLDC generator. Each phase optimal current reference waveform of the test-bed BLDC generator based on the directly measured EMFs is presented in Fig. 49.

In Fig. 50(a), each phase optimal current reference waveform of the test-bed BLDC generator by using the directly measured EMFs. And each phase optimal current reference waveform by using the calculated EMFs is shown in the Fig. 50(b). As shown, the current reference from the calculated EMFs is almost identical with the current reference from the directly measured EMFs.

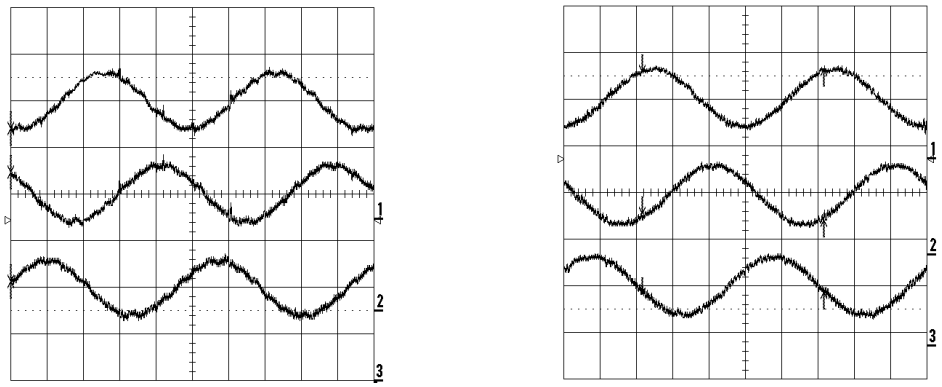

(a) From the direct EMF information (b) From the calculated EMF information

Fig. 50. Each phase optimal current reference waveform of the test-bed BLDC generator [1A/div.] [20ms/div.].

Fig. 51 shows the experimental waveforms of the phase current with a diode rectifier at 1350 RPM. The RMS value of the current is the same as the rated current at

5.0A. The phase current is almost a sinusoidal waveform, and it is out of phase with phase EMF because the speed of the rotor is high and the magnitude of the current is large compared with the low-speed case, while inductance of the generator is large. As discussed in Chapter IV, out-of-phase phenomenon between induced voltage and current is prominent in (4.46) and Fig. 31 as the inductance of the generator and speed of the rotor increase. Therefore, the rate of increase of the average power gets worse compared with the low-speed case. The results of the power comparison will be shown in Table V at the end of this section.

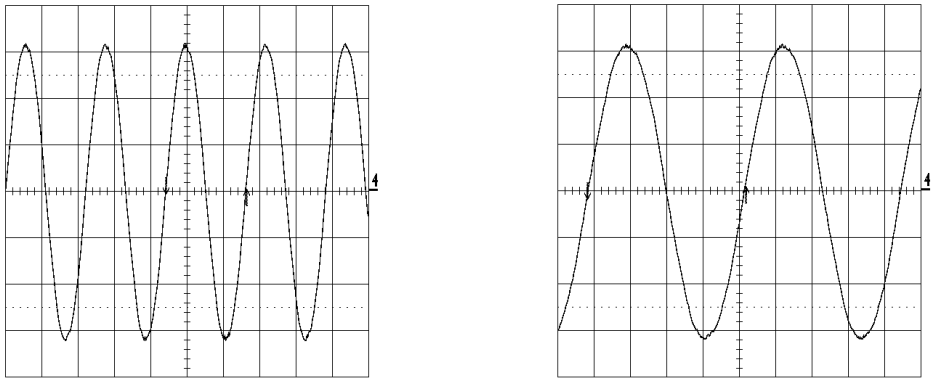

(a) 10 ms/div. (b) 5 ms/div.

Fig. 51. Phase current waveform with a diode rectifier at 1350 RPM [2 A/div.].

Fig. 52 shows the calculated line-to-line EMF and zero-sequence eliminated EMF waveforms at 1350 RPM. The results are not clean and good waveforms since the EMFs are calculated based on the sensed DC-link voltage, sensed phase currents, and the switching status of the converter. In the high-speed operation, measurement error of currents and DC-link voltage, and the influences of the parameter deviations cause the

accuracy problem. In addition, controlling three phases all together at the same time increases the length of the algorithm and decreases sampling frequency. If more accurate current-measurement devices and high speed DSP with higher MIPS and higher data bits A/D converters are used, the calculation of the EMFs can be more precise.

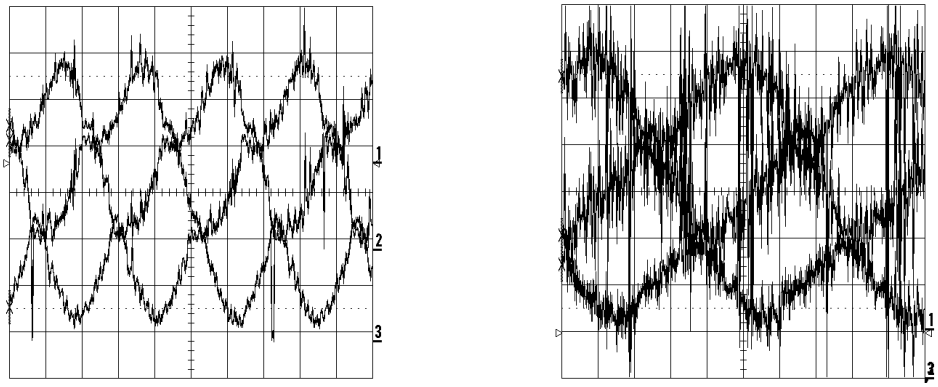

(a) [10 ms/div., 180V/div.] (b) [5 ms/div., 120V/div.]

Fig. 52. Calculated line-to-line EMF and zero-sequence eliminated EMF waveforms at 1350 RPM.

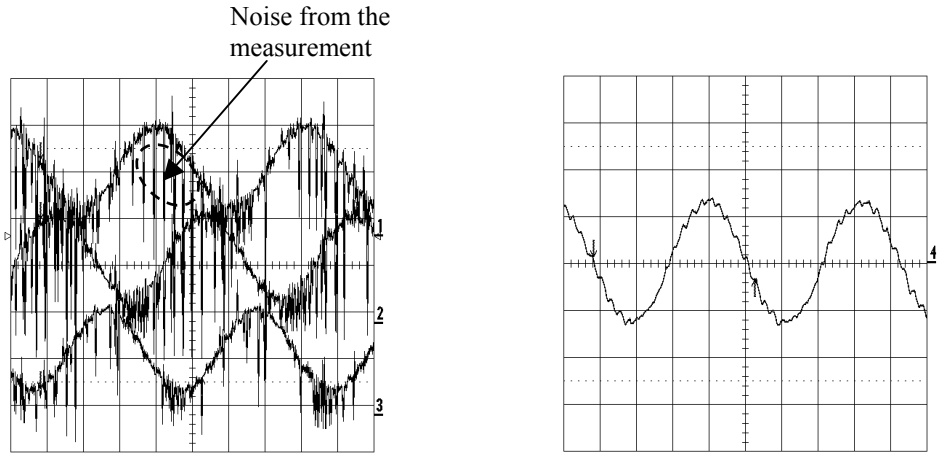

(a) Three phases [5 ms/div., 7 A/div.] (b) One phase [5 ms/div., 5 A/div.]

Fig. 53. Each phase current waveform at 1350 RPM.

Fig. 53 shows each phase controlled current waveform at 1350 RPM. There is some measurement noise in Fig. 53(a), but Fig. 53(b) shows the clean one phase current waveform which is measured directly by current probe amplifier. Hence, we can see that the noise in Fig. 53(a) is not a real value of the phase current. For more study, error analysis including measurement error is performed at section G in the following Chapter VI. For the current shaping, hysteresis control is used.

Table VI shows the electrical output power comparison between a conventional method and the proposed method. Here, the most important thing for comparing the electrical output power is to keep the RMS current values the same in both cases. In other words, the rating of the machine should be the same in both cases. In the same speed (300 RPM, 1350 RPM) and the same RMS rated current (0.386A, 5.0A), the proposed method increases electrical output power by 6.9% and 43%, respectively. That is, the weight and volume of the generator can be reduced by 6.9% and 43%, respectively because volume of the machine is proportional to the electrical output power.

As shown in Table VI, there is a difference of power increase between the low-speed case and the high-speed case, even though the proposed method is same in both cases. In the low-speed mode, since the induced voltage and phase current is almost in-phase, the output power using a conventional method loses only 6.9%. However, in the high-speed mode, the phase current is almost a sinusoidal waveform, and it is considerably out of phase with phase EMF because the speed of rotor is high, inductance of the generator is large, and magnitude of the current is big. As discussed in chapter IV,

out-of-phase phenomenon between induced voltage and current with a diode rectifier makes the average power get worse than the low-speed mode. Therefore, increase of the output power by using the proposed control method in the high-speed case is relatively much larger than in the low-speed case.

And also, simulation results (Table III in Chapter IV) show a higher increase of power density than experimental results because the induced voltage and current is perfectly in-phase in simulation but the induced voltage and current cannot be perfectly in-phase in the experiment because of the time-delay from the EMF calculation and filtering operation.

Table VI. Comparison of the electrical output power of the BLDC generator.

	Conventional Method	Proposed Method	Conventional Method	Proposed Method
Speed[RPM]	300	300	1350	1350
RMS Current[A]	0.386	0.386	5.0	5.0
Output Power[W]	19.56	20.91	242.3	346.8
Increase[%]	-	6.9	-	43

D. Conclusion

In this chapter, the hardware details of the experimental setup developed in the laboratory and the software algorithm for the proposed control method for power density

maximization were explained. The control algorithm, in the form of flowcharts, was presented. With the experimental test-bed developed in the laboratory, a comprehensive set of experimental results was also presented. From the results, it is verified that the proposed control method works over a wide speed range, from low-speed to high-speed.

In the next chapter, the analyses of various attributes of the proposed control method will be performed to investigate the effects of various situations.

CHAPTER VI

ANALYSIS OF VARIOUS ATTRIBUTES OF THE PROPOSED CONTROL METHOD

The simulation and experimental results are presented in the previous chapter to show the validity of the proposed method. In order to ensure high performance operation of the proposed BLDC generator drive, various attributes of the proposed control method are analyzed and shown in this chapter. The influences from several situations (neutral point connection, sinusoidal current waveform, load variation, one-phase failure, unbalanced induced EMF, and multi-phase) on the performance of the proposed control technique are investigated through simulation and experiments. Also, the various sources of the EMF estimation errors are investigated as well.

A. Power Density Maximization in Case Neutral Point is Connected

Since many manufacturers do not provide the neutral point in the BLDC machine, the proposed control method in this research presents the general case without neutral point connection as shown in Fig. 8 on page 17.

As stated in Chapter IV, the product of each voltage and current harmonic produces electrical output power. So we had to consider all harmonics included. However, for power density maximization in the three-phase BLDC generator, the

proposed optimal current waveform does not take care of zero-sequence component, multiple of the third harmonic because this term does not exist in the general case that is without neutral point connection and does not contribute to the total power in the three-phase system. In other words, the sum of the three phase currents should be zero in the Wye connection according to the Kirchhoff's law, in (4.18).

$$
\begin{aligned}
e_a(t) &= E_{a1}\sin(wt) + E_{a2}\sin 2(wt) + E_{a3}\sin 3(wt) + E_{a4}\sin 4(wt) + \dots \\
e_b(t) &= E_{b1}\sin(wt - \frac{2\pi}{3}) + E_{b2}\sin 2(wt - \frac{2\pi}{3}) + E_{b3}\sin 3(wt - \frac{2\pi}{3}) + E_{a4}\sin 4(wt - \frac{2\pi}{3}) + \dots \\
e_c(t) &= E_{c1}\sin(wt - \frac{4\pi}{3}) + E_{c2}\sin 2(wt - \frac{4\pi}{3}) + E_{c3}\sin 3(wt - \frac{4\pi}{3}) + E_{a4}\sin 4(wt - \frac{4\pi}{3}) + \dots \\
i_a(t) &= I_{a1}\sin(wt - \phi_1) + I_{a2}\sin 2(wt - \phi_2) + I_{a4}\sin 4(wt - \phi_4) + \dots \\
i_b(t) &= I_{b1}\sin(wt - \phi_1 - \frac{2\pi}{3}) + I_{b2}\sin 2(wt - \phi_2 - \frac{2\pi}{3}) + I_{b4}\sin 4(wt - \phi_4 - \frac{2\pi}{3}) + \dots \\
i_c(t) &= I_{c1}\sin(wt - \phi_1 - \frac{4\pi}{3}) + I_{c2}\sin 2(wt - \phi_2 - \frac{4\pi}{3}) + I_{c4}\sin 4(wt - \phi_4 - \frac{4\pi}{3}) + \dots
\end{aligned}
\tag{4.18}
$$

However, if the neutral point is connected in the three-phase system, the sum of the three phase currents does not need to be zero any longer because there is a path for current flowing in the system, as shown in Fig. 54. Consequently, we are able to take care of all the harmonics included in the induced EMF so that we can have more electrical output power from the generator because the zero-sequence component can contribute to the total electrical output power in this case, as in (6.1).

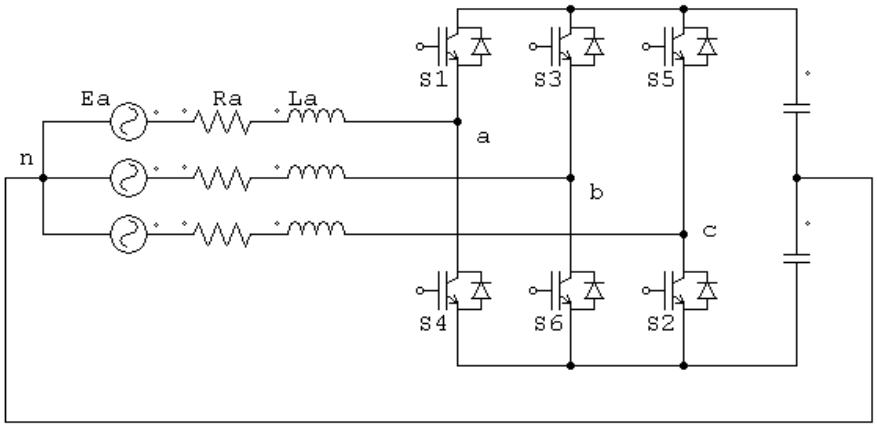

Fig. 54. Equivalent circuit of the BLDC generator with neutral connection.

$$
\begin{aligned}
e_a(t) &= E_{a1}\sin(wt) + E_{a2}\sin 2(wt) + E_{a3}\sin 3(wt) + E_{a4}\sin 4(wt) + \dots \\
e_b(t) &= E_{b1}\sin(wt - \frac{2\pi}{3}) + E_{b2}\sin 2(wt - \frac{2\pi}{3}) + E_{b3}\sin 3(wt - \frac{2\pi}{3}) + E_{a4}\sin 4(wt - \frac{2\pi}{3}) + \dots \\
e_c(t) &= E_{c1}\sin(wt - \frac{4\pi}{3}) + E_{c2}\sin 2(wt - \frac{4\pi}{3}) + E_{c3}\sin 3(wt - \frac{4\pi}{3}) + E_{a4}\sin 4(wt - \frac{4\pi}{3}) + \dots \\
\\
i_a(t) &= I_{a1}\sin(wt - \phi_1) + I_{a2}\sin 2(wt - \phi_2) + I_{a3}\sin 3(wt - \phi_3) + I_{a4}\sin 4(wt - \phi_4) + \dots \\
i_b(t) &= I_{b1}\sin(wt - \phi_1 - \frac{2\pi}{3}) + I_{b2}\sin 2(wt - \phi_2 - \frac{2\pi}{3}) + I_{b3}\sin 3(wt - \phi_3 - \frac{2\pi}{3}) \\
&\quad + I_{b4}\sin 4(wt - \phi_4 - \frac{2\pi}{3}) + \dots \\
i_c(t) &= I_{c1}\sin(wt - \phi_1 - \frac{4\pi}{3}) + I_{c2}\sin 2(wt - \phi_2 - \frac{4\pi}{3}) + I_{c3}\sin 3(wt - \phi_3 - \frac{4\pi}{3}) \\
&\quad + I_{c4}\sin 4(wt - \phi_4 - \frac{4\pi}{3}) + \dots
\end{aligned}
\tag{6.1}
$$

Fig. 54 shows the equivalent circuit of the BLDC generator with a neutral point connection. Two of batteries instead of one should be used for connection with a neutral point. In order to implement to the Digital Signal Processor (DSP), a digitized form of the voltage equation for induced EMF calculation, in case of a neutral point connection, is presented as in (6.2):

$$\mathrm{E[k]} = R \cdot \left(\frac{i[k] + i[k-1]}{2} \right) + L \cdot \left(\frac{i[k] - i[k-1]}{t[k] - t[k-1]} \right) + V_{dclink} \cdot \left(\frac{2 * S_1[k-1] - 1}{2} \right) \quad (6.2)$$

Here, phase current is measured by a Hall-effect current sensor and R, L are known parameters. DC-link voltage is also measured by a Hall-effect voltage sensor and $S_1[k-1]$ is a switching function which is known by the current control algorithm. The $S_1[k-1]$ is actually PWM duty ratios in between zero and one.

Figs. 55 through 57 show the simulation results for an operating point at 1350 RPM. The induced EMF is assumed as an ideal trapezoidal waveform, as shown. As mentioned before, the optimal current reference waveform for maximizing power density with the neutral point connection does have all harmonics of induced phase EMF, including multiple of the third harmonics, zero-sequence component.

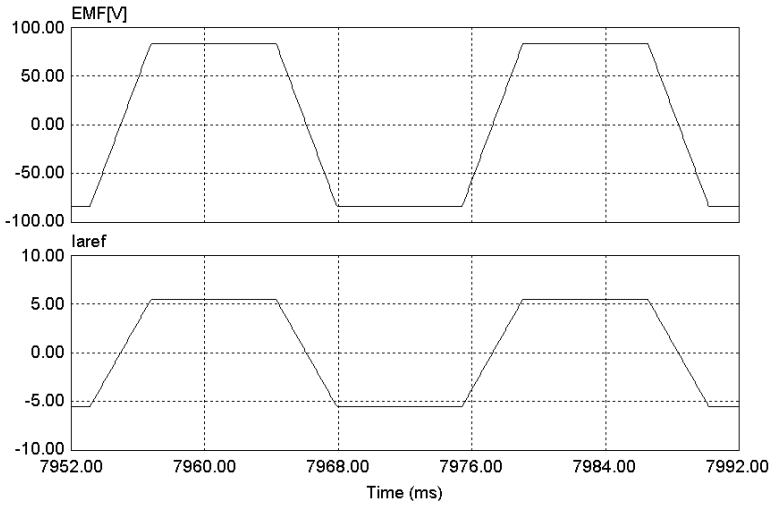

Fig. 55. Simulated phase EMF and the optimal current reference waveform.

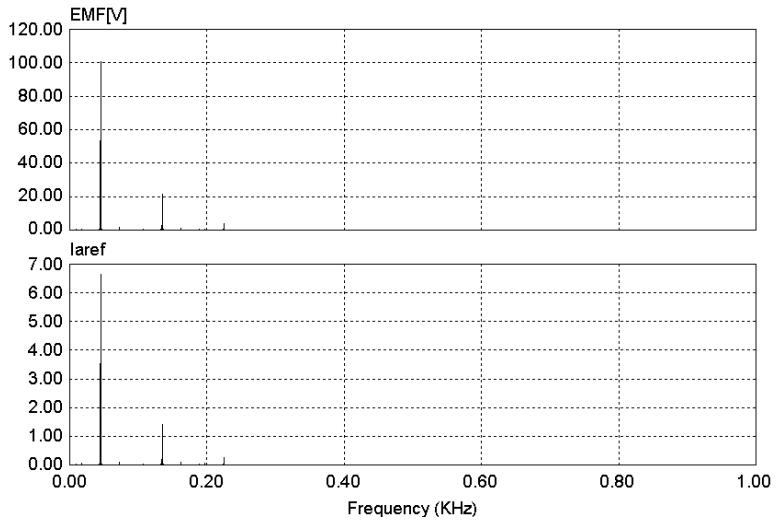

Fig. 56. Frequency analysis of phase EMF and current reference waveform.

Fig. 56 shows the result of frequency analysis of the phase EMF and optimal current reference waveform. Both of them have the same harmonic components such as fundamental, 3rd, 5th, 7th, etc. The fundamental frequency is 45Hz.

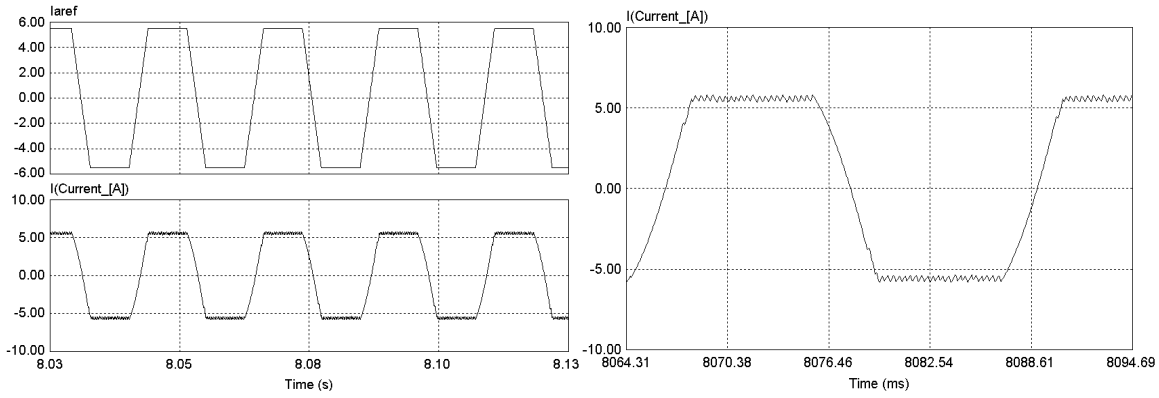

(a) Zoom out (b) Zoom in

Fig. 57. Optimal current reference waveform and a controlled current at 1350 RPM in case a neutral point is connected.

Fig. 57 shows the optimal current reference waveform and a controlled phase current in case neutral point is connected. The speed of the rotor is 1350 RPM and RMS current is 5.0A. A hysteresis controller is used for current control and the band of the controller (upper limit or lower limit from the reference in Fig. 18, (a)) is 0.05A. The switching frequency of the simulation is 20kHz. Since the inductance of the system is large, the controlled current sags little bit as shown in Fig. 57(b).

Fig. 58 and Fig. 59 show the experimental results of the neutral point connection. As shown in Fig. 58, the current is a trapezoidal waveform like phase EMF, and is controlled well by the hysteresis controller at 300 RPM. However, in the high-speed case, 1350 RPM, the current waveform is not trapezoidal like phase EMF, as shown in Fig. 59. The current waveform is not trapezoidal as we expected because of hardware limits as following:

- Currents and voltage measurement error
- A/D conversion error
- Low DSP speed (MIPS: Mega Instruction Per Second)

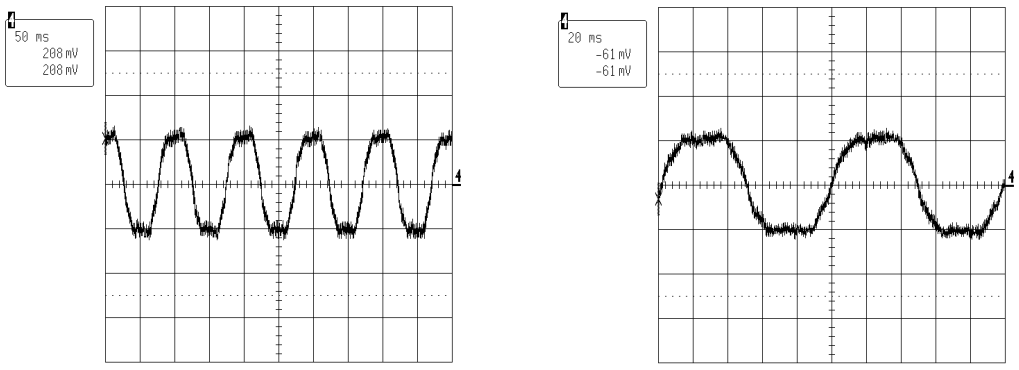

(a) 50 ms/div. (b) 20 ms/div.

Fig. 58. Phase current waveform at 300 RPM [1 A/div.].

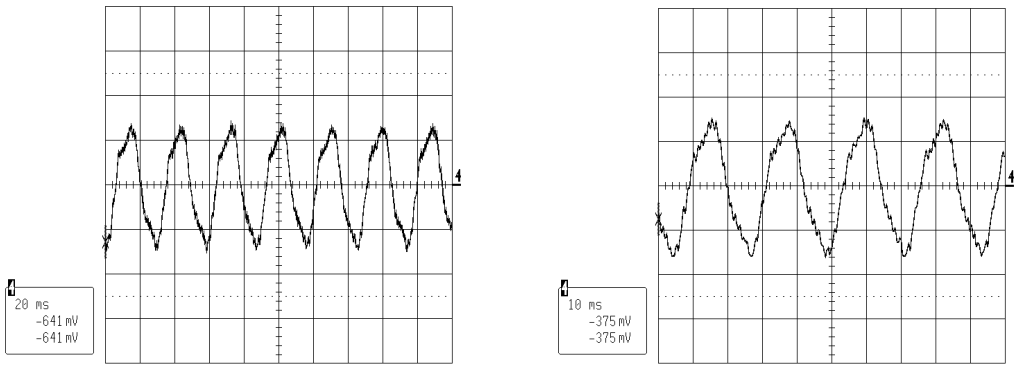

(a) 20 ms/div. (b) 10 ms/div.

Fig. 59. Phase current waveform at 1350 RPM [5 A/div.].

The EMFs are calculated based on the sensed DC-link voltage, the sensed phase currents, and the switching status of the converter as in (6.2). In the high-speed operation, currents measurement error, DC-link voltage measurement error and the influences of the parameter deviations cause the accuracy problem. And also, the A/D conversion makes the quantization error in the program. In addition, controlling three phases all together at the same time increases the length of the software algorithm and decreases switching frequency. Therefore, the calculated EMF in the high-speed is not exactly a trapezoidal waveform and the current reference is also not the trapezoidal waveform we expected. These are hardware limit problems.

In the experimental results of the proposed control method in Chapter V, even though the calculated EMFs are not exactly trapezoidal waveform in the high-speed operation because of hardware limits, the correct optimal current reference waveform is obtained in the process of eliminating zero-sequence component because it is similar as sinusoidal.

If more accurate measurement devices and high-speed DSP with higher MIPS and higher data bits A/D converters are used, the calculation of the EMFs will be more precise and the controlled current can be a more precise trapezoidal waveform. The detailed error analysis of the experimental results will be provided in the following section G.

Table VII. Comparison of the electrical output power with neutral point connection.

Speed : 1350 RPM		RMS Current : 5.0A	
	Control Method	Output Power [W]	Increase [%]
Simulation	Diode Rectifier	251.1[W]	
	Proposed Control	464.5[W]	85[%]
	Neutral Connection	475.1[W]	89[%]
Experiment	Diode Rectifier	242.3[W]	
	Proposed Control	346.8[W]	43[%]
	Neutral Connection	407.0[W]	68[%]

Table VII shows the comparison of the electrical output power of the BLDC generator when the neutral point connection is provided. In the condition of 1350 RPM and 5.0A, three methods: conventional method, proposed control method without a neutral point connection, control method with a neutral point connection, are compared. As shown in table VII, a neutral point connection mode has more power than the other control method; and the increase of output power is 89% in the simulation and 68% in the experiment, respectively.

Simulation results show higher increase of power density than experimental results because the induced voltage and current is perfectly in-phase in simulation, but the induced voltage and current cannot be perfectly in-phase in experiment because of the time-delay from the EMF calculation and filtering operation.

And also in the simulation, the increases of proposed control without a neutral point connection and with a neutral point connection are almost the same (85% and 89%) even though the zero-sequence component (which is used in case of a neutral point connection) is around 20% of the fundamental harmonic. The reason for this is because the current reference, in case the neutral point is connected, has a sharp slope as shown in Fig. 57, so that the current cannot follow the reference well compared with the proposed control which has not a neutral point connection.

However, in the experiment, both of the current control modes cannot follow the reference perfectly, regardless of sharp slope, because of the low switching frequency. Therefore, the magnitude of the zero-sequence component is dominant, and the increase of the control with a neutral point connection is bigger than the proposed control without a neutral point connection, as we expected.

From the study, we gather that if manufacturers provide the neutral point in the BLDC generator, we can have maximum output power possible with the proposed control method.

B. Sub-optimal Current Waveform for Practical Applications

The optimal current waveform for power density maximization of the non-sinusoidal system (because a BLDC generator has a trapezoidal EMF waveform) has been derived, incorporated in the system, and verified by numerical simulation and experiment in the previous chapters. As presented in Fig. 27, the optimal current waveform of the non-sinusoidal system is similar to a sinusoidal waveform but, the current contains all the harmonics of the phase EMF except multiple of the third harmonic that is the zero-sequence component.

However, these harmonics (5^{th}, 7^{th}, 11^{th}, etc.) are such small amounts in general (less than 5% of the fundamental) that we may sacrifice these terms and apply pure sinusoidal waveform for the current reference in practical applications, even though a BLDC generator is a non-sinusoidal system. Therefore, we can simplify the algorithm and its control, consequently since the sinusoidal current reference is well known and easy to implement.

In addition, as the inductance of the generator and speed of the rotor increase, the out-of-phase phenomenon between induced voltage and current is prominent, as shown in Fig. 31 on page 54. Therefore, a pure sinusoidal current reference that is the sub-optimal current reference, and its in-phase control is more important in practical than to match all harmonics included. However, note that this pure sinusoidal current waveform is not the optimal current waveform for power density maximization but a sub-optimal current waveform, theoretically.

Figs. 60 through 62 show the simulation results for an operating point at 1350 RPM. Even though the induced EMF waveform is not exactly trapezoidal because of the machine geometry, winding, and unevenness of the surface of the permanent magnet, the induced EMF is assumed as an ideal trapezoidal waveform as shown in Fig. 60.

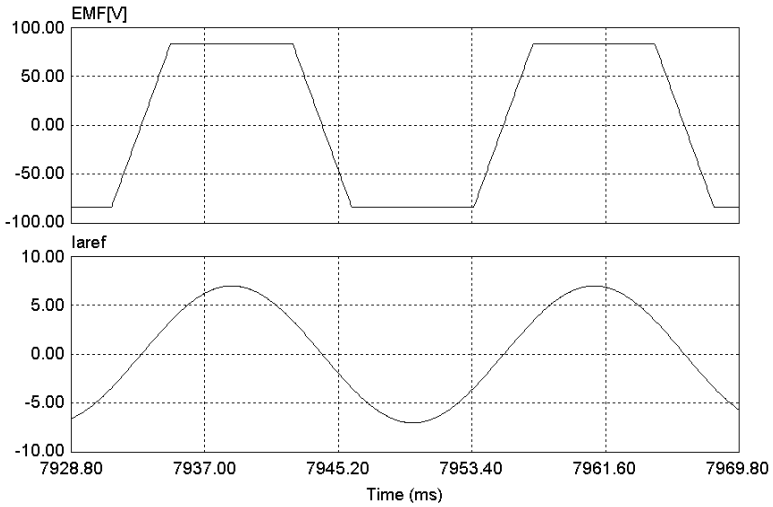

Fig. 60. Simulated phase EMF and sub-optimal current reference waveform.

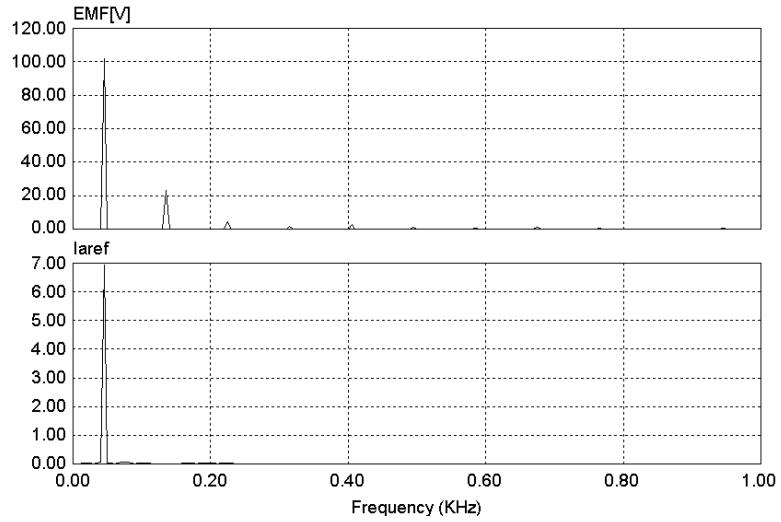

Fig. 61. Frequency analysis of phase EMF and current reference.

As it is mentioned before, the sub-optimal current reference waveform for maximizing power density in the non-sinusoidal power supply system, BLDC generator is shown in Fig. 60 and the result of frequency analysis of the induced phase EMF and sub-optimal current reference is shown in Fig. 61. The fundamental frequency is 45Hz and current reference waveform is pure sinusoidal.

Fig. 62 shows the sub-optimal current reference waveform, the pure sinusoidal waveform and a controlled phase current. The speed of the rotor is 1350 RPM and the RMS current is 5A. A hysteresis controller is used for current control and the band of the hysteresis controller is 0.05A. The fundamental frequency is 45Hz and the switching frequency of the simulation is 20kHz.

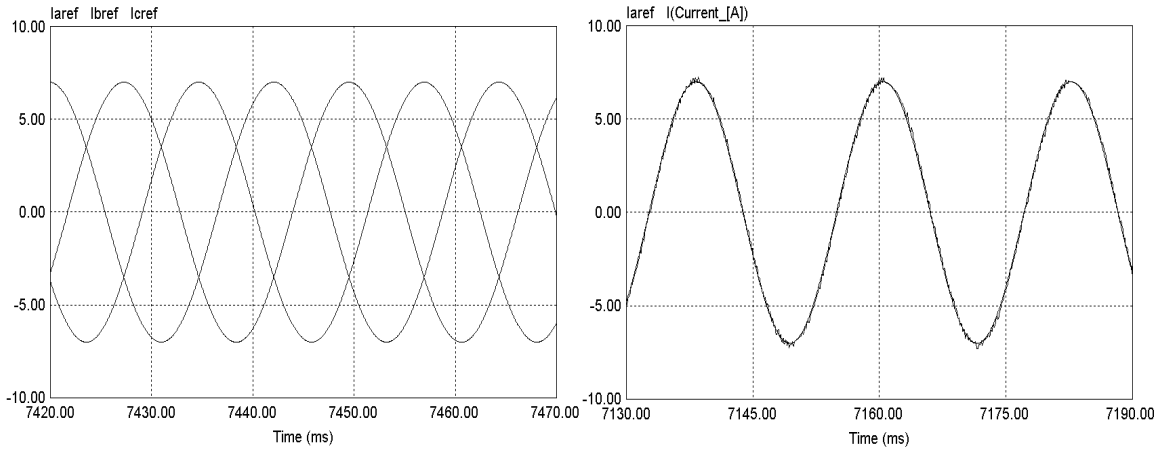

(a) Three phase current reference (b) Phase current reference and current

Fig. 62. Sub-optimal current reference waveform and controlled current for power density maximization at 1350 RPM.

Figs. 63 through 66 show the experimental results of the sinusoidal current reference waveform. Current reference waveform is generated by using the look-up-table, and the calculated EMF is used for detecting the zero-crossing point.

Figs. 64 and 65 show each phase current reference waveform at 300 RPM and 1350 RPM, respectively.

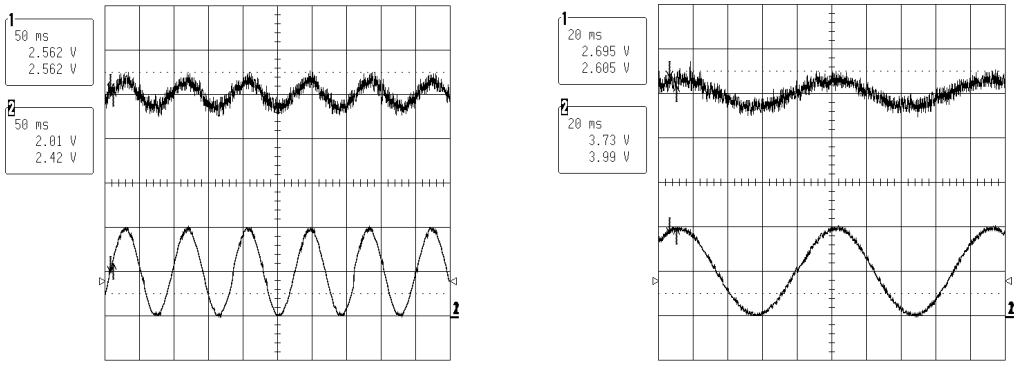

(a) 50 ms/div. (b) 20 ms/div.

Fig. 63. Zero-sequence eliminated EMF and phase current reference waveform at 300 RPM [50 V/div., 1A/div.].

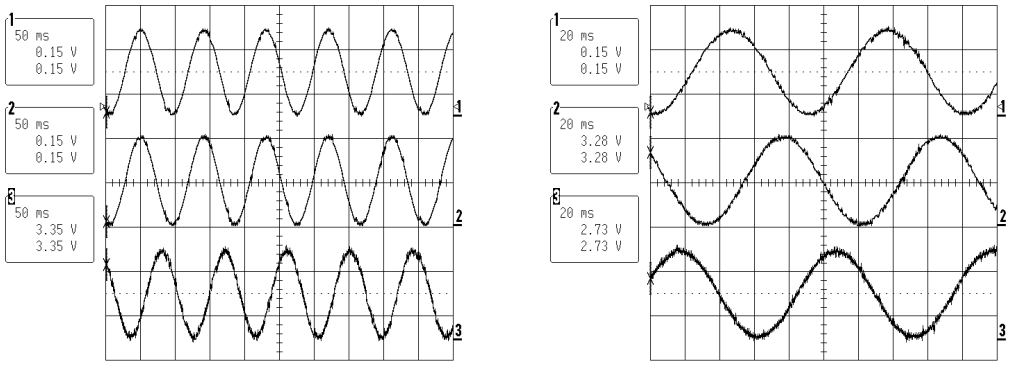

(a) 50 ms/div. (b) 20 ms/div.

Fig. 64. Each phase current reference waveform at 300 RPM [1A/div.].

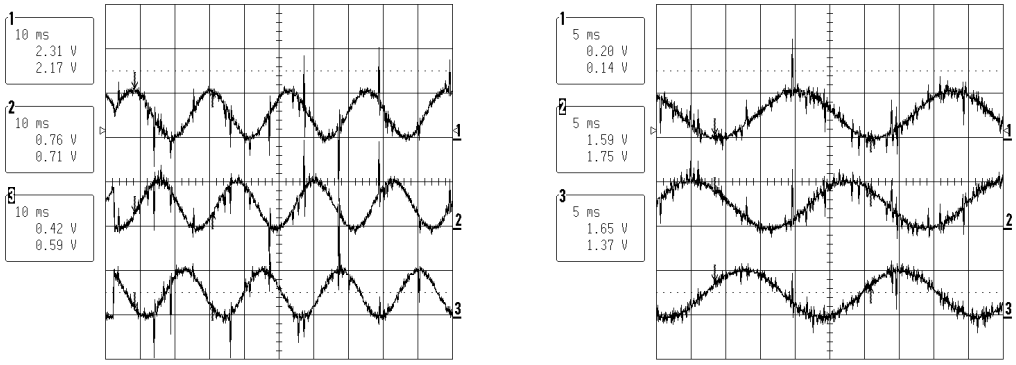

(a) 10 ms/div. (b) 5 ms/div.

Fig. 65. Each phase current reference waveform at 1350 RPM [12A/div.].

Fig. 66 shows each phase current reference waveform, controlled current and switching status at 1350 RPM. The controlled current waveform from the sub-optimal current reference is similar to the proposed controlled current waveform from the optimal current reference. The output power comparison of each method (conventional method, proposed control without a neutral point connection, proposed control with a neutral point connection and the sub-optimal method) is presented in Table VIII.

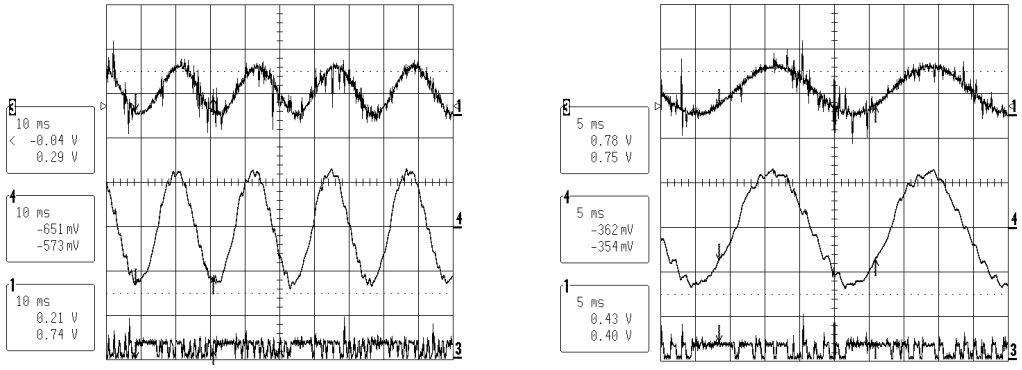

(a) 10 ms/div. (b) 5 ms/div.

Fig. 66. Each phase current reference waveform, controlled current and switching status at 1350 RPM [12A/div., 5A/div.].

Table VIII. Comparison of the electrical output power with the sub-optimal waveform.

Speed : 1350 RPM		RMS Current : 5.0A	
	Control Method	Output Power [W]	Increase [%]
Simulation	Diode Rectifier	251.1 [W]	
	Proposed Control	464.5 [W]	85 [%]
	Neutral Connection	475.1 [W]	89 [%]
	Sub-optimal	463.3 [W]	84.5 [%]
Experiment	Diode Rectifier	242.3 [W]	
	Proposed Control	346.8 [W]	43 [%]
	Neutral Connection	407.0 [W]	68 [%]
	Sub-optimal	343.2 [W]	41.7 [%]

Table VIII shows the comparison of the electrical output power of the BLDC generator when the sub-optimal current reference is applied. In the condition of 1350 RPM and 5.0A, four methods are compared. As shown in Table VIII, the case of sub-optimal has almost same electrical output power as the case of optimal current reference. The increase of output power is 84.5% in the simulation and 41.7% in the experiment, respectively.

From the study, it is known that in the practical application, by using the look-up-table the sinusoidal current reference waveform can replace the optimal current reference derived by the proposed control algorithm. However, note that this pure sinusoidal current waveform is a sub-optimal current waveform theoretically.

C. Load Variation Mode

The optimal current waveform and its control for the power density maximization have been described. Note that this derived current waveform is always optimal in every situation because the optimal current reference waveform is calculated by the induced EMF waveform which is already decided by the machine design and structure even if there is a load variation.

However, load variation causes DC-link voltage variation and electrical output power variation. If we do not need to consider the DC-link voltage regulation problem in the application, it is fine to apply the proposed control strategy in any situation. But if we need to consider the DC-link voltage regulation (in many applications, we need to consider it), it becomes a problem of a PI controller and PWM converter. In this section, load variation when the proposed control is applied will be discussed.

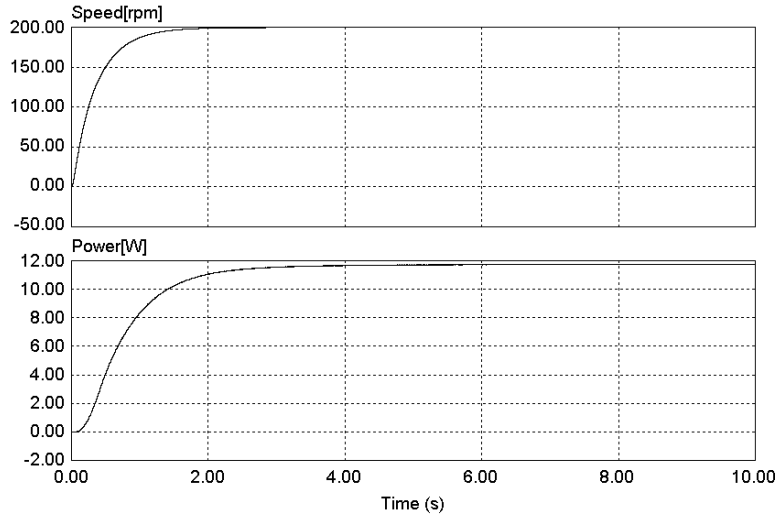

(a) Operating speed and output power

Fig. 67. Normal operation characteristics.

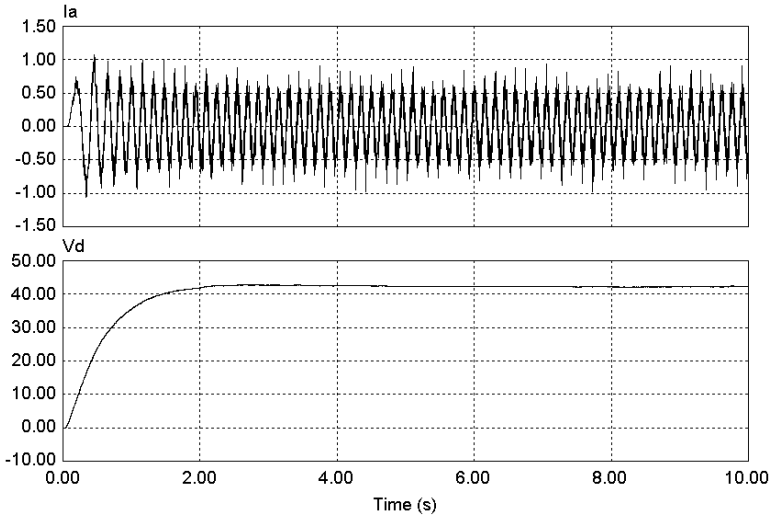

(b) Controlled current and regulated voltage

Fig. 67. Continued.

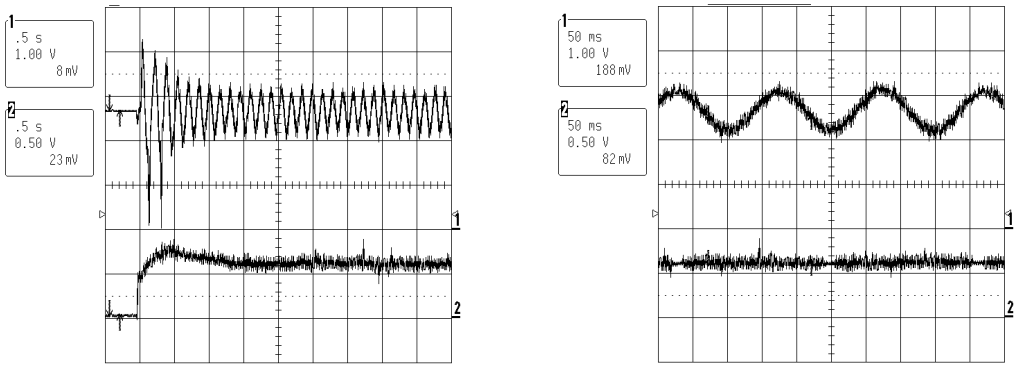

(a) 500 [ms/div.] (b) 50[ms/div.]

Fig. 68. Experimental results of the normal operation characteristics.

(Controlled current [1 A/div.] and DC-link voltage[35 V/div.])

Fig. 67(a) shows the speed of the generator and output power in the normal operation. The speed of the rotor is 200 RPM. Fig. 67(b) shows the phase current and regulated voltage. The output voltage is regulated to 42V by the PI controller. Fig. 68 shows the experimental results of the normal operation at the same speed. Transient

response of the generator is shown in Fig. 68(a) and steady-state response is shown in Fig. 68(b). As it is shown, the proposed control is working well. In order to investigate the performance of the generator with the proposed control, three cases of the load variation are described as following:

(1) Light load variation

(2) Medium load variation

(3) Heavy load variation

(1) Light load variation: 200% of the initial load

Fig. 69 shows the characteristics of the generator system in the case of the light load variation at the time of 5 seconds, stopping at 6 seconds. At the point that load is increased 100 percent at the time of 5 seconds, the DC-link voltage decreases but PI controller can regulate the voltage to the required voltage reference.

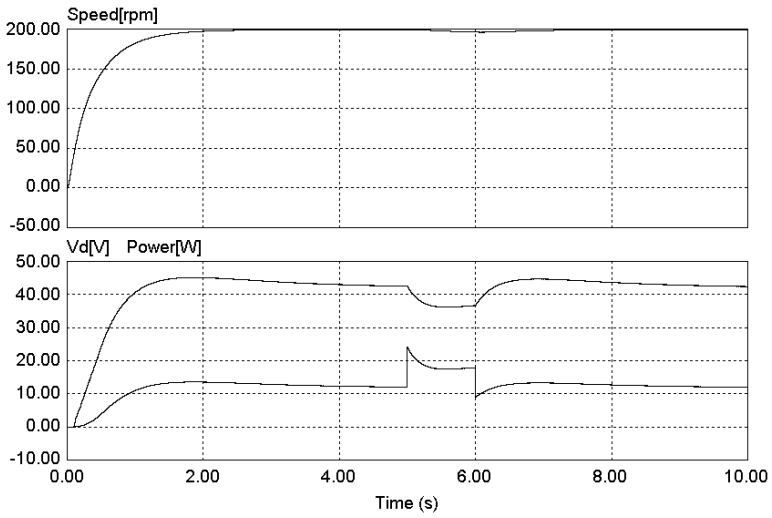

(a) Operating speed, output voltage and output power

Fig. 69. Characteristics of the generator system in the light load variation.

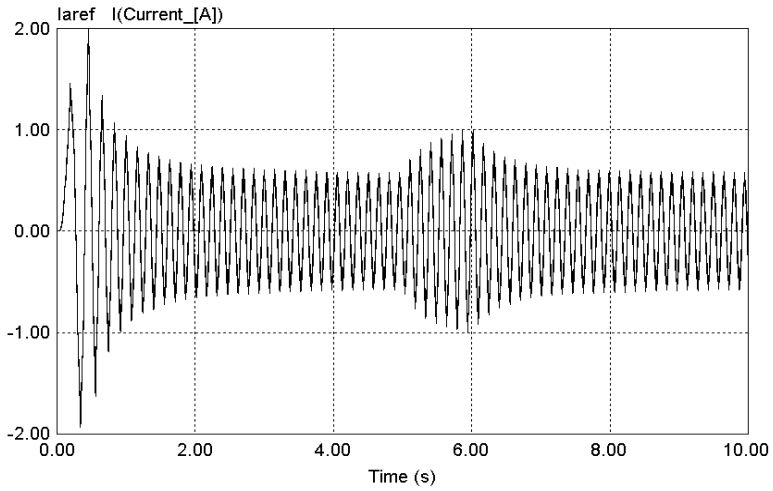

(b) Current reference and controlled current

Fig. 69. Continued.

After load changes at 5 seconds, the current reference and real currents increase slightly in order to transfer the output power to the increased load. Fig. 70 shows the experimental results of the DC-link voltage and current. In case of light load variation, Figs. 69 and 70 show that the proposed control does not have any problems in the light load variation, within the range that PI controller can operate with the given PI gain.

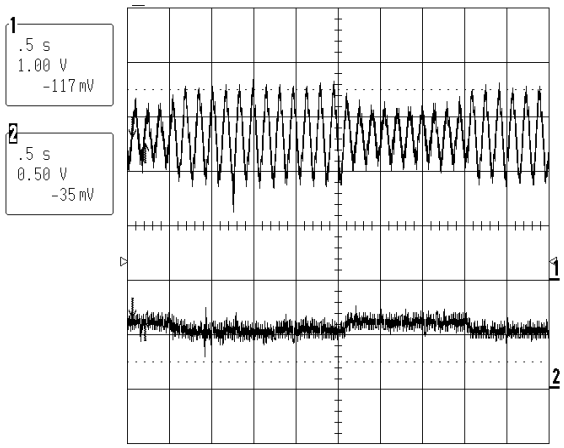

Fig. 70. Experimental results of the generator system in the light load variation.

(500 [ms/div.], Controlled current [1 A/div.] and DC-link voltage [35 V/div.])

(2) Medium load variation: 300% of the initial load

Fig. 71 shows the characteristics of the generator system in the case of the medium load variation at the time of 5 seconds, stopping at 6 seconds. The operating speed of the generator is 300 RPM and the regulated voltage is 48V.

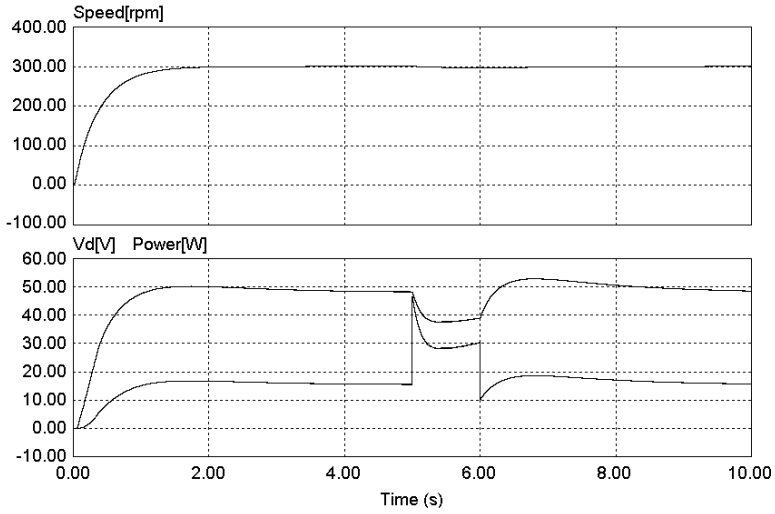

(a) Operating speed, output voltage and output power

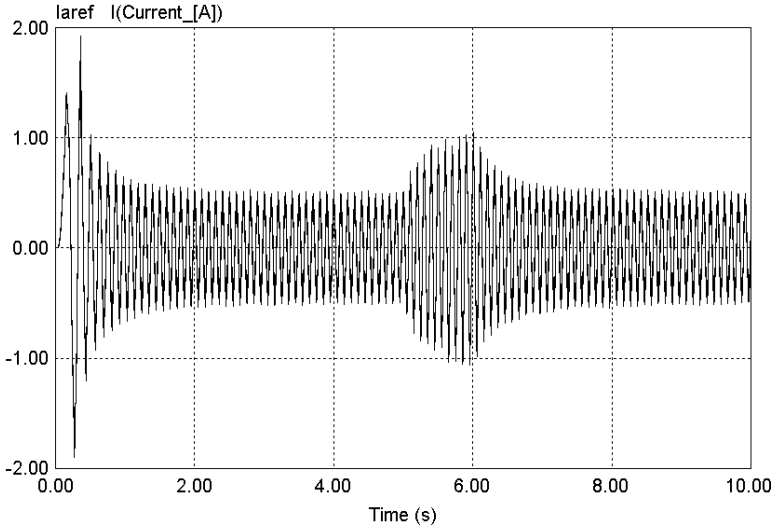

(b) Current reference and controlled current

Fig. 71. Characteristics of the generator system in the medium load variation.

At the point that load is increased to 300% of the initial load at the time of 5 seconds, the DC-link voltage decreases but the PI controller still can regulate the voltage to the required voltage reference. After load changes at 5 seconds, the current reference and real currents increase in order to transfer the output power to the increased load.

Fig. 72 shows the experimental results of the DC-link voltage regulation and current waveform. In the case of medium load variation, Figs. 71 and 72 show that the proposed control does not have any problem in the medium load variation, within the range that the PI controller can operate with the given PI gain. However if the load changes heavily, the PI controller cannot regulate the DC-link voltage for the reference voltage so the control will fail, as in the following section (3).

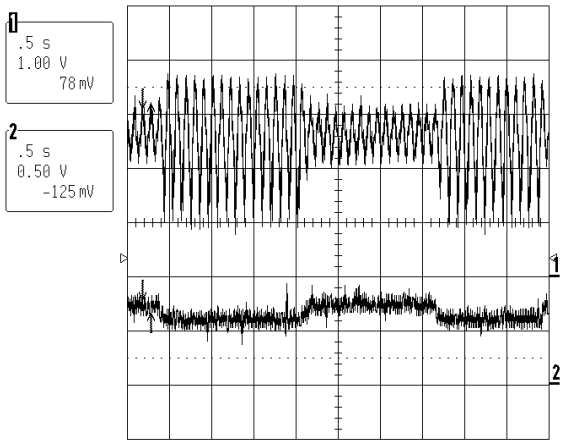

Fig. 72. Experimental results of the generator system in the medium load variation.

(500 [ms/div.], Controlled current [1 A/div.] and DC-link voltage [35 V/div.])

(3) Heavy load variation : 400% of the initial load

Fig. 73 shows the characteristics of the generator system in the case of the heavy load variation at the time of 5 seconds. The operating speed of the generator is 500RPM

and the regulated voltage is 90V. At the point that load is increased to the 400% of the initial load, the output power in the DC-link battery suddenly increases very quickly and goes to zero value, and DC-link voltage decreases and is not recovered. And current also increases quickly because the PI controller commands more current to recover the required DC-link voltage.

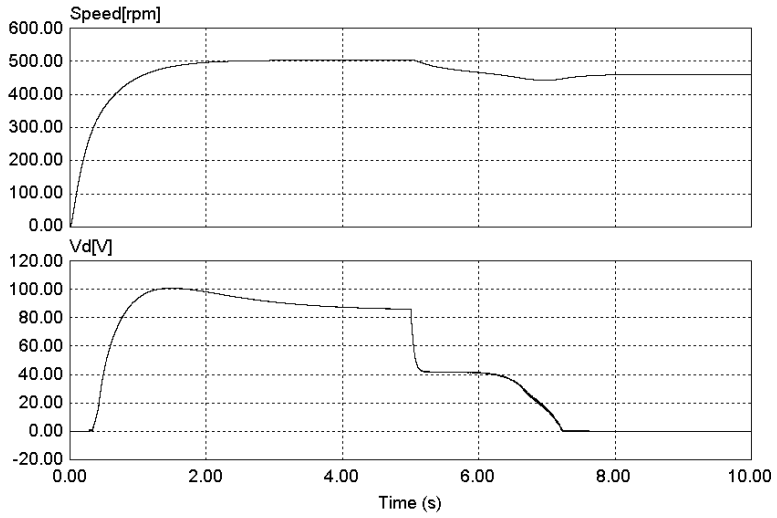

(a) Operating speed, output voltage and output power

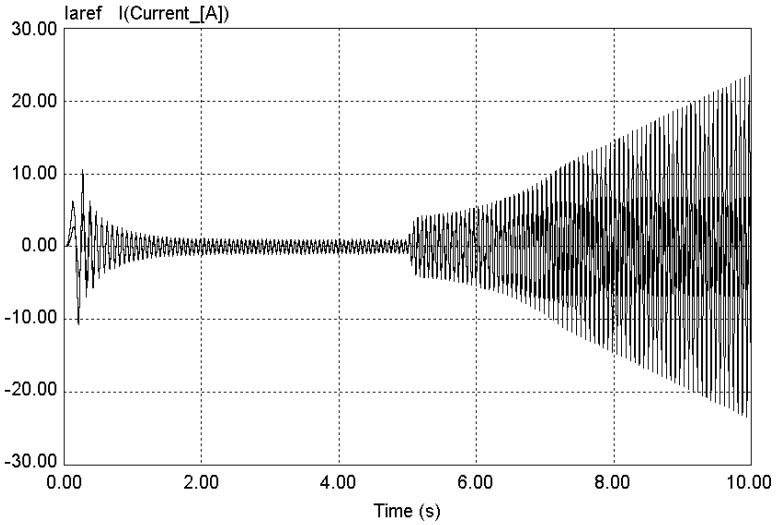

(b) Current reference and phase current (Zoom out)

Fig. 73. Characteristics of the generator system in the heavy load variation.

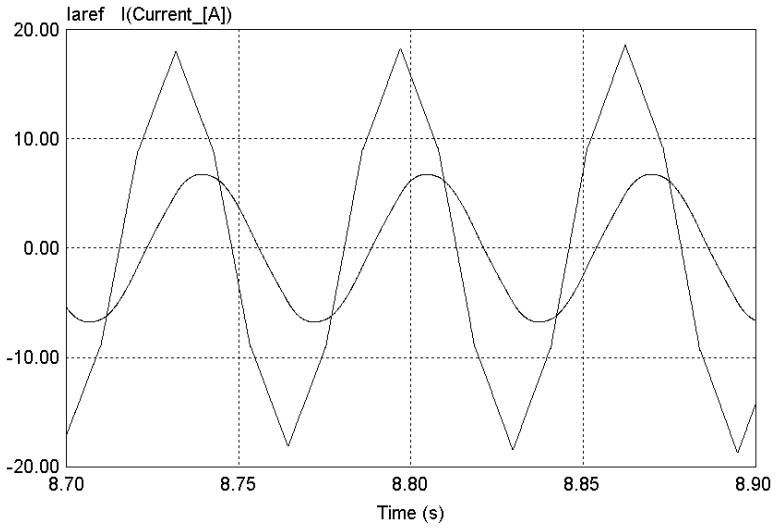

(c) Current reference and phase current (Zoom in)

Fig. 73. Continued.

However, in the heavy load case, the PI controller cannot regulate the output voltage by the given PI gain so the power goes down to zero the same as the voltage and we lose the control of currents as shown in Fig. 73(c). It is not a problem of the power density maximization theory but the problem is from the PI controller. In addition to the limit of the PI controller, there is another problem generated by the limitation of the current rating. Current cannot flow over the rating of the generator stator winding so that DC-link voltage cannot be regulated.

Fig. 74 shows the experimental results of the current waveform and the DC-link voltage. In the case of heavy load variation, Figs. 73 and 74 show that the given PI controller cannot regulate the DC-link voltage and we lose the control of currents. For various studies, the speed of the rotor and reference voltage are changed in every load case (light, medium and heavy).

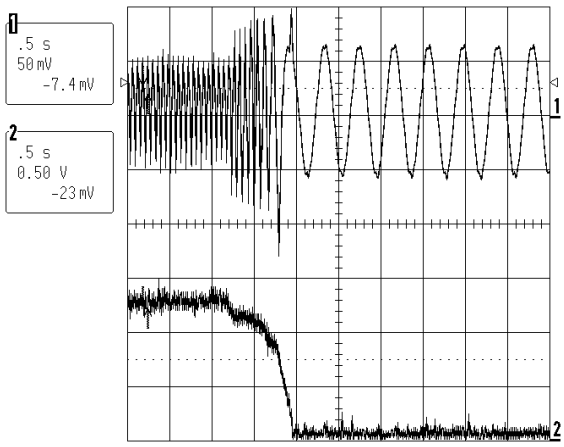

Fig. 74. Experimental results of the generator system in the heavy load variation. (500 [ms/div.], Controlled current [1 A/div.] and DC-link voltage [35 V/div.])

In this section, the effect of the load variation on the proposed control method is investigated. Limits of the PI controller and stator current rating in a heavy load variation create a problem for voltage regulation and results in a control failure, but note that it is not a problem of the proposed control algorithm.

D. One-phase Failure Mode

In general, the PM generator such as a BLDC generator is a small rating machine for the home application or transportation system. So there is little possibility for generator to be damaged and disconnected in a one-phase winding. Nevertheless, we cannot overlook the possibility that the phase line is disconnected by some accidents (harsh environment or manufacturing error, etc.). In this section, analysis of the one-phase failure mode is discussed and numerical simulations are presented.

(1) One phase failure with proposed control

Fig. 75(a) shows the speed and output power when the one phase line (phase C) is broken at 4 seconds. Since one line is disconnected, line-to-line EMF from the EMF calculation algorithm shows the incorrect waveform, and current reference also has miscalculation, as shown in Fig. 75(b). In case one phase is broken suddenly, the proposed control cannot accomplish the voltage regulation based on the given PI gain so that the DC-link voltage and output power suddenly goes to zero and the speed of the prime mover goes up slightly at that time, consequently. Since the proposed control is based on the balanced-phases BLDC generator; after one phase line is broken, the only path of the current is from phase A to phase B or the opposite way only. Therefore, each phase of the current is 180^{o} phase shifted so that we cannot make each phase voltage and current in phase because voltage is 120 ^{o} phase shifted. Fig. 75(c) shows the waveforms of each phase current.

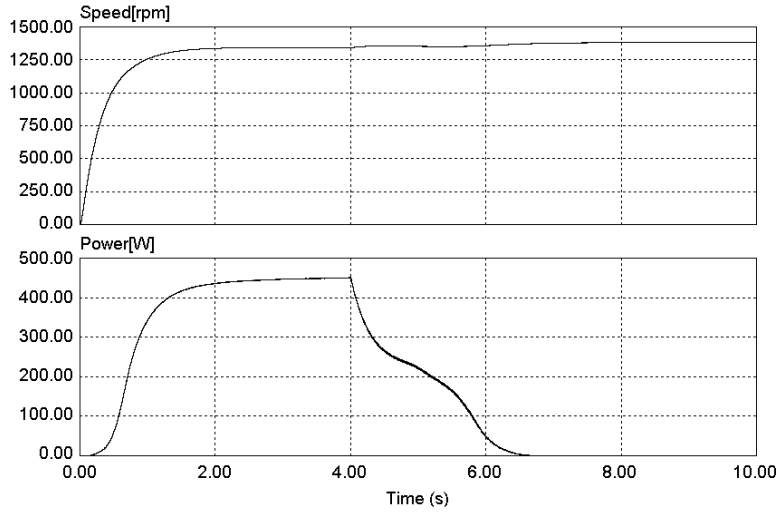

(a) Speed and output power variation

Fig. 75. Characteristics of the one phase failure operation.

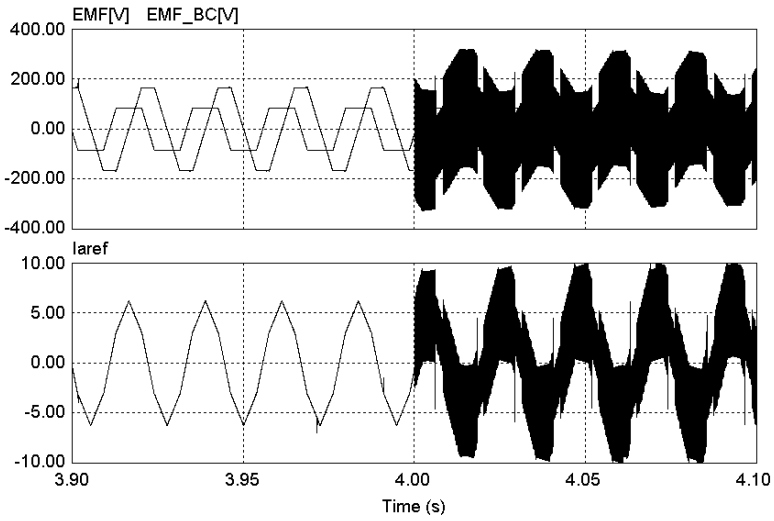

(b) EMF and current reference waveforms

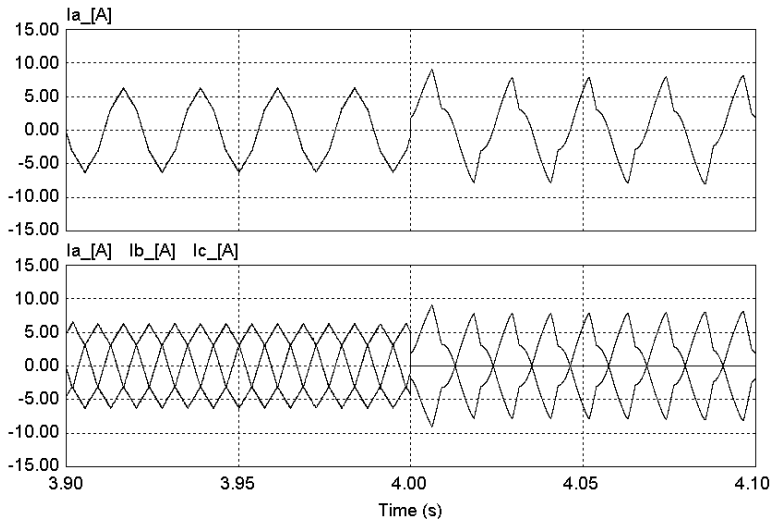

(c) One phase current and three phase currents

Fig. 75. Continued.

(2) One phase failure with a diode rectifier

Fig. 76 shows the characteristics of the one phase failure operation when the conventional diode rectifier is used in the generator system. Since the diode rectifier cannot control the DC-link voltage and phase currents, even though one phase is failed, it

provides a certain amount of the DC-link voltage and power. Because one phase winding is disconnected, the magnitude of the DC-link voltage and output power decreases to around one-third of the normal operation mode. The uncontrolled currents (Phase A and B) have opposite directions, and each phase of the current is 180^{o} phase shifted as shown in Fig. 76(b). Following sections, D. (3), (4), (5) propose alternative plans to keep some amount of the output power while one phase is disconnected.

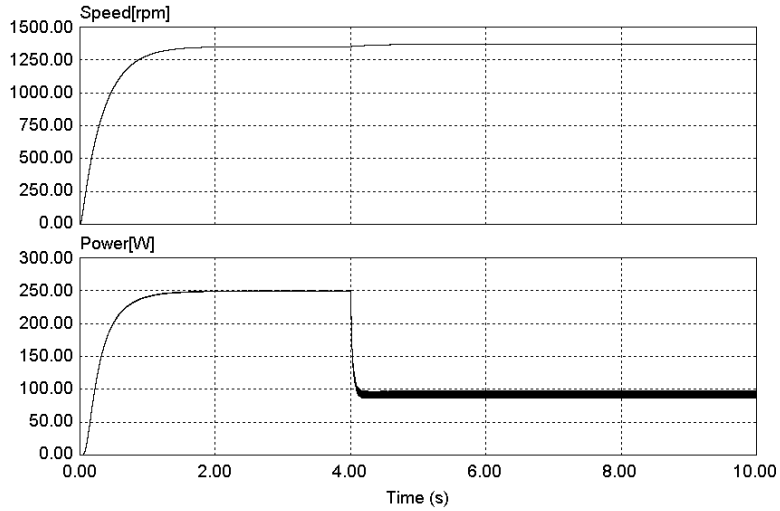

(a) Speed and output power

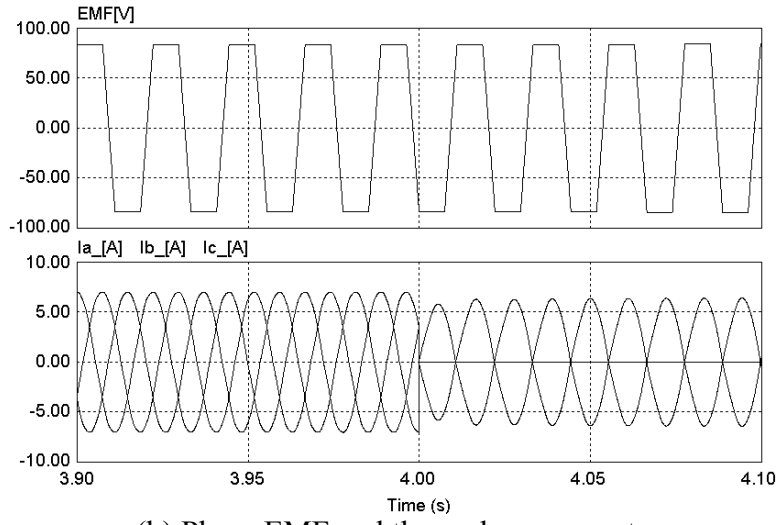

(b) Phase EMF and three phase currents

Fig. 76. Characteristics of the one phase failure mode with the diode rectifier.

(3) Replacing the proposed control with a diode rectifier in the accident

In case of one phase failure, the proposed control cannot provide the regulated DC-link voltage and it will go down to zero as shown above. However, a PWM converter has six freewheeling diodes besides the switches, so we can use these diodes as a full-bridge rectifier. If one phase failure happens, we can switch the PWM converter to the conventional diode rectifier (turn all six switches off) by the software and run the generator with a diode rectifier. Fig. 77 shows the simulation results when using the freewheeling diodes as a rectifier if the DC-link voltage drops under some voltage value because of the one phase failure. This backup algorithm increases reliability of the generator system so that the system can provide electrical output power even though one phase is disconnected.

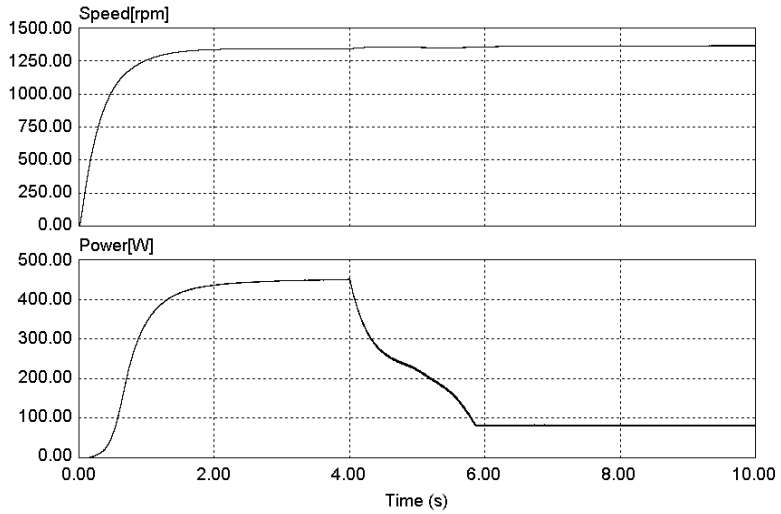

Fig. 77. Replacing the proposed control with a diode rectifier in case one phase is disconnected.

(4) One phase failure with the proposed control without voltage regulation

Besides of replacing the proposed control with a diode rectifier, there are other ways in order to keep the output power possible. As discussed in section D. (1), the control for voltage regulation fails in case of the one phase failure and results in zero output power. In the emergency situation such as one phase failure, we can switch the control algorithm from the proposed control to compensated control so as to abandon the voltage regulation operation and keep the output power possible. That is, the output of the PI controller will be set some value regardless of DC-link voltage magnitude and it will be used for the magnitude of the current reference. This magnitude of the current reference is stored to the control algorithm in the normal operation. Fig. 78 shows the speed of the rotor and output power when one phase is disconnected and compensated control algorithm is applied. As shown in Fig. 78, we lose some amount of the output power but still keep about half of the normal output power.

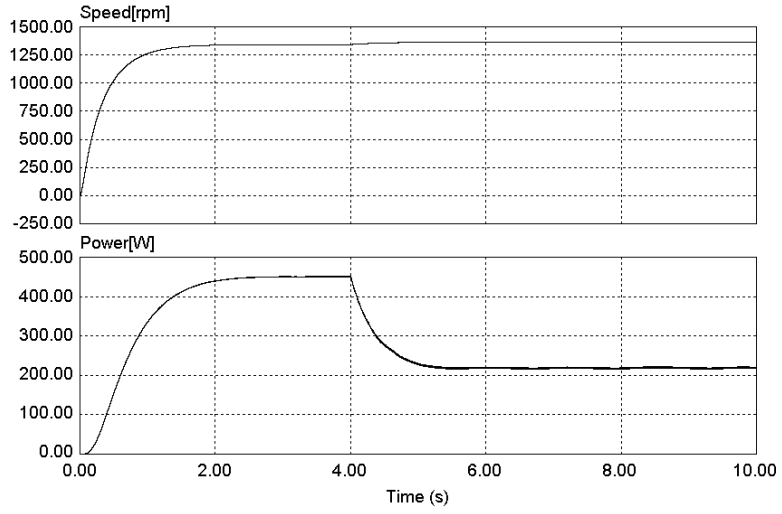

Fig. 78. One phase failure with the proposed control without voltage regulation.

(5) Two phases control while one phase failure

After one phase line is broken, the only path of the current is from phase A to phase B or the opposite way only. The equivalent circuit of the power supply system is shown in Fig. 79.

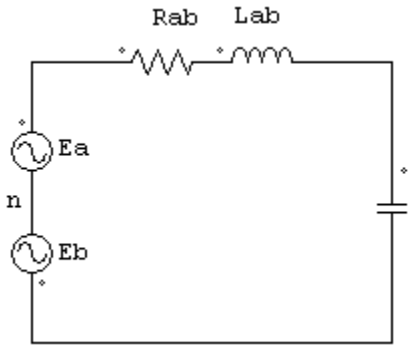

Fig. 79. Equivalent circuit when one phase is disconnected.

The optimal current waveform for power density maximization, in this case, is the same waveform as line-to-line EMF based on the theory in Chapter IV. Therefore, we need to modify the control algorithm when the accident happens. Fig. 80 shows the DC-link voltage and current reference. One phase is disconnected at 4 seconds and the modified control algorithm is applied when the DC-link voltage drops below than a certain value. The current reference waveform by the modified control algorithm is the same as the line-to-line EMF. Fig. 81 shows the phase current and three phase current waveforms before and after modified control algorithm is applied. Before the accident happens, the current waveform is the proposed controlled waveform and after the accident, the current waveform is uncontrollable. The current is controlled again after the DC-link voltage drop below than a certain value.

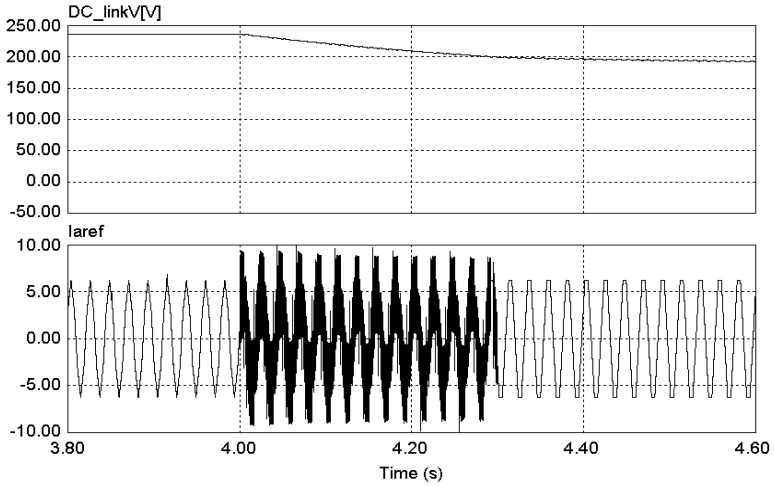

Fig. 80. DC-link voltage and current reference with modified control.

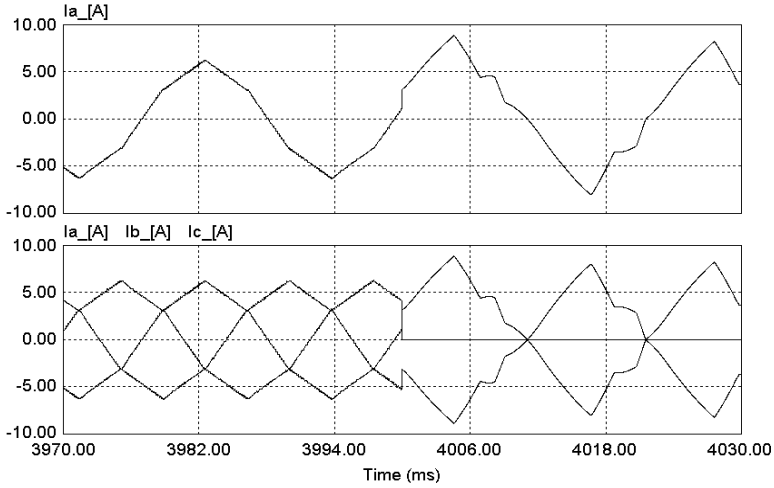

(a) Before modified control

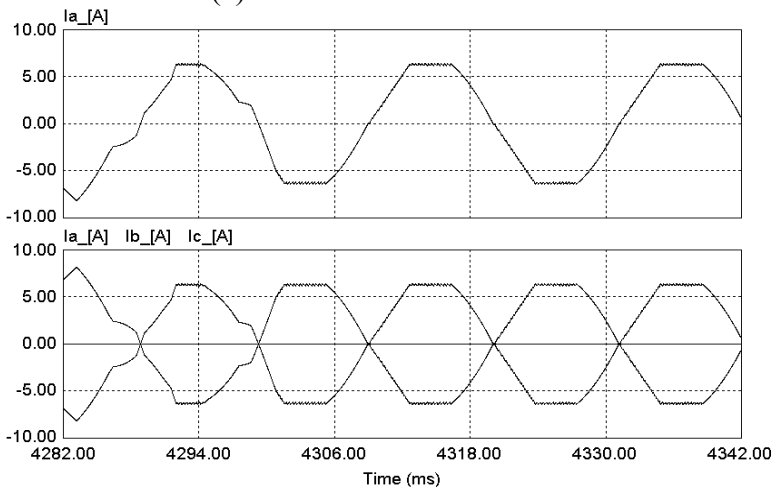

(b) After modified control

Fig. 81. One phase current and three phase currents with modified control.

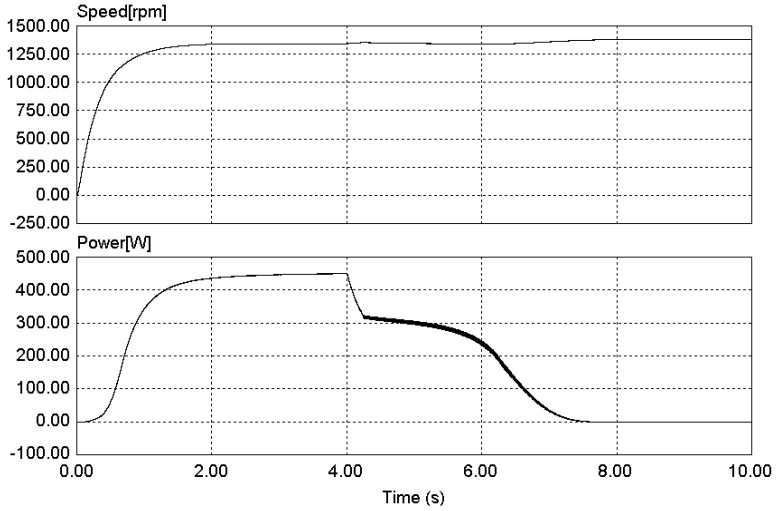

(a) With voltage regulation

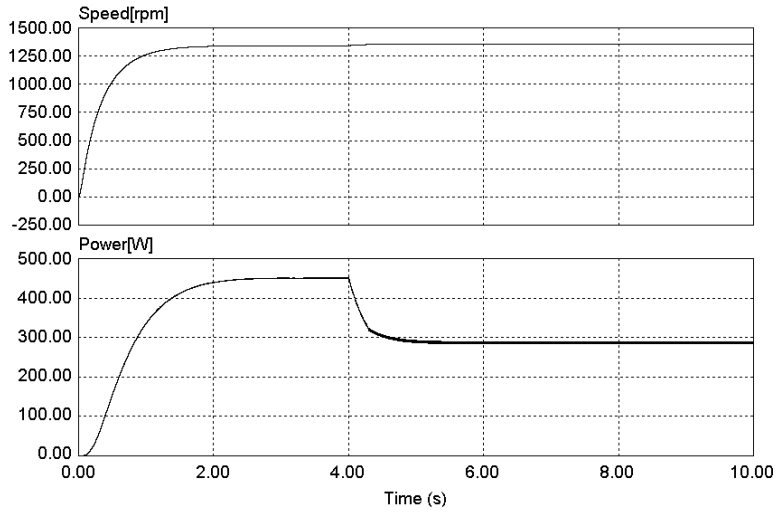

(b) Without voltage regulation

Fig. 82. Speed and output power with modified control.

Fig. 82 shows the output power when the modified control algorithm is applied. As discussed before, the failure of the PI control based on the given PI gain causes the power drop to zero even in the modified control. However, if we do not consider of the voltage regulation in case of one phase failure, because this is an emergency situation, modified control keep the output power around two third compared with the normal operation. It is very important to keep the power even in an accident.

E. Unbalanced Induced EMF Mode

The adverse conditions of heat and vibration to which electric machines are naturally exposed will occasionally lead to the progressive deterioration and eventual breakdown of the winding insulation in a phase of the machine. This internal fault, stator-winding failure resulted from breakdown of the turn-to-turn insulation, will give rise to unbalanced induced EMF that deteriorates generator system performance. Under the unbalanced induced EMF mode, proposed control for power density maximization is investigated and a method to compensate this unbalanced EMF situation is presented with the numerical simulation.

The magnitude of the total induced EMF with *N*-turn concentric windings is presented in (2.3):

$$E = 2N_S B_f lr\omega_r \tag{2.3}$$

Since induced EMF is proportional to the number of turns in a phase winding, the internal fault creates an unbalanced magnitude of the phase EMFs as shown in Fig. 83.

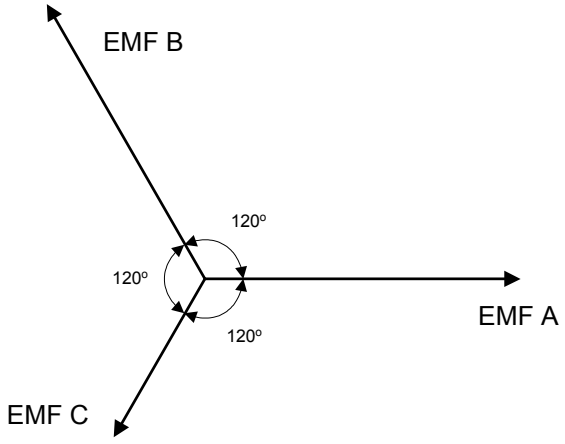

Fig. 83. Unbalanced magnitude of the phase EMFs.

Each phase EMF has harmonics as 1st, 3rd, 5th,… and an unbalanced magnitude of the each phase EMF is shown in (6.3). The sum of three phase EMFs can be categorized as zero and a zero-sequence component, as in (6.4). This zero sequence component is no longer multiple of the third harmonic because of the unbalanced situation.

$$\begin{aligned} e_a &= e_{a1} + e_{a3} + e_{a5} + \ldots = e_{am} + e_{az} \\ e_b &= p(e_{b1} + e_{b3} + e_{b5} + \ldots) = p(e_{bm} + e_{bz}) \\ e_c &= q(e_{c1} + e_{c3} + e_{c5} + \ldots) = q(e_{cm} + e_{cz}) \end{aligned} \tag{6.3}$$

$$\begin{aligned} &m = 1, 5, 7, 11, \ldots, \qquad \mathrm{z} = 3, 9, 15, 21, \ldots \\ &p = 1 + \varepsilon_b \qquad (-1 < \varepsilon_b < 0) \\ &q = 1 + \varepsilon_c \qquad (-1 < \varepsilon_c < 0) \end{aligned}$$

Here, p and q are proportional constant values of the phase B and C. ε_b and ε_c are an unbalanced magnitude of each phase. e_{am}, e_{bm}, e_{cm} are each phase balanced component.

$$\begin{aligned} e_a + e_b + e_c &= e_{am} + pe_{bm} + qe_{cm} + e_{az} + pe_{bz} + qe_{cz} \\ &= e_{am} + (1+\varepsilon_b)e_{bm} + (1+\varepsilon_c)e_{cm} + e_{az} + (1+\varepsilon_b)e_{bz} + (1+\varepsilon_c)e_{cz} \\ &= \underbrace{e_{am} + e_{bm} + e_{cm}}_{0} + \underbrace{e_{az} + e_{bz} + e_{cz} + \varepsilon_b e_{bm} + \varepsilon_c e_{cm} + \varepsilon_b e_{bz} + \varepsilon_c e_{cz}}_{\text{zero sequence}} \end{aligned} \tag{6.4}$$

Since $e_{az} = e_{bz} = e_{cz} = e_z$, sum of three phase EMFs can be presented as in (6.5):

$$\begin{aligned} e_a + e_b + e_c &= e_{az} + e_{bz} + e_{cz} + \varepsilon_b e_{bm} + \varepsilon_c e_{cm} + \varepsilon_b e_{bz} + \varepsilon_c e_{cz} \\ &= e_z + e_z + e_z + \varepsilon_b e_{bm} + \varepsilon_c e_{cm} + \varepsilon_b e_z + \varepsilon_c e_z \\ &= \varepsilon_b e_{bm} + \varepsilon_c e_{cm} + (3 + \varepsilon_b + \varepsilon_c) e_z \end{aligned} \tag{6.5}$$

Therefore:

$$\begin{aligned} e_z &= \frac{1}{(3 + \varepsilon_b + \varepsilon_c)} \{ e_a + e_b + e_c - \varepsilon_b e_{bm} - \varepsilon_c e_{cm} \} \\ &= e_{az} = e_{az} = e_{az} \end{aligned} \tag{6.6}$$

From (6.3):

$$\begin{aligned} e_{am} &= e_a - e_z \\ e_{bm} &= \frac{1}{p} e_b - e_z \\ e_{cm} &= \frac{1}{q} e_c - e_z \end{aligned} \tag{6.7}$$

By inserting (6.6) into (6.7),

$$e_{am} = e_a - \frac{1}{(3+\varepsilon_b+\varepsilon_c)}\{e_a + e_b + e_c - \varepsilon_b e_{bm} - \varepsilon_c e_{cm}\} \tag{6.8}$$

$$e_{bm} = \frac{1}{1+\varepsilon_b} e_b - \frac{1}{(3+\varepsilon_b+\varepsilon_c)}\{e_a + e_b + e_c - \varepsilon_b e_{bm} - \varepsilon_c e_{cm}\} \tag{6.9}$$

$$e_{cm} = \frac{1}{1+\varepsilon_c} e_c - \frac{1}{(3+\varepsilon_b+\varepsilon_c)}\{e_a + e_b + e_c - \varepsilon_b e_{bm} - \varepsilon_c e_{cm}\} \tag{6.10}$$

From (6.9),

$$\begin{aligned} e_{bm} &= \frac{1}{1+\varepsilon_b} e_b - \frac{e_a + e_b + e_c}{(3+\varepsilon_b+\varepsilon_c)} + \frac{\varepsilon_b}{(3+\varepsilon_b+\varepsilon_c)} e_{bm} + \frac{\varepsilon_c}{(3+\varepsilon_b+\varepsilon_c)} e_{cm} \\ \frac{3+\varepsilon_c}{(3+\varepsilon_b+\varepsilon_c)} e_{bm} &= \frac{1}{1+\varepsilon_b} e_b - \frac{e_a + e_b + e_c}{(3+\varepsilon_b+\varepsilon_c)} + \frac{\varepsilon_c}{(3+\varepsilon_b+\varepsilon_c)} e_{cm} \end{aligned} \tag{6.11}$$

By inserting (6.11) into (6.10),

$$\begin{aligned} e_{cm} &= \frac{1}{1+\varepsilon_c} e_c - \frac{e_a + e_b + e_c}{(3+\varepsilon_b+\varepsilon_c)} + \frac{\varepsilon_b}{(3+\varepsilon_b+\varepsilon_c)} e_{bm} + \frac{\varepsilon_c}{(3+\varepsilon_b+\varepsilon_c)} e_{cm} \\ &= \frac{1}{1+\varepsilon_c} e_c - \frac{e_a + e_b + e_c}{(3+\varepsilon_b+\varepsilon_c)} + \frac{\varepsilon_c}{(3+\varepsilon_b+\varepsilon_c)} e_{cm} \\ &\quad + \frac{\varepsilon_b}{(3+\varepsilon_c)}\left\{\frac{1}{1+\varepsilon_b} e_b - \frac{e_a + e_b + e_c}{(3+\varepsilon_b+\varepsilon_c)} + \frac{\varepsilon_c}{(3+\varepsilon_b+\varepsilon_c)} e_{cm}\right\} \end{aligned} \tag{6.12}$$

The term of e_{cm} is summarized as in (6.13):

$$e_{cm} - \frac{\varepsilon_c}{(3+\varepsilon_b+\varepsilon_c)}e_{cm} - \frac{\varepsilon_b}{(3+\varepsilon_c)}\frac{\varepsilon_c}{(3+\varepsilon_b+\varepsilon_c)}e_{cm}$$
$$= \frac{1}{1+\varepsilon_c}e_c - \frac{e_a+e_b+e_c}{(3+\varepsilon_b+\varepsilon_c)} + \frac{\varepsilon_b}{(3+\varepsilon_c)}\left\{\frac{1}{1+\varepsilon_b}e_b - \frac{e_a+e_b+e_c}{(3+\varepsilon_b+\varepsilon_c)}\right\}$$

$$\frac{3}{(3+\varepsilon_c)}e_{cm} = \frac{1}{1+\varepsilon_c}e_c - \frac{e_a+e_b+e_c}{(3+\varepsilon_b+\varepsilon_c)} + \frac{\varepsilon_b}{(3+\varepsilon_c)}\left\{\frac{1}{1+\varepsilon_b}e_b - \frac{e_a+e_b+e_c}{(3+\varepsilon_b+\varepsilon_c)}\right\}$$

$$\therefore \quad e_{cm} = \frac{1}{3}\left\{-e_a - \frac{1}{1+\varepsilon_b}e_b + \frac{2}{1+\varepsilon_c}e_c\right\} \tag{6.13}$$

By inserting (6.13) into (6.11),

$$e_{bm} = \frac{1}{3}\left\{-e_a + \frac{2}{1+\varepsilon_b}e_b - \frac{1}{1+\varepsilon_c}e_c\right\} \tag{6.14}$$

By inserting (6.13) and (6.14) into (6.11),

$$e_{am} = \frac{1}{3}\left\{2e_a - \frac{1}{1+\varepsilon_b}e_b - \frac{1}{1+\varepsilon_c}e_c\right\} \tag{6.15}$$

Therefore, each phase optimal current reference for power density maximization of the three-phase unbalanced BLDC generator is (6.16):

$$\begin{bmatrix} i_a^* \\ i_b^* \\ i_c^* \end{bmatrix} = g \cdot \begin{bmatrix} e_{am} \\ e_{bm} \\ e_{cm} \end{bmatrix} = g \cdot \frac{1}{3}\begin{bmatrix} 2 & -\frac{1}{1+\varepsilon_b} & -\frac{1}{1+\varepsilon_c} \\ -1 & +\frac{2}{1+\varepsilon_b} & -\frac{1}{1+\varepsilon_c} \\ -1 & -\frac{1}{1+\varepsilon_b} & \frac{2}{1+\varepsilon_c} \end{bmatrix}\begin{bmatrix} e_a \\ e_b \\ e_c \end{bmatrix} \tag{6.16}$$

Here, g is a proportional gain from the voltage controller. If the system is balanced, ε_b and ε_c are null, matrix (6.16) is same as (4.41) in chapter IV.

Figs. 84 through 91 show the simulation results which investigate the unbalanced induced EMF mode and verify the compensated algorithm for making a balanced system. A hysteresis controller is used for current control and the band of the controller is 0.05A. The switching frequency of the simulation is 20kHz. Comparison of the electrical output power of the unbalanced BLDC generator has been presented in Table VIII at the end of this section.

Fig. 84 shows the simulation results of the 20% unbalanced EMF of phase C and the zero-sequence eliminated-phase EMFs by using the proposed control algorithm. The magnitude of EMF in the phase C is 20% lower than of other phases, so that the peak value of the *EMF_cm*, the zero-sequence eliminated EMF of phase C, is a bit smaller than the other zero-sequence eliminated EMFs, and the waveforms of *EMF_am* and *EMF_bm* are a bit twisted. The optimal current reference waveforms and controlled current waveforms are presented in Fig. 85.

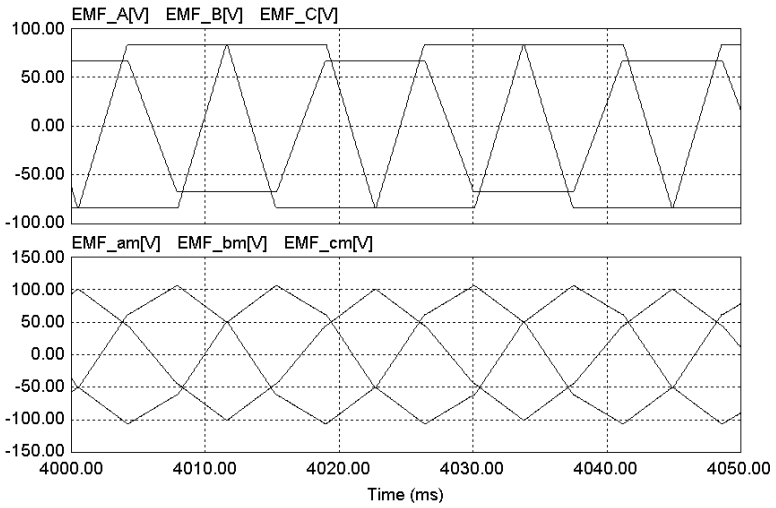

Fig. 84. Simulated phase EMFs and zero-sequence eliminated phase EMFs under 20% unbalanced EMF mode.

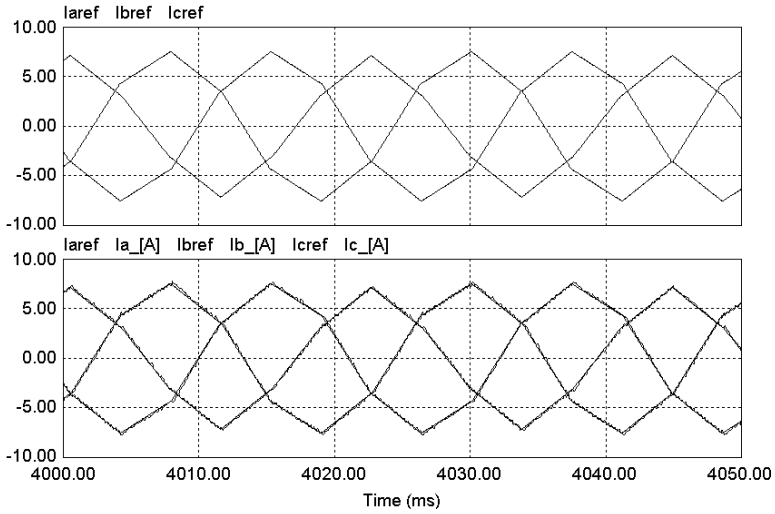

Fig. 85. Each phase optimal current reference waveform and controlled currents under 20% unbalanced EMF mode.

Fig. 86 shows the simulation results of the 50% unbalanced EMF of phase C and the zero-sequence eliminated-phase EMFs by using the proposed control algorithm.

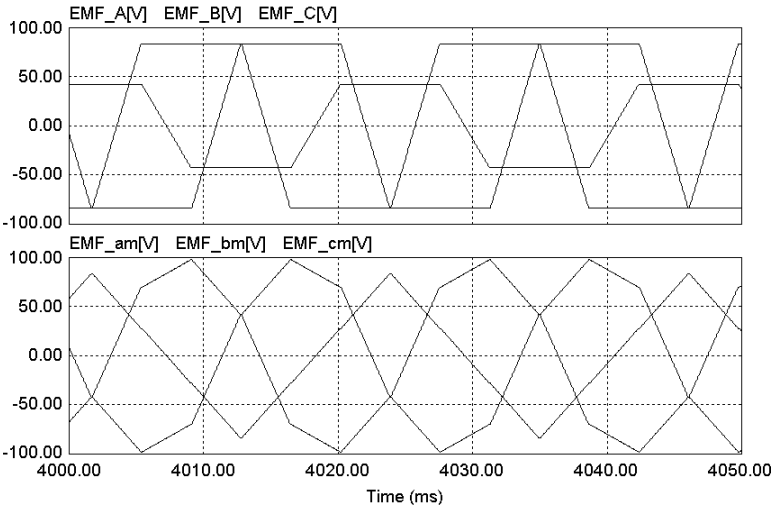

Fig. 86. Simulated phase EMFs and zero-sequence eliminated-phase EMFs under 50% unbalanced EMF mode.

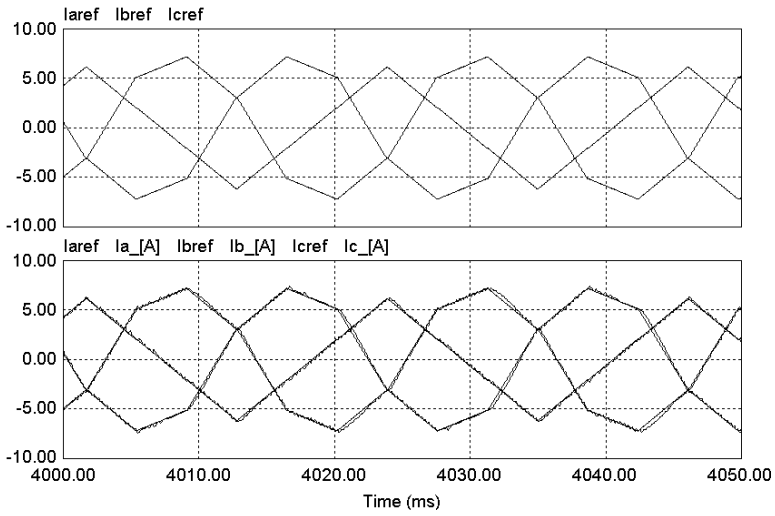

Fig. 87. Each phase optimal current reference waveform and controlled currents under 50% unbalanced EMF mode.

The magnitude of EMF in the phase C is 50% lower than of other phases so that the peak value of the *EMF_cm* is a bit smaller than other zero-sequence eliminated EMFs, and the waveforms of *EMF_am* and *EMF_bm* are awfully twisted because of the unbalance. The optimal current reference waveforms and controlled current waveforms are presented in Fig. 87.

The proposed control method for power density maximization is developed based on the balanced three-phase power generator system. In the unbalanced system as above, we need to revise the control algorithm as derived in (6.16) in order to compensate for the unbalanced three-phase system, and so as to balanced three-phase system. The following numerical simulations show the compensated control for an unbalanced system.

Fig. 88 shows the simulation results of the 20% unbalanced EMF of phase C and the zero-sequence eliminated-phase EMFs by using a compensated control algorithm. Even though the magnitude of EMF in the phase C is 20% lower than in other phases,

each phase zero-sequence eliminated EMFs are balanced. The optimal current reference waveforms and controlled current waveforms are also presented in Fig. 89.

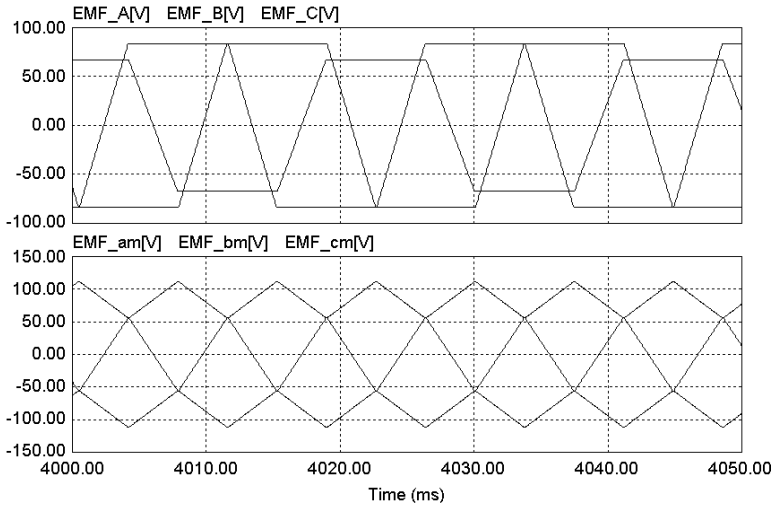

Fig. 88. Phase EMFs and zero-sequence eliminated phase EMFs under 20% unbalanced EMF mode with the compensated control algorithm.

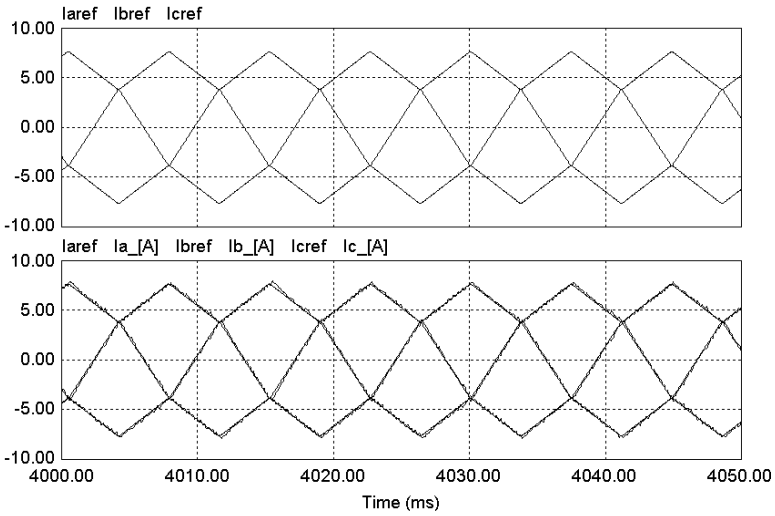

Fig. 89. Each phase optimal current reference waveform and controlled currents under 20% unbalanced EMF mode with the compensated control algorithm.

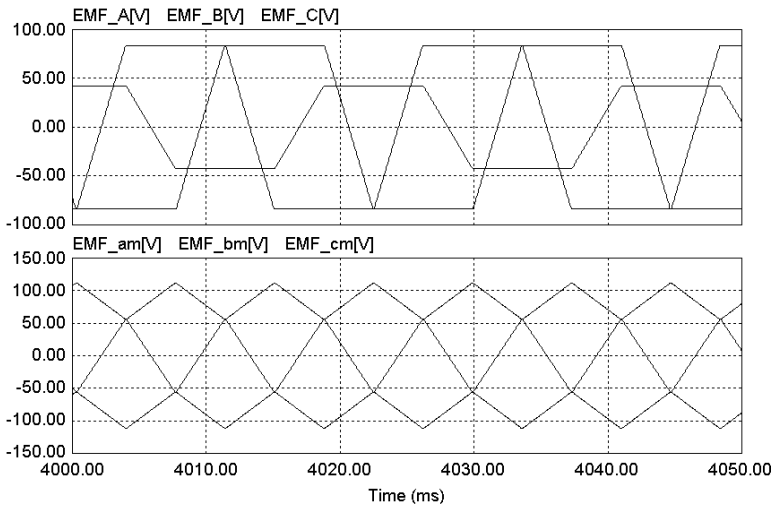

Fig. 90. Phase EMFs and zero-sequence eliminated-phase EMFs under 50% unbalanced EMF mode with the compensated control algorithm.

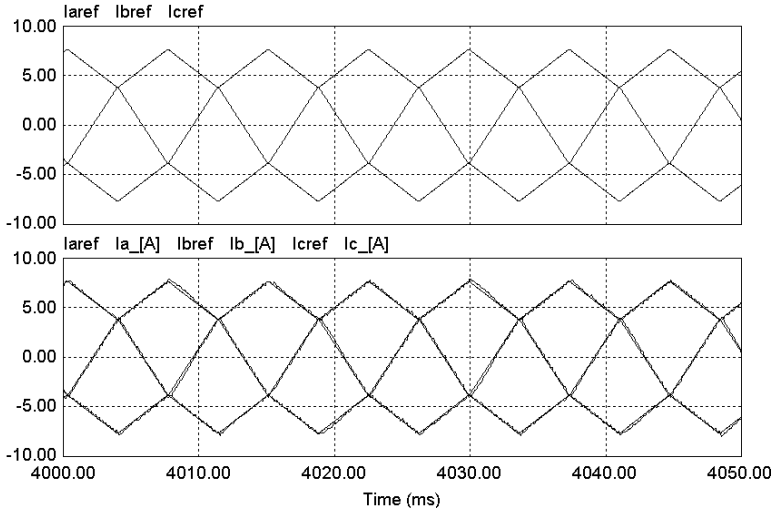

Fig. 91. Each phase optimal current reference waveform and controlled currents under 50% unbalanced EMF mode with the compensated control algorithm.

Fig. 90 shows the simulation results of the 50% unbalanced EMF of phase C and the zero-sequence eliminated-phase EMFs by using compensated control algorithm. Even though the magnitude of EMF in the phase C is 50% lower than in other phases, each

zero-sequence eliminated-phase EMFs are balanced the same as a 20% unbalanced system. The optimal current reference waveforms and controlled current waveforms are also presented in Fig. 91.

In Table IX, an output power comparison in each case of the unbalanced three-phase BLDC generator system is presented. In a balanced system, proposed control for power density maximization provides 464.5W. In the unbalanced system, the unbalanced phase EMF is smaller than in other phases so that the output power is reduced, as shown in Table IX. However, note that the output power using the proposed control is larger than with a conventional diode rectifier, even though phase EMF is unbalanced. The output power of the 20% and 50% unbalanced EMF modes with the compensated control algorithm is also presented. It shows that the compensated control algorithm increases output power a bit more than proposed control method.

Table IX. Comparison of the electrical output power of the unbalanced BLDC generator

Speed : 1350 RPM	RMS Current : 5.0A	
Mode	Output Power [W]	Decrease [%]
Balanced with diode rectifier	251.1 [W]	N/A
Balanced with proposed control	464.5 [W]	-
20[%] unbalanced with proposed control	411.5 [W]	11.41 [%]
50[%] unbalanced with proposed control	340.2 [W]	26.76 [%]
20[%] unbalanced with the compensated	418.7 [W]	9.86 [%]
50[%] unbalanced with the compensated	345.8 [W]	25.55 [%]

From the research of the unbalanced induced EMF mode, it is verified that the proposed control works properly and increases the output power even though the system is unbalanced. The power ripple caused by the unbalanced EMF and the twisted current waveforms cannot be reduced by using the proposed control method. Contrarily, since the compensated control algorithm makes the currents waveforms balanced three-phase, we can expect that the power ripple can be reduced significantly and the shaft vibration of the prime mover also can be reduced. Note that this work is based on the assumption that we know the each phase EMF and the unbalanced magnitude of each phase (ε_b and ε_c).

F. Multi-phase Mode

In this dissertation, the proposed control method for power density maximization is based on the three-phase balanced system. However, this control algorithm can also be applied to the multi-phase system as well. In Chapter IV, (4.28) shows the optimal current reference waveforms for power density maximization. As is shown, each phase current waveform should be the same as each phase zero-sequence eliminated EMF waveform because the zero-sequence component does not contribute to the output power and each phase current does not have the zero-sequence component in the Wye connection. And this theory can also be applied to multi-phase system.

$$\therefore \quad i_{abc}(t) = g \cdot e_{abcm}(t) \tag{4.28}$$

Where, g is the gain for the current reference.

For an n-phase system, optimal phase current waveform is as following:

$$i_n(t) = g \cdot e_{nm}(t) \qquad n : each\ phase\ \ (a,b,c,....) \tag{6.17}$$

Here, $e_{nm}(t)$ is the zero-sequence eliminated phase EMF and the zero-sequence component is the multiple of (number of phase)th harmonic in the balanced n-phase system. For example, in the five-phase system, optimal phase current waveform is:

$$i_{a,b,c,d,e}(t) = g \cdot e_{am,bm,cm,dm,em}(t) \tag{6.18}$$

and the zero-sequence component is a multiple of 5th harmonic such as 5, 15, 25, ….

In order to eliminate the specific harmonic, zero-sequence component, a simple algebraic method is proposed in Chapter IV. (4.41) shows the optimal current waveforms of the three-phase BLDC generator from the line-to-line EMFs.

$$\begin{bmatrix} i_a^* \\ i_b^* \\ i_c^* \end{bmatrix} = g \cdot \begin{bmatrix} e_{am} \\ e_{bm} \\ e_{cm} \end{bmatrix} = g \cdot \frac{1}{3} \begin{bmatrix} e_a - e_b + e_a - e_c \\ e_b - e_a + e_b - e_c \\ e_c - e_a + e_c - e_b \end{bmatrix} = \frac{g}{3} \begin{bmatrix} 1 & 0 & -1 \\ -1 & 1 & 0 \\ 0 & -1 & 1 \end{bmatrix} \begin{bmatrix} e_{ab} \\ e_{bc} \\ e_{ca} \end{bmatrix} \tag{4.41}$$

Here, g is a proportional gain from the voltage controller.

This simple algebraic method is adopted and extended for zero-sequence elimination in the multi-phase system as in (6.19).

$$\left[i_n^*\right] = g \cdot \left[e_{nm}\right] = g \cdot \frac{1}{n} \underbrace{\begin{bmatrix} n-1 & -1 & \cdots & \cdots & -1 \\ -1 & \ddots & & & \vdots \\ \vdots & & \ddots & & \vdots \\ \vdots & & & \ddots & -1 \\ -1 & \cdots & \cdots & -1 & n-1 \end{bmatrix}}_{n} \left[e_n\right] \tag{6.19}$$

Here, g is a proportional gain from the voltage controller.

For example, in the five-phase system, optimal phase current waveform for power density maximization is shown in (6.20). Since many manufacturers do not provide the neutral point, phase current reference waveforms should be calculated by the line-to-line EMFs.

$$\begin{bmatrix} i_a^* \\ i_b^* \\ i_c^* \\ i_d^* \\ i_e^* \end{bmatrix} = g \cdot \begin{bmatrix} e_{am} \\ e_{bm} \\ e_{cm} \\ e_{dm} \\ e_{em} \end{bmatrix} = g \cdot \frac{1}{5} \begin{bmatrix} 4 & -1 & -1 & -1 & -1 \\ -1 & 4 & -1 & -1 & -1 \\ -1 & -1 & 4 & -1 & -1 \\ -1 & -1 & -1 & 4 & -1 \\ -1 & -1 & -1 & -1 & 4 \end{bmatrix} \begin{bmatrix} e_a \\ e_b \\ e_c \\ e_d \\ e_e \end{bmatrix}$$

$$= \frac{g}{5} \begin{bmatrix} 1 & 1 & 1 & 1 & 0 & 0 & 0 & 0 & 0 & 0 \\ -1 & 0 & 0 & 0 & 1 & 1 & 1 & 0 & 0 & 0 \\ 0 & -1 & 0 & 0 & -1 & 0 & 0 & 1 & 1 & 0 \\ 0 & 0 & -1 & 0 & 0 & -1 & 0 & -1 & 0 & 1 \\ 0 & 0 & 0 & -1 & 0 & 0 & -1 & 0 & -1 & -1 \end{bmatrix} \begin{bmatrix} e_{ab} \\ e_{ac} \\ e_{ad} \\ e_{ae} \\ e_{bc} \\ e_{bd} \\ e_{be} \\ e_{cd} \\ e_{ce} \\ e_{de} \end{bmatrix} \quad (6.20)$$

Figs. 92 through 94 show the simulation results of the multi-phase BLDC generator system. Since three-phase or five-phase is general in the machine structure, the five-phase is used for the example of multi-phase BLDC generator.

Five-phase EMFs are shown in Fig. 92. It is assumed that each phase is shifted 72^o electrical angle and is identical in shape.

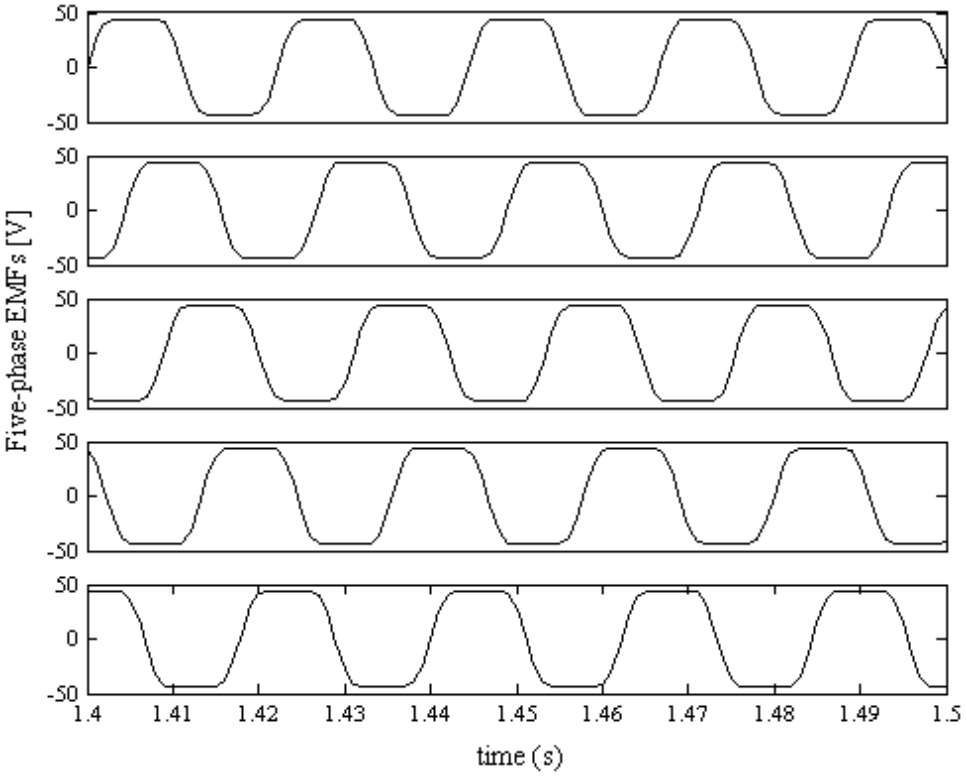

Fig. 92. Five-phase induced EMFs.

Fig. 93 presents five phase zero-sequence eliminated EMFs, which are derived by using (6.20) for power density maximization. These waveforms do not have multiple of fifth harmonic.

Phase EMF waveform and optimal current reference waveform are shown in Fig. 94. Both of them are in phase and the current reference does not have a zero-sequence component. From the study, it is verified that the proposed simple algebraic method for eliminating zero-sequence component in the balanced system can be used for any phase system.

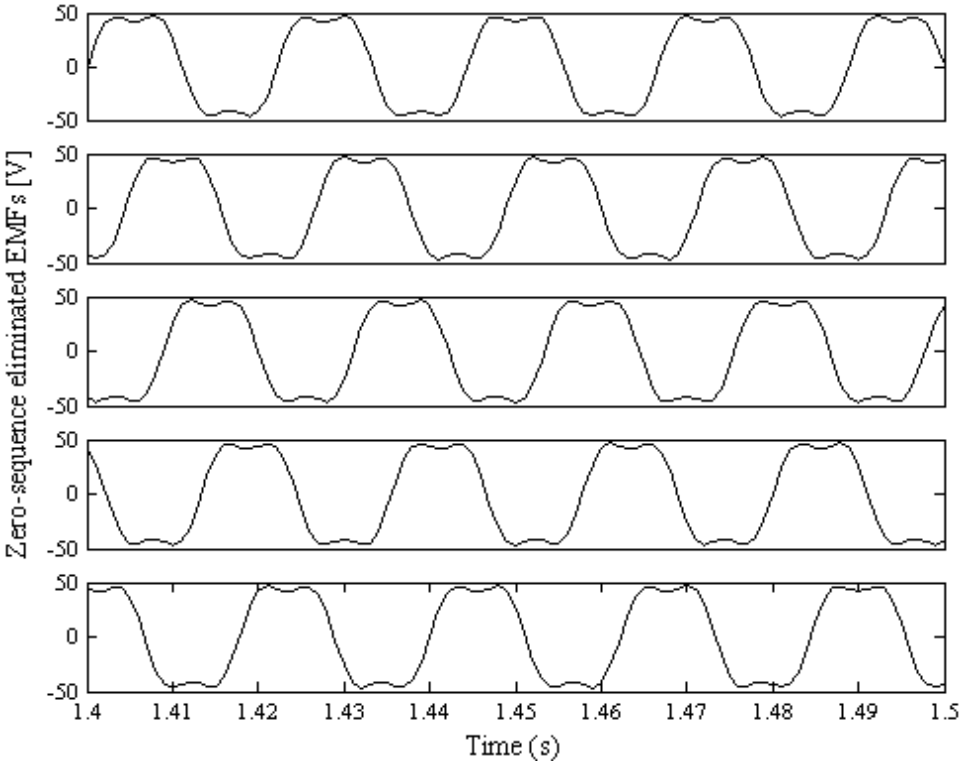

Fig. 93. Five-phase zero-sequence eliminated EMFs.

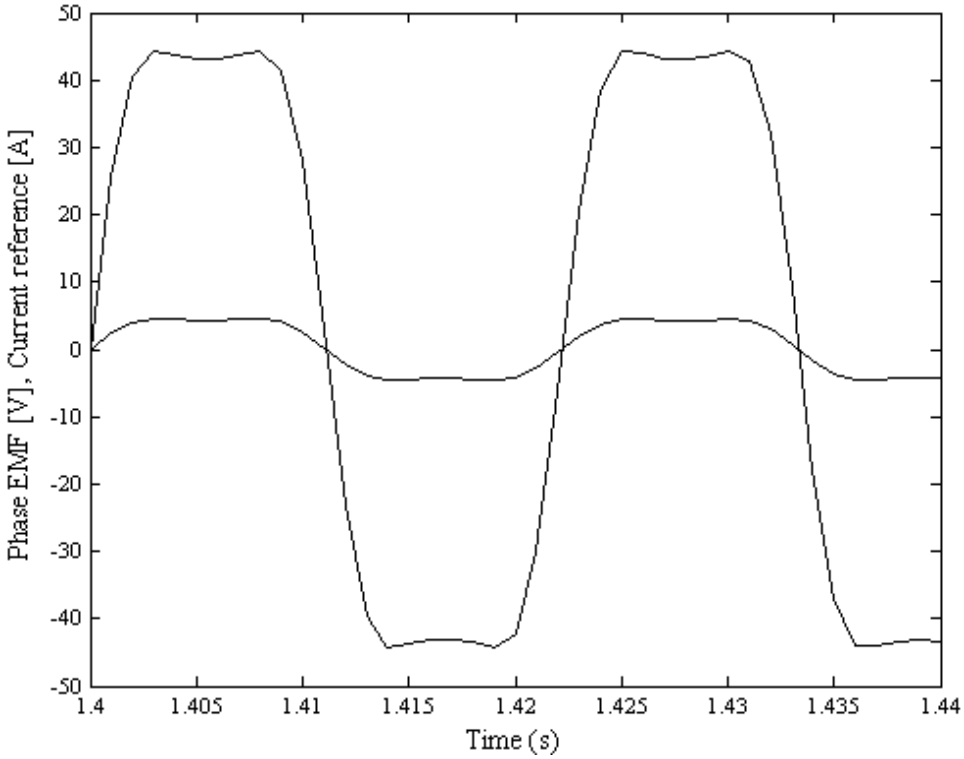

Fig. 94. Phase EMF and optimal current reference waveforms.

G. Error Analysis

The simulation and experimental results of the proposed control method are presented in the previous chapters and sections to show the validity of the proposed method. Since there are several kinds of error sources in the experiment, it is obvious that the simulation results are better than the experimental results. The various sources of the error are investigated and the analysis of the effects from the sources is presented in this section; the output power under the error sources is also analyzed.

1. Sources of the error in the proposed current reference waveform

The error of the current reference calculation in an experimental system is generated by the following factors:

1) Measurement errors
2) Parameter errors by manufacturing imperfections and temperature variation
3) Limited sampling rate

1) Measurement errors

The accuracy of the measured or estimated voltage and current directly affects the accuracy of the proposed control algorithm. When a phase is conducting, the phase voltage can be assumed to be equal to the DC-link voltage or negative of the DC-link voltage based on the switching status of the phase. The voltage drop on the active switches and diodes leads to a certain error in phase voltage estimation; however, this error is so small that it can be negligible. To measure the phase current and DC-link

voltage, Hall-effect current and voltage sensors are used in this work. The sensed current and voltage are sampled by the A/D converter of the DSP. The worst-case quantization error due to the A/D conversion can be estimated, as in (6.21):

$$E_Q = \frac{M}{2^{L+1}} \tag{6.21}$$

Where, L and M are the number of bits of the A/D converter and the maximum value of the signal. In this work, a 10 bit A/D converter is used for the phase current and voltage sampling. For example, if the maximum sensing range of the current is 10A and the voltage is 500V, the possible quantization error is:

$$E_Q = \frac{10}{2^{11}} = \frac{10}{2048} = 0.00488[A] \tag{6.22}$$

$$E_Q = \frac{10}{2^{11}} = \frac{500}{2048} = 0.24414[V] \tag{6.23}$$

Also, in current and DC-link voltage signal, there is noise generated from the electromagnetic interference and switching in the system. The amount of noise can vary in different systems.

2) Parameter errors by manufacturing imperfections and temperature variation

Ideally, an inductance variation for the surface-mounted permanent magnet type of a BLDC machine is negligible. But in actual cases, there is a small inductance variation due to manufacturing imperfections, leakage flux, and local saturation of the flux. Also, the phase resistance value can be changed by temperature variation. Typically, the wire resistance made by copper has ±10% variation when the temperature is changed from room temperature to 130° F.

3) Limited sampling rate

In order to calculate the optimal current waveform for power density maximization by using the proposed method, the derivative of the phase current (di/dt) has to be calculated using the sampled phase current data obtained from the A/D converters. Since the calculation of di/dt is very sensitive to the error of sampled current data, the di/dt term is calculated sparsely to increase time (dt term), and hence, to decrease the error of di/dt term. Another way to decrease the di/dt term error is collecting many samples to arrive at one sample which is a time average. Suppose the calculation frequency of the proposed control is f_c and speed is N RPM. In this case, the estimated zero-synchronizing point error is given as:

$$E_c = \frac{\frac{P}{2} \times \frac{N}{60} \times 360}{f_c} \quad \text{[electrical degree]} \tag{6.24}$$

Because of the limited sampling rate of a DSP, f_c has a limited number. For example, if the calculation frequency of the proposed control algorithm is 10kHz at 1000 RPM and it is a four-pole machine, then E_c is 1.2° electrical angle.

2. Numerical calculation of the error

Based on the simulation model of the three-phase BLDC generator system described in Chapter IV, the error of the proposed control method can be calculated. The error sources are defined as:

1) Error from the current and DC-link voltage measurement:

- Current measurement

  −Sensor (LEM, LA55-P) error: 0 ~ ±1%

  −Noise of the current signal

  −Quantization error: ±10A/2048 (10 bits A/D converter)

- DC-link voltage measurement

  −Sensor (LEM, LV25-P) error: 0 ~ ±1%

  −Noise of the DC-link voltage signal

  −Quantization error: ±500V/2048 (10 bits A/D converter)

The current and DC-link voltage sensor error is based on the sensor's specification given from the manufacturer (LEM), and signal noise is assumed to vary from 0 to ±1%, depending on the different generator systems. The quantization error directly depends on the number of bits of A/D converters.

2) Parameter errors:

- Resistance variation: 0% ~ ±10% (room temperature ~ 130° F)
- Inductance variation: 0% ~ ±10% (by local saturation and manufacturing imperfections)

The amount of resistance variation is based on a data sheet of the copper wires, and the inductance variation is assumed to vary from zero to ±10%, based on saturation level, leakage flux, and manufacturing tolerances.

3) Calculation of induced EMF:

A digitized form of the voltage equation for induced EMF calculation in the three-phase BLDC generator is presented as in (4.33):

$$\begin{aligned} \mathrm{E_{ab}[k]} &= R \cdot \left(i_a[k] + i_b[k]\right) \\ &\quad + L \cdot \left(\frac{\left(i_a[k] - i_a[k-1]\right) - \left(i_b[k] - i_b[k-1]\right)}{t[k] - t[k-1]} \right) + V_{dclink} \cdot \left(S_a[k-1] - S_b[k-1]\right) \end{aligned} \tag{4.33}$$

The modified voltage equation with possible error sources is given in (6.25):

$$\begin{aligned} \mathrm{E_{ab[k]}} &= R \cdot (1 \pm \eta_1) \cdot \left(i_{a[k]} \cdot ((1 \pm \eta_5) \pm \eta_9) - i_{b[k]} \cdot ((1 \pm \eta_7) \pm \eta_{11})\right) \\ &\quad + L \cdot (1 \pm \eta_2) \cdot \left(\frac{\left(i_{a[k]} \cdot ((1 \pm \eta_5) \pm \eta_9) - i_{a[k-1]} \cdot ((1 \pm \eta_6) \pm \eta_{10})\right) - \left(i_{b[k]} \cdot ((1 \pm \eta_7) \pm \eta_{11}) - i_{b[k-1]} \cdot ((1 \pm \eta_8) \pm \eta_{12})\right)}{t_{[k]} - t_{[k-1]}} \right) \\ &\quad + V_{dclink} \cdot \left(S_{a[k-1]} - S_{b[k-1]}\right) \cdot ((1 \pm \eta_3) \pm \eta_4) \end{aligned}$$

(6.25)

Where, the error sources are:

η_1: Parameter variation (phase resistance)

η_2: Parameter variation (phase inductance)

η_3: DC-link voltage measurement error (noise + sensor error)

η_4: Quantization error for DC-link voltage measurement

η_5, η_6, η_7 and η_8: Current measurement error (noise + sensor error)

η_9, η_{10}, η_{11} and η_{12}: Quantization error for current measurement

(6.25) is added to the simulation program and the worst-case error is simulated. The worst-case error and simulated waveforms of the EMF without errors and with possible error sources under different conditions are shown.

In the simulation of the EMF calculation in Chapter IV, a filtering operation for noise cancellation is not used since there is no noise in an ideal numerical simulation. However, in the experiment, a filtering operation is used for the EMF calculation to reduce the noise. This operation leads to a time-delay and a phase shift between voltage and current so that the average power is reduced. Figs. 95 through 97 show the simulation results with filtering operation and without error sources.

Fig. 95 shows the original line-to-line EMF from the machine itself and the filtered line-to-line EMF after the calculation by using the voltage equation. Filtered line-to-line EMF has a time-delay, as shown, because of the filtering operation.

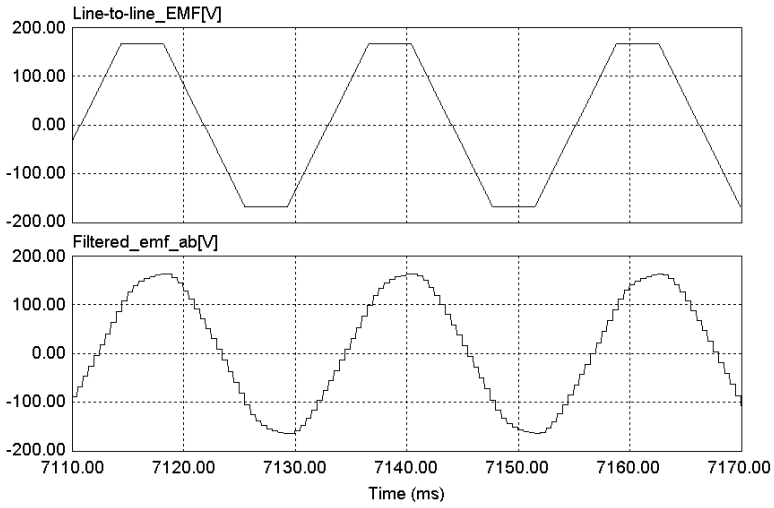

Fig. 95. Original line-to-line EMF and filtered line-to line EMF.

Figs. 96 and 97 show the optimal current reference waveform for power density maximization based on the calculated line-to-line EMFs.

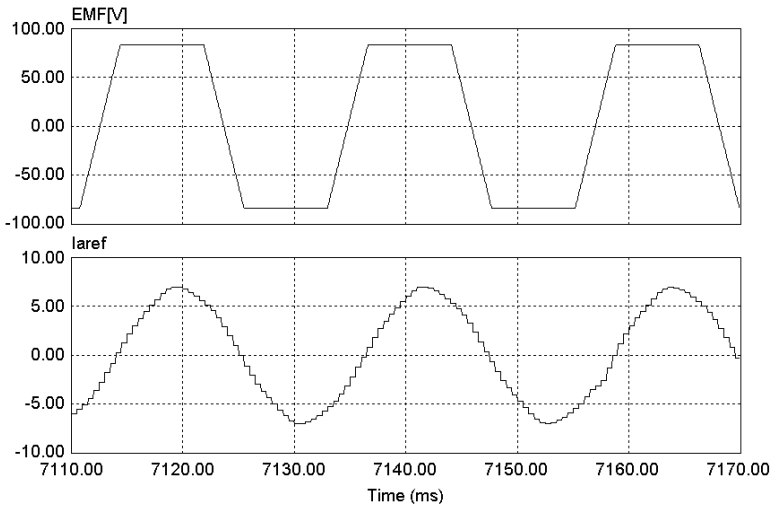

Fig. 96. Original phase EMF and current reference waveform.

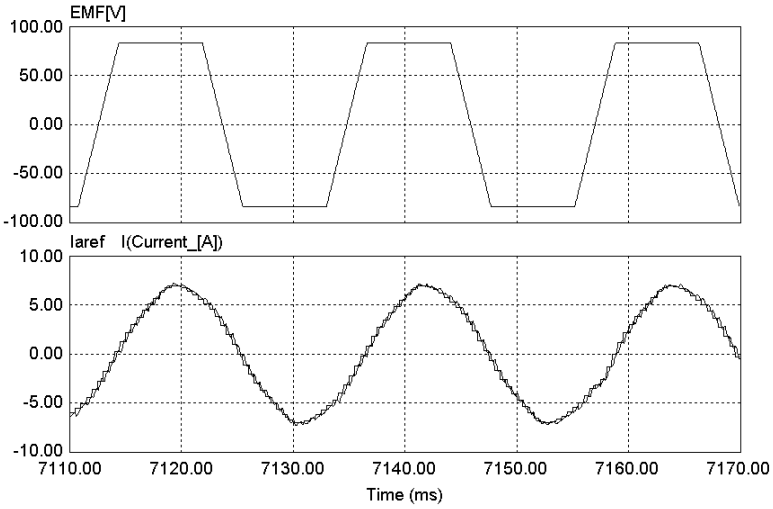

Fig. 97. Original phase EMF, current reference waveform, and controlled current.

Original phase EMF and current reference is a bit out of phase because of time-delay and this phase difference reduces the output power. The current is controlled well

by using a hysteresis controller. The output power based on the filtered line-to-line EMF without any error source is 394.3W and it is smaller than the ideal simulation result. The output power comparison according to the error sources is presented in the end of this section. Specification of the simulation for error analysis is as following:

- Speed: 1350 RPM
- Sampling frequency : 20kHz
- η_1: Parameter variation (phase resistance) = ±10%
- η_2: Parameter variation (phase inductance) = ±10%
- η_3: DC-link voltage measurement error = ±5%
- η_4: Quantization error for DC-link voltage measurement
  = ±500V/2048 = ±0.24414V (10bits A/D converter)
- η_5, η_6, $\eta_7$and η_8: Current measurement error = ±5%
- η_9, η_{10}, η_{11} and η_{12}: Quantization error for current measurement
  = ±10A/2048 = ±0.00488A (10 bits A/D converter)

Based on the error specification of the simulation, the worst-case error is simulated separately and in each situation, other error sources are assumed as zero. The current and voltage quantization error depends on the number of bits of A/D converter. In this analysis, the number of bits of A/D converter is considered to be 10, which is the number of bits of the DSP in the experimental test-bed; these quantization errors are included in the current and voltage measurement error in the simulation, respectively.

Fig. 98 shows the output power decrease due to the current measurement error. As the error increases, EMF calculation becomes incorrect and results in incorrect current reference waveform. This incorrect current reference leads the decrease of the output power.

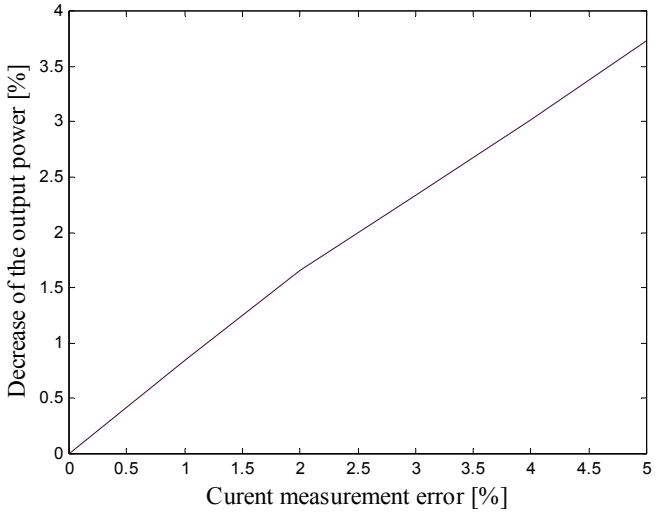

Fig. 98. Impact of the current measurement error.

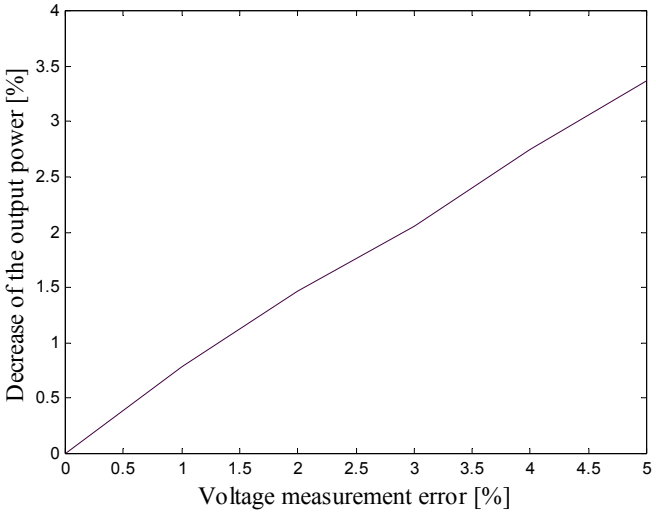

Fig. 99. Impact of the voltage measurement error.

Fig. 99 shows the output power decrease due to the voltage measurement error. Sensitivity of the voltage measurement error is almost same as the current measurement error. Figs. 100 and Fig. 101 also show the sensitivity of the proposed method from the parameter variation. The phase resistance value can be changed due to the temperature variation.

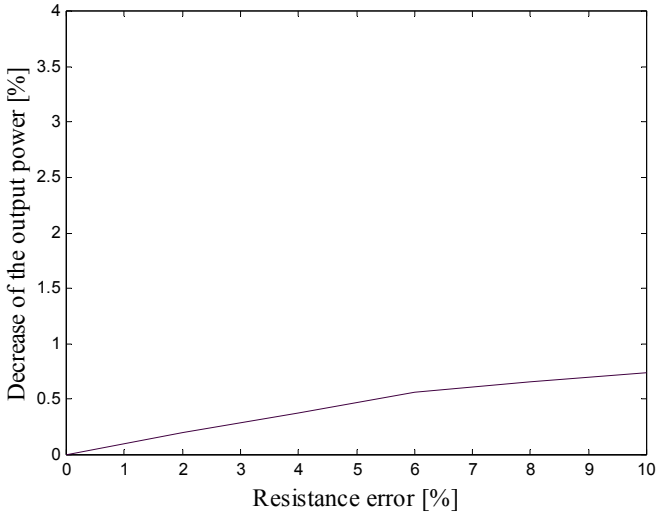

Fig. 100. Impact of the resistance variation error.

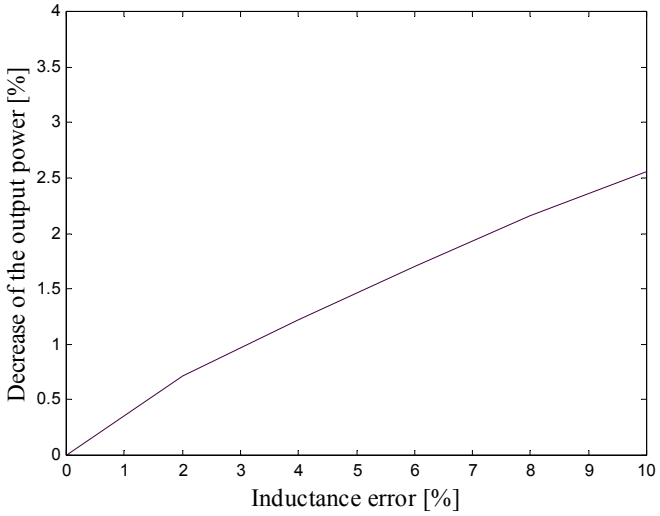

Fig. 101. Impact of the inductance variation error.

Fig. 100 shows the worst-case error due to resistance variation. As shown in Fig. 100, decrease of the output power due to the resistance variation is very small and almost negligible compared with the power decrease due to the measurement error.

The output power decrease due to the inductance variation occurs because of the manufacturing imperfections, leakage flux, and local saturation of the flux, etc., and is shown in Fig. 101. Since inductance variation affects directly to the (di/dt) term of the voltage equation, the inductance variation is more sensitive than the resistance variation, but it is less sensitive than the measurement error.

Table X shows the comparison of the electrical output power according to the worst-case error sources. From Table X, it is known that current measurement error is the most dominant error source and resistance variation is negligible. In this section, various error sources and their effects on the output power have been studied. These possible error sources make the difference of the simulation and experimental results in Chapter IV and V. It is known that more precise measurement of the currents and voltage can increase the output power by improving the performance of the proposed control method.

Table X. Electrical output power according to the worst-case error sources.

Error source	Worst-case error	Output Power [W]	Decrease [%]
No error		394.3 [W]	-
Current measurement	5 [%]	379.6 [W]	3.73 [%]
Voltage measurement	5 [%]	381.0 [W]	3.37 [%]
Resistance variation	10 [%]	391.4 [W]	0.74 [%]
Inductance variation	10 [%]	384.2 [W]	2.56 [%]
Combined		381.5 [W]	3.25 [%]

H. Conclusion

In this chapter, various attributes of the proposed control method were discussed. The proposed theory is adopted for the neutral point connection mode and for practical applications. Various possibilities of driving the BLDC generator system such as load variation, one-phase failure, and unbalanced induced EMF mode have been investigated. It is verified that the proposed theory can be used for the multi-phase BLDC generator as well. In addition, the influence of measurement and parameter errors on the calculated current reference waveform and output power has been shown through simulation results. These analyses of the various attributes will be helpful for improving power generation systems.

CHAPTER VII

SUMMARY AND FUTURE RESEARCH

This chapter presents a summary of the work accomplished and the contributions of the research. Also, a section on the suggestions for future research work has been included.

A. Summary of the Work

In this dissertation, a new control method to maximize the power density and to minimize the size and weight of the BLDC generator with the non-sinusoidal induced EMF for a given rating of machine by controlling the current spectrum has been presented. The fundamental machine equations for a BLDC generator are utilized, and the optimal current waveform is formulated from the power concept, induced voltage equation and simple algebraic method. The proposed control method is verified with simulation and experimental works. Also, various attributes of practical interest are analyzed and simulated to investigate the impact of possible situations on real systems.

Chapter II deals with the fundamental characteristics of the BLDC generator. The advantages and disadvantages of the BLDC generator, mechanical structure, magnetic characteristic and trapezoidal induced EMF of the BLDC generator are described. The simplified dynamic equations for the BLDC generator drive are also introduced.

Chapter III reviewed the conventional rectification methods of the BLDC generator, and the drawbacks of the existing method are investigated to develop a new method that can solve those problems.

In Chapter IV, the theory of the proposed control method for power density maximization is presented. In the first part of the chapter, the derivation of the optimal current waveform of a single-phase BLDC generator and EMF calculation using the voltage equation are explained. The detailed control strategy for a three-phase BLDC generator drive follows. And also a new simple algebraic method to eliminate the zero-sequence component is proposed. To verify the proposed theory, the simulation model for the BLDC generator drive is developed. The description of the dynamic model of the BLDC generator drive and the details of the simulation work were carried out to validate the theory of the proposed control method.

In Chapter V, the description of the experimental setup developed in the laboratory was presented. The experimental results to prove the theory and simulation results were also presented.

The analyses of various attributes of the proposed control method have been performed and the results are presented in Chapter VI. The influences from several situations: (neutral point connection, sinusoidal current waveform, load variation, one-phase failure, unbalanced induced EMF, and multi-phase) on the performance of the proposed control technique are investigated through simulation and experiments, and the results are presented. And also, effects of the various error sources are investigated as well.

B. Contributions of the Research

This research mainly focused on developing a new control technique for power density maximization of the BLDC generator with the non-sinusoidal induced EMF for a given rating of machine, while not requiring additional hardware or an expensive microprocessor. In order to achieve this, the advanced control method based on the power concept has been developed and implemented on the experimental test-bed. The major contributions of the research work can be summarized as follows:

- A new control method based on the power concept to maximize power density and minimize size and volume is developed.
- For a three-phase optimal current waveform of the BLDC generator, a simple algebraic method, which replaces a complicated and time-consuming FFT, is developed.
- The proposed control method has been evaluated through computer simulations using the dynamic model of the BLDC generator drive. The performance of the drive in different operating conditions with the proposed control scheme has been thoroughly studied.
- A prototype BLDC generator drive based on a fixed-point DSP has been designed and developed in the laboratory. The proposed control algorithm has been tested, and the performance has been satisfactory.
- Detailed analyses under various attributes are performed, and effects of the possible error sources are investigated as well.

C. Future Research Work

In this dissertation, the validities of the advanced control method for power density maximization in the given rating of machine have been successfully verified. The performance of the proposed control method is satisfactory. Based on these results, further research works are suggested in this area:

- Dualities of the BLDC motor and generator such as base speed, maximum speed, rated power, should be researched for the extension of the theory.
- The theory of the optimal current waveform for the electrical output power density maximization can be used for the mechanical output power density maximization of the BLDC motor.
- Control methods focusing on maintaining DC-link voltage in any circumstance should be proposed.
- To optimize the performance of the BLDC generator drive, the trade-off between maximization of the power per ampere ratio and minimization of the power pulsation are required. Since we are using the power equation in the control algorithm, we can also minimize the power pulsation based on the application.
- Extending of the proposed control method for the BLDC generator drive to achieve maximum regenerative braking force in the application of electric vehicles and aircrafts can be proposed.

REFERENCES

[1] J. R. Hendershot Jr. and T. J. E. Miller, *Design of Brushless Permanent-magnet Motors,* England, Oxford Magna Physics Publications, 1994.

[2] T. Kenjo and S. Nagamori, *Permanent Magnet and Brushless DC Motors,* Tokyo, Sogo Electronics Publishing Company, 1994.

[3] S. J. Park, H. W. Park, M. H. Lee and F. Harashima, "A New Approach for Minimum-Torque-Ripple Maximum-Efficiency Control of BLDC Motor," *IEEE Trans. on Industrial Electronics*, vol. 47, no. 1, pp. 109-114, Feb. 2000.

[4] S. K. Safi, P. P. Acarnley and A. G. Jack, "Analysis and Simulation of the High-Speed Torque Performance of Brushless DC Motor Drives," *IEEE Proc. of Electr. Power Appl.*, vol. 142, no. 3, pp. 191-199, May 1995.

[5] K. F. Rasmussen, J. H. Davies, T. J. E. Miller, M. I. McGilp and M. Olaru, "Analytical and Numerical Computation of Air-Gap Magnetic Fields in Brushless Motors with Surface Permanent Magnets," *IEEE Trans. on Industry Applications*, vol. 36, no. 6, pp. 1547-1554, Nov./Dec., 2000.

[6] The Institute of Electrical Engineers of Japan, *Small Motors*, Tokyo, Bomundang publications, 2000.

[7] L. McGrow and C. Pollock, "Low Cost Brushless Generators," in *IEEE Industry Application Conference*, vol. 2, pp. 1229-1236, Oct. 1999.

[8] R. Krishnan and G. H. Rim, "Modeling, Simulation, and Analysis of Variable-Speed Constant Frequency Power Conversion Scheme with a Permanent Magnet Brushless DC Generator," *IEEE Trans. on Industrial Electronics*, vol. 37, no. 4, pp. 291-296, Aug., 1990.

[9] J. Kim, *Handbook of Magnet and DC Motors,* Seoul, Hanjin Publications, 2002.

[10] A. Ferrero and G. Superti-Furga, "A New Approach to the Definition of Power Components in Three-phase Systems under Nonsinusoidal Conditions," *IEEE Trans. on Instrumentation and Measurement*, vol. 40, no. 3, pp. 568-577, June 1991.

[11] D. C. Hanselman, "Minimum Torque Ripple, Maximum Efficiency Excitation of Brushless Permanent Magnet Motors," *IEEE Trans. on Industrial Electronics*, vol. 41, no. 3, pp. 292-300, June 1994.

[12] H. J. Gutt and J. Muller, "New Aspects for Developing and Optimizing Modern Motorcar Generators," in *IEEE Industry Application Society Annual Meeting*, vol. 1, pp. 3-8, Oct. 1994.

[13] H. J. Gutt and J. Muller, "Mechatronical Considerations in Modern Motorcar Generators," *IEEE Industry Applications Magazine*, pp. 33-38, Nov./Dec., 1996.

[14] M. Naidu, N. Boules and R. Henry, "A High-Efficiency, High Power Generation System for Automobiles," in *IEEE Industry Applications Conference*, vol. 1, pp. 709-716, Oct. 1995.

[15] V. V. Vasher, J. G. Kettleborough, I. R. Smith and W. R. Gerges, "Generalized Model of Brushless DC Generator," *IEEE Trans. on Aerospace and Electronic Systems*, vol. 25, no. 4, pp. 508-519, July, 1989.

[16] V. Caliskan, D. J. Perreault, T. M. Jahns and J. G. Kassakian, "Analysis of Three-Phase Rectifiers with Constant-Voltage Loads," in *IEEE Power Electronics Specialists Conference*, vol. 2, pp. 715-720, July 1999.

[17] B.K. Bose, "Power Electronics – A Technology Review," *Proceedings of the IEEE*, vol. 80, no. 8, pp. 1303-1334, August 1992.

[18] J. W. Lim and B. H. Kwon, "A Power-Factor Controller for Single-Phase PWM Rectifiers," *IEEE Trans. on Industrial Electronics*, vol. 46, no. 5, pp. 1035-1037, Oct. 1999.

[19] R. Martinez and P. N. Enjeti, "A High-Performance Single-Phase Rectifier with Input Power Factor Correction," *IEEE Trans. on Power Electronics*, vol. 11, no. 2, pp. 311-317, Mar. 1996.

[20] O. Stihi and B. T. Ooi, "A Single-Phase Controlled-Current PWM Rectifier," *IEEE Trans. on Power Electronics*, vol. 3, no. 4, pp. 453-459, Oct. 1988.

[21] J. T. Boys and A. W. Green, "Current-Forced Single-Phase Reversible Rectifier," *IEE Proceedings*, vol. 136, no. 5, pp. 205-211, Sept. 1989.

[22] A.W. Green and J.T. Boys, "Hysteresis Current-Forced Three Phase Voltage-Sourced Reversible Rectifier," *IEE Proceedings*, vol. 136, Pt. B, no. 3, pp. 113-120, May, 1989.

[23] N. Mohan, *Electric Drives: An Integrative Approach*, New York, Mnpere Inc., 2001.

APPENDIX

DSP SOURCE CODE FOR THE ADVANCED CONTROL METHOD FOR POWER DENSITY MAXIMIZATION OF THE BLDC GENERATOR

```
;*************************************************************************************
;File Name: Power.ASM
;Description: 0.75 [kW] BLDC Generator Drive Using TMS320F243 DSP
;Author: Hyung-Woo Lee, Power Electronics and Motor Drive Lab., Texas A&M University
;May., 12, 2003
;*************************************************************************************

            .include    "X24x.h"

              .sect     "vectors"

RSVECT          B       _c_int0
INT1            B       PHANTOM
INT2            B       DETECTION
INT3            B       PHANTOM
INT4            B       PHANTOM
INT5            B       PHANTOM
INT6            B       PHANTOM
RESERVED        B       PHANTOM
SW_INT8         B       PHANTOM
SW_INT9         B       PHANTOM
SW_INT10        B       PHANTOM
SW_INT11        B       PHANTOM
SW_INT12        B       PHANTOM
SW_INT13        B       PHANTOM
SW_INT14        B       PHANTOM
SW_INT15        B       PHANTOM
SW_INT16        B       PHANTOM
TRAP            B       PHANTOM
NMI             B       PHANTOM
EMU_TRAP        B       PHANTOM
SW_INT20        B       PHANTOM
SW_INT21        B       PHANTOM
SW_INT22        B       PHANTOM
SW_INT23        B       PHANTOM


;=====================================================
; Variable definition
;=====================================================

            .bss        GPR0, 1
            .bss        Sense_DCVtemp, 1
            .bss        TempV, 1
            .bss        Sense_DClinkV, 1
            .bss        Ia_input, 1
            .bss        Ib_input, 1
            .bss        Ic_input, 1
            .bss        Ia, 1
            .bss        Ib, 1
            .bss        Ic, 1
            .bss        Ia_ref, 1
            .bss        Ib_ref, 1
            .bss        Ic_ref, 1
            .bss        BangbangA, 1
            .bss        BangbangB, 1
            .bss        BangbangC, 1
            .bss        Switching_function_a, 1
            .bss        Switching_function_b, 1
            .bss        Switching_function_c, 1
```

```
        .bss    Switching_function_aa, 1
        .bss    Switching_function_bb, 1
        .bss    Switching_function_cc, 1
        .bss    Vda, 1
        .bss    Vdb, 1
        .bss    Vdc, 1
        .bss    Vdab, 1
        .bss    Vdca, 1
        .bss    Vdbc, 1
        .bss    Eaa, 1
        .bss    Ebb, 1
        .bss    Ecc, 1
        .bss    Eab, 1
        .bss    Eab_disp, 1
        .bss    Eab_fil, 1
        .bss    Eab_fil_disp, 1
        .bss    Eab_fil_temp, 1
        .bss    Ebc, 1
        .bss    Ebc_disp, 1
        .bss    Ebc_fil, 1
        .bss    Ebc_fil_disp, 1
        .bss    Ebc_fil_temp, 1
        .bss    Eca, 1
        .bss    Eca_disp, 1
        .bss    Eca_fil, 1
        .bss    Eca_fil_disp, 1
        .bss    Eca_fil_temp, 1
        .bss    Temp, 1

        .bss    COMP, 1
        .bss    COMP2, 1
        .bss    COMP3, 1
        .bss    CAPT, 1
;       .bss    DA_OPSET, 1
        .bss    INVERSE_BangbangA, 1
        .bss    INVERSE_BangbangB, 1
        .bss    INVERSE_BangbangC, 1
        .bss    Old_Ia, 1
        .bss    Old_Ib, 1
        .bss    Old_Ic, 1
        .bss    Old_Vdab, 1
        .bss    Old_Vdca, 1
        .bss    Old_Vdbc, 1
        .bss    Delta_Ia, 1
        .bss    Delta_Ib, 1
        .bss    Delta_Ic, 1
        .bss    INPUTa_OLD, 1
        .bss    OUTa, 1
        .bss    OUTa_OLD, 1
        .bss    INPUTb_OLD, 1
        .bss    OUTb, 1
        .bss    OUTb_OLD, 1
        .bss    INPUTc_OLD, 1
        .bss    OUTc, 1
        .bss    OUTc_OLD, 1

        .bss    Ipeak, 1
;       .bss    Va_normal, 1
;       .bss    Vb_normal, 1
;       .bss    Vc_normal, 1
;       .bss    Va_peak, 1
;       .bss    Va_peak_old, 1
        .bss    Vaawave, 1
        .bss    Vbbwave, 1
        .bss    Vccwave, 1

        .bss    Vawave, 1
        .bss    Vbwave, 1
        .bss    Vcwave, 1
        .bss    Vawave1, 1
        .bss    Vbwave1, 1
        .bss    Vcwave1, 1
        .bss    Vawave2, 1
        .bss    Vbwave2, 1
        .bss    Vcwave2, 1
```

```
            .bss    Vawave_disp2, 1
            .bss    Vbwave_disp2, 1
            .bss    Vcwave_disp2, 1

            .bss    Eab_fil_disp2, 1
            .bss    Ebc_fil_disp2, 1
            .bss    Eca_fil_disp2, 1
            .bss    Ia_ref_disp, 1
            .bss    Ib_ref_disp, 1
            .bss    Ic_ref_disp, 1

            .bss    Resistance, 1
            .bss    Inductance, 1

;=====================================================
; Reset & interrupt vectors
;=====================================================


KICK_DOG    .macro
            LDP     #00E0h
            SPLK    #05555h, WDKEY
            SPLK    #0AAAAh, WDKEY
            LDP     #0h
            .endm

AB_PLUS_CD  .macro  a, b, c, d

            ZAC
            LT      a
            MPY     b
            LTA     c
            MPY     d
            APAC

            .endm

AB_MINUS_CD .macro  a, b, c, d

            ZAC
            LT      a
            MPY     b
            LTA     c
            MPY     d
            SPAC

            .endm

            .text
            .global _c_int0

_c_int0:
            CLRC    CNF
            CLRC    OVM
            SETC    SXM
            CLRC    XF
            SETC    INTM

            MAR     *, AR2
            LAR     AR2, #0300h
            SPLK    #0, *+
            SPLK    #0, *+
            SPLK    #0, *+
            SPLK    #0, *+
            SPLK    #0, *+
            SPLK    #0, *
            LAR     AR2, #0300h
;           LAR     AR1, #stack

            LDP     #WDKEY>>7
            SPLK    #006Fh, WDCR
            KICK_DOG


; I/O SETTING
```

```
                LDP     #00E1h
                SPLK    #0FFFFh, OCRA
                SPLK    #03FFh, OCRB

; CLEAR EV CONTROL REGISTERS

                LDP     #0E8h
                SPLK    #0000h, T1CON
                SPLK    #0000h, T1PER
                SPLK    #0000h, T1CNT
                SPLK    #0000h, T1CMP
                SPLK    #0000h, T2CON
                SPLK    #0000h, T2PER
                SPLK    #0000h, T2CNT
                SPLK    #0000h, T2CMP
                SPLK    #0000h, T3CON
                SPLK    #0000h, T3PER
                SPLK    #0000h, T3CNT
                SPLK    #0000h, T3CMP
                SPLK    #0000h, COMCON
                SPLK    #0000h, DBTCON
                SPLK    #0000h, ACTR
                SPLK    #0000h, SACTR
                SPLK    #0000h, CMPR1
                SPLK    #0000h, CMPR2
                SPLK    #0000h, CMPR3
                SPLK    #0000h, SCMPR1
                SPLK    #0000h, SCMPR2
                SPLK    #0000h, SCMPR3
                SPLK    #0000h, CAPCON
                SPLK    #0000h, CAPFIFO

; GP TIMER2 SETTING START WITH GPT1 PRESC 128

                SPLK    #0FFFEh, T2PER
                SPLK    #00000h, T2CNT
                SPLK    #17C0h, T2CON

; PWM UNIT SETTING

                SPLK    #0500, T1PR
                SPLK    #0000h, T1CNT
                SPLK    #0000h, ACTR
;               SPLK    #03F0h, DBTCON  ;2.4usec dead band;#05ech, DBTCON
;               SPLK    #0504h, DBTCON ;0.5 us
;               SPLK    #0510h, DBTCON ;4 us
                SPLK    #0a04h, DBTCON      ;1 us
                SPLK    #00000, CMPR1
                SPLK    #00000, CMPR2
                SPLK    #00000, CMPR3
                SPLK    #2687h, COMCON
                SPLK    #0a687h, COMCON
                SPLK    #0000100000000101b, T1CON
                SPLK    #0000100001000101b, T1CON
                SPLK    #0000000100000000b, GPTCON

; CAPTURE UNIT SETTING

                SPLK    #0b0fch, CAPCON
                SPLK    #1500h, CAPFIFO

                LACC    FIFO1
                LACC    FIFO2
                LACC    FIFO3

                LDP     #224
                LACC    ADCFIFO1
                LACC    ADCFIFO2

; CORE MASK SETTING
```

```
                LDP     #4
                LACC    #0ah
                SACL    IMR
                LACC    IFR
                SACL    IFR


; EV Mask Setting, Vector & Flag reset

                LDP     #EVIFRA>>7
                SPLK    #0ffffh, EVIFRA
                SPLK    #0ffffh, EVIFRB
                SPLK    #0ffffh, EVIFRC
                SPLK    #0000000010000000b, IMRA
                SPLK    #0000000010000000b, IMRB
                SPLK    #0000000010000000b, IMRC


; ADC UNIT SETTING

                LDP     #224
;               SPLK    #1101000000100000b, ADCTRL1
                SPLK    #1101100000110100b, ADCTRL1
                SPLK    #0000010000000000b, ADCTRL2

                LDP     #4
                SPLK    #0500, COMP
                SPLK    #0500, COMP2
                SPLK    #0500, COMP3
                SPLK    #0500, INVERSE_BangbangA
                SPLK    #0500, INVERSE_BangbangB
                SPLK    #0500, INVERSE_BangbangC
                SPLK    #0000h, CAPT
;               SPLK    #2048, DA_OPSET


;=============================================
; STARTING PROCEDURE
;=============================================

; DISABLE CAPT INPUT
                LDP     #0E8h
                SPLK    #8000h, CAPCON


; SET I/O UNIT AS I

                LDP     #00E1h
                SPLK    #0FFC7h, OCRA
                SPLK    #0000h, PADATDIR


; WHICH SEQUENCE

                LACC    PADATDIR
                AND     #0038h
                LDP     #4
                SACL    CAPT
                LACC    CAPT, 13
                SACH    CAPT


; DISABLE I/O UNIT

                LDP     #0E1h
                SPLK    #0FFFFh, OCRA


; CAPTURE UNIT SETTING

                LDP     #0E8h
                SPLK    #0b0fch, CAPCON

                CLRC    INTM
```

```
;=============================================
; END OF STARTING PROCEDURE
;=============================================

LOOP:
                NOP
                NOP
                NOP
                B       LOOP


SEQUENCE:

                LDP     #4
                LACC    INVERSE_BangbangA
                SUB     BangbangA
                LDP     #0E8h
                SACL    CMPR1

                LDP     #4
                LACC    INVERSE_BangbangB
                SUB     BangbangB
                LDP     #0E8h
                SACL    CMPR2

                LDP     #4
                LACC    INVERSE_BangbangC
                SUB     BangbangC
                LDP     #0E8h
                SACL    CMPR3

                SPLK    #0666h, ACTR

                B       END

END:
                RET

DAC:
                LDP     #4

                LACC    Vawave_disp2
                SACL    GPR0
                OUT     GPR0, DAC0_VAL

                LACC    Ia_ref_disp, 2
                SACL    GPR0
                OUT     GPR0, DAC1_VAL

                LACC    BangbangA
                SACL    GPR0
                OUT     GPR0, DAC2_VAL

;               LACC    Ic_input, 2
;               SACL    GPR0
;               OUT     GPR0, DAC3_VAL

                OUT     GPR0, DAC_VAL

                RET


; A/D CONVERSION INTERRUPT SERVICE ROUTINE

DETECTION:

ADC_CHECK1:
                LDP     #224
                BIT     ADCTRL1, BIT7
                BCND    ADC_CHECK1, TC

                LDP     #224
                SPLK    #1101100000010001b, ADCTRL1
```

```
ADC_CHECK2:
                BIT     ADCTRL1, BIT7
                BCND    ADC_CHECK2, TC

                LDP     #224
                CLRC    SXM
                LACC    ADCFIFO2, 10
                LDP     #4
                SACH    Sense_DCVtemp

                LDP     #224
                CLRC    SXM
                LACC    ADCFIFO2, 10
                LDP     #4
                SACH    Ib_input

                LDP     #224
                CLRC    SXM
                LACC    ADCFIFO1, 10
                LDP     #4
                SACH    Ic_input

                LDP     #224
                CLRC    SXM
                LACC    ADCFIFO1, 10
                LDP     #4
                SACH    Ia_input

                CLRC    SXM
                LDP     #224
;               SPLK    #1101000000100000b, ADCTRL1
                SPLK    #1101100000110100b, ADCTRL1

;Current control
                LDP     #4

                LACC    Ia_input    ;(1.0A = 66 digital => 66*8A+531=1059)
;               SFR
;               SFR
                SUB     #531
                SACL    Ia

                LACC    Ib_input
;               SFR
;               SFR
                SUB     #531
                SACL    Ib

                LACC    Ic_input
;               SFR
;               SFR
                SUB     #531
                SACL    Ic

                CLRC    SXM
                SETC    SXM
                LACC    Ia
                SUB     Ia_ref

                BGZ     TURN_OFF_a
                SPLK    #0500, BangbangA
                SPLK    #1, Switching_function_a
                B       Phase_b

TURN_OFF_a:

                SPLK    #0, BangbangA
                SPLK    #0, Switching_function_a
                B       Phase_b

Phase_b:

                CLRC    SXM
                SETC    SXM
                LACC    Ib
```

```
                SUB     Ib_ref

                BGZ     TURN_OFF_b
                SPLK    #0500, BangbangB
                SPLK    #1, Switching_function_b
                B       Phase_c

TURN_OFF_b:

                SPLK    #0, BangbangB
                SPLK    #0, Switching_function_b
                B       Phase_c

Phase_c:

                CLRC    SXM
                SETC    SXM
                LACC    Ic
                SUB     Ic_ref

                BGZ     TURN_OFF_c
                SPLK    #0500, BangbangC
                SPLK    #1, Switching_function_c
                B       TURN_ON

TURN_OFF_c:

                SPLK    #0, BangbangC
                SPLK    #0, Switching_function_c
                B       TURN_ON

TURN_ON:

;EMF Caculation

                LDP     #4
                CLRC    SXM

                LT      Sense_DCVtemp
;               MPY     #22
                MPY     #17
                LTP     TempV
                SACL    Sense_DClinkV       ;(real voltage*66/3)

                LACC    Switching_function_a
                NEG
                ADD     #1
                SACL    Switching_function_aa

                LACC    Switching_function_b
                NEG
                ADD     #1
                SACL    Switching_function_bb

                LACC    Switching_function_c
                NEG
                ADD     #1
                SACL    Switching_function_cc


                LT      Sense_DClinkV
                MPY     Switching_function_aa
                LTP     TempV
                SACL    Vda

                LT      Sense_DClinkV
                MPY     Switching_function_bb
                LTP     TempV
                SACL    Vdb

                LT      Sense_DClinkV
                MPY     Switching_function_cc
                LTP     TempV
                SACL    Vdc
```

```
                LACC    Vda
                SUB     Vdb
                SACL    Vdab

                LACC    Vdb
                SUB     Vdc
                SACL    Vdbc

                LACC    Vdc
                SUB     Vda
                SACL    Vdca


                LDP     #4
                SPLK    #86, Inductance
                SPLK    #4, Resistance

                SETC    SXM
                LACC    Ia
                SUB     Old_Ia
                SACL    Delta_Ia

                LACC    Ib
                SUB     Old_Ib
                SACL    Delta_Ib

                LACC    Ic
                SUB     Old_Ic
                SACL    Delta_Ic


                AB_PLUS_CD      Resistance, Ia, Inductance, Delta_Ia
                SACL    Eaa     ;(should multiply by 1/200)

                AB_PLUS_CD      Resistance, Ib, Inductance, Delta_Ib
                SACL    Ebb

                AB_PLUS_CD      Resistance, Ic, Inductance, Delta_Ic
                SACL    Ecc


                LACC    Eaa
                SUB     Ebb
                ADD     Old_Vdab
                SACL    Eab

                LACC    Ebb
                SUB     Ecc
                ADD     Old_Vdbc
                SACL    Ebc

                LACC    Ecc
                SUB     Eaa
                ADD     Old_Vdca
                SACL    Eca

; Filtering and peak value

                LACC    Eab             ;(worst : 37180)
                SFR
                SFR
                SFR
                SFR
                SFR
                ADD     #1000
                SACL    Eab_disp        ;(worst : 620~1781)

                LACC    Ebc
                SFR
                SFR
                SFR
                SFR
                SFR
                ADD     #1000
                SACL    Ebc_disp
```

```
                LACC    Eca
                SFR
                SFR
                SFR
                SFR
                SFR
                ADD     #1000
                SACL    Eca_disp

                LACC    Eab_disp
                ADD     INPUTa_OLD
                SUB     OUTa_OLD, 1
                ADD     OUTa
                SACL    OUTa
                LACC    Eab_disp
                SETC    SXM
                SACL    INPUTa_OLD
                SETC    SXM
                CLRC    SXM
                LACC    OUTa
                SFR
                SFR
                SFR
                SFR
;               SFR
                SACL    OUTa_OLD
                SACL    Eab_fil_disp
                LACC    Eab_fil_disp
                SUB     #1000
                SACL    Eab_fil_temp
                LT      Eab_fil_temp
                MPY     #32
                LTP     Temp
                SACL    Eab_fil


                LACC    Ebc_disp
                ADD     INPUTb_OLD
                SUB     OUTb_OLD, 1
                ADD     OUTb
                SACL    OUTb
                LACC    Ebc_disp
                SETC    SXM
                SACL    INPUTb_OLD
                SETC    SXM
                CLRC    SXM
                LACC    OUTb
;               SFR
                SFR
                SFR
                SFR
                SFR
                SACL    OUTb_OLD
                SACL    Ebc_fil_disp
                LACC    Ebc_fil_disp
                SUB     #1000
                SACL    Ebc_fil_temp
                LT      Ebc_fil_temp
                MPY     #32
                LTP     Temp
                SACL    Ebc_fil

                LACC    Eca_disp
                ADD     INPUTc_OLD
                SUB     OUTc_OLD, 1
                ADD     OUTc
                SACL    OUTc
                LACC    Eca_disp
                SETC    SXM
                SACL    INPUTc_OLD
                SETC    SXM
                CLRC    SXM
                LACC    OUTc
                SFR
```

```
                SFR
;               SFR
                SFR
                SFR
                SACL    OUTc_OLD
                SACL    Eca_fil_disp
                LACC    Eca_fil_disp
                SUB     #1000
                SACL    Eca_fil_temp
                LT      Eca_fil_temp
                MPY     #32
                LTP     Temp
                SACL    Eca_fil


;               LACC    Eab_fil
;               SFR
;               SFR
;               ADD     #2048
;               SACL    Eab_fil_disp2

                LACC    Ebc_fil
                SFR
;               SFR
                SFR
                ADD     #2048
                SACL    Ebc_fil_disp2

;               LACC    Eca_fil
;               SFR
;               SFR
;               ADD     #2048
;               SACL    Eca_fil_disp2

                SETC    SXM
                LACC    Eab_fil
                SFR
                SFR
                SFR
                SFR
                SFR
                SACL    Vawave1
                LACC    Eca_fil
                SFR
                SFR
                SFR
                SFR
                SFR
                SACL    Vawave2
                LACC    Vawave1
                SUB     Vawave2
                SACL    Vawave

                SETC    SXM
                LACC    Ebc_fil
                SFR
                SFR
                SFR
                SFR
                SFR
                SACL    Vbwave1
                LACC    Eab_fil
                SFR
                SFR
                SFR
                SFR
                SFR
                SACL    Vbwave2
                LACC    Vbwave1
                SUB     Vbwave2
                SACL    Vbwave

                SETC    SXM
                LACC    Eca_fil
                SFR
```

```
                SFR
                SFR
                SFR
                SFR
                SACL    Vcwave1
                LACC    Ebc_fil
                SFR
                SFR
                SFR
                SFR
                SFR
                SACL    Vcwave2
                LACC    Vcwave1
                SUB     Vcwave2
                SACL    Vcwave

                LACC    Vawave
                ADD     #2048
                SACL    Vawave_disp2

                LACC    Vbwave
                ADD     #2048
                SACL    Vbwave_disp2

                LACC    Vcwave
                ADD     #2048
                SACL    Vcwave_disp2

                SPLK    #34, Ipeak ; 16,45, 10 = 32*32*5A/(3*174V)
                B       PII


PII:

                SETC    SXM
                LT      Vawave
                MPY     Ipeak
                LTP     Temp
                SFR
                SFR
                SFR
                SFR
                SFR
                SACL    Ia_ref

                SETC    SXM
                LACC    Ia_ref
;               LT      Ia_ref
;               MPY     #8
;               LTP     Temp
                ADD     #2048
                SACL    Ia_ref_disp

                SETC    SXM
                LT      Vbwave
                MPY     Ipeak
                LTP     Temp
                SFR
                SFR
                SFR
                SFR
                SFR
                SACL    Ib_ref

                SETC    SXM
                LT      Ib_ref
                MPY     #8
                LTP     Temp
                ADD     #2048
                SACL    Ib_ref_disp

                SETC    SXM
                LT      Vcwave
                MPY     Ipeak
```

```
                LTP     Temp
                SFR
                SFR
                SFR
                SFR
                SFR
                SACL    Ic_ref

                SETC    SXM
                LT      Ic_ref
                MPY     #8
                LTP     Temp
                ADD     #2048
                SACL    Ic_ref_disp


;               SETC    SXM
;               LACC    Vawave
;               AND     #0FFFFh
;               RPT     #15
;               SUBC    Va_peak
;               SETC    SXM
;               SACL    Va_normal
;               LT      Va_normal
;               MPY     Ipeak
;               LTP     Temp
;               SACL    Ia_ref
;
;               LACC    Ia_ref
;               ADD     #2048
;               SACL    Ia_ref_disp
;
;               SETC    SXM
;               LACC    Vbwave
;               AND     #0FFFFh
;               RPT     #15
;               SUBC    Va_peak
;               SETC    SXM
;               SACL    Vb_normal
;               LT      Vb_normal
;               MPY     Ipeak
;               LTP     Temp
;               SACL    Ib_ref
;
;               SETC    SXM
;               LACC    Vcwave
;               AND     #0FFFFh
;               RPT     #15
;               SUBC    Va_peak
;               SETC    SXM
;               SACL    Vc_normal
;               LT      Vc_normal
;               MPY     Ipeak
;               LTP     Temp
;               SACL    Ic_ref


                LACC    Ia
                SACL    Old_Ia

                LACC    Ib
                SACL    Old_Ib

                LACC    Ic
                SACL    Old_Ic

                LACC    Vdab
                SACL    Old_Vdab

                LACC    Vdbc
                SACL    Old_Vdbc

                LACC    Vdca
                SACL    Old_Vdca
```

```
;               LACC    Va_peak
;               SACL    Va_peak_old


                CALL    SEQUENCE
                CALL    DAC
                LDP     #232
                LACC    EVIFRA
                SACL    EVIFRA
                CLRC    INTM
                RET

PHANTOM:
                RET
                .end
```

VITA

Hyung-Woo Lee was born in Taejon, Korea. He received his B.S. and M.S. degrees in electrical engineering from Hanyang University in 1998 and 2000, respectively. In September 2000, he joined the doctoral program at Texas A&M University. His research interests are design, analysis and control of the motor/generator and power electronics. He has been a student member of IEEE. He can be reached c/o Dr. M. Ehsani, Power Electronics Laboratory, Department of Electrical Engineering, Texas A&M University, College Station, Texas 77843.